THE MECHANICAL ROLE OF LOCALIZED ACTIN POLYMERIZATION IN GIANT UNILAMELLAR VESICLES

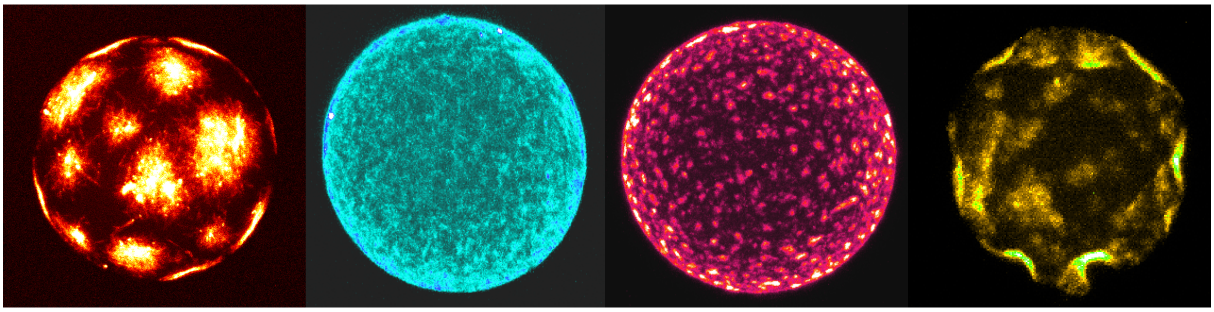

DISSERTATION BY KATHARINA DÜRRE
Juni 2018 – München

Lehrstuhl für Zellbiophysik – E27
Physikdepartment
Technische Universität München

TECHNISCHE UNIVERSITÄT MÜNCHEN
PHYSIKDEPARTMENT
LEHRSTUHL FÜR ZELLBIOPHYSIK – E27

THE MECHANICAL ROLE OF LOCALIZED ACTIN POLYMERIZATION IN GIANT UNILAMELLAR VESICLES

KATHARINA DÜRRE

Vollständiger Abdruck der von der Fakultät für Physik der Technischen Universität München zur Erlangung des akademischen Grades eines

Doktors der Naturwissenschaften (Dr. rer. nat.)

genehmigten Dissertation.

Vorsitzender: Prof. Dr. Ulrich Gerland

Prüfer der Dissertation: 1. Prof. Dr. Andreas R. Bausch

2. Dr. Zeynep Ökten

Die Dissertation wurde am 18.06.2018 bei der
Technischen Universität München eingereicht und durch die
Fakultät für Physik am 13.07.2018 angenommen.

Katharina Dürre: *The mechanical role of localized actin polymerization in Giant Unilamellar Vesicles* , © Juni 2018

ABSTRACT

Interactions of the actin cytoskeleton and the plasma membrane are essential for cellular processes like migration or endocytosis. While the biochemical processes of actin polymerization and membrane organization are well characterized, a deep understanding about actin induced shape remodeling of fluid membranes is still lacking. It is not clear how similar microscopic assembly kinetics of actin define the elastic network properties that control membrane shape. It was the main goal of this thesis to understand the mechanical interplay between the actin cytoskeleton and a fluid membrane, which was achieved by the in-vitro reconstitution of different cellular processes inside of giant unilamellar vesicles (GUVs).

In the first part of this thesis, dendritic lamellipodia-like actin networks were reconstituted to study force transduction of lamellipodia formation. Network growth is induced upon activation of the actin nucleating factor Arp2/3 complex. The resulting network pushes the membrane forward during cell migration and induces a negative bending of the membrane during endocytosis. It was found, that Capping Protein (CP) is one key regulator for dendritic network formation and allows to switch between both deformation types. The CP dependent growth kinetics were translated into a set of differential equations to identify the microscopic assembly kinetics and link them to the observed shape deformation. Encapsulation of VASP instead of Arp2/3 in the second part, allowed to reconstruct the mechanic interaction between filopodia-like actin bundles and the membrane. The formation of a bundled actin network could be observed. But only, when polymerization was sufficiently shifted towards the membrane, finger-like membrane protrusions appeared. Both network architectures were static once they formed at the GUV's membrane. However, actin polymerization is dynamic. Thus in the third part, Xenopus extract was encapsulated to reconstitute an actively polymerizing actomyosin cortex at the membrane. Membrane deformations were not visible. Addition of α-actinin induced a symmetry break and stable actin domains were formed, that triggered the formation of membrane blebs and a negative bending of the membrane. Heterogeneous membrane organization is also thought to be a driver of symmetry breaks in actin networks. Thus, a modified protocol of cDICE was developed in the last part of this thesis to enable production of phase separated vesicles at room temperature. The right oil composition of the lipid-oil mixture, in which lipids were dissolved, was decisive for the amount of cholesterol in the lipid bilayer. Only, when enough cholesterol sorted into the membrane, phaseseparation was observed.

The successful encapsulation of various cellular processes revealed that sufficient membrane localization and heterogeneous polymerization of actin are essential to remodel the membrane. Thereby, local growth kinetics at non-steady state conditions determine the force transduction of the assembled microstructures. The combination of in-vitro reconstitution and mathematical modeling is a promising approach, to fully reconstitute an artifical cell in the future.

ZUSAMMENFASSUNG

Die Interaktion zwischen dem Aktinzytoskelett und der Plasmamembran sind entscheidend für viele zelluläre Prozesse wie Zellmigration oder Endozytose. Während die biochemischen Prozesse der Aktinpolymerisation und der Plasmamembran ausführlich beschrieben sind, fehlt bisher noch ein tiefes Verständis dafür, wie Aktinnetzwerke Deformationen in der Membran erzeugen können. Hierbei ist nicht klar, wie ähnliche Wachstumskinetiken die elastischen Eigenschaften der Netzwerke bestimmen und so unterschiedliche Arten der Membrandeformation erzeugen. Daher war es das Ziel dieser Arbeit die mechanischen Wechselwirkungen zwischen dem Aktinzytoskelett und der Plasmamembrane zu charakterisieren und zu verstehen. Hierfür wurden unterschiedliche zelluläre Prozesse erfolgreich in einem künstlichen System nachgebaut.

In dem ersten Teil dieser Arbeit wurden dendritische Lamellipodia-ähnliche Aktinnetzwerke in riesigen unilamellaren Vesikeln (GUVs) rekonstruiert, um die Kraftübertragung des Lamellipodiums auf die Membran zu untersuchen. Dendritische Netzwerke werden durch Arp2/3 kontrollierte Aktinpolymerisation erzeugt. Die Netzwerke drücken die Membran während der Zellmigration nach vorne, wohingegen sie während der Endozytose eine negative Krümmung der Membran erzeugen. Hierbei hat sich herausgestellt, dass Capping Protein (CP) ein wichtiger Regulator dendritischer Netzwerke ist und es so ermöglicht zwischen den unterschiedlichen Deformationen zu schalten. Die CP abhängigen Wachstumsprozesse wurden in ein System aus gekoppelten Differentialgleichungen übersetzt, um die mikroskopische Netzwerkarchitektur in Relation zu den beobachteten Deformationen zu setzen. Das Einkapseln von VASP anstelle von Arp2/3 im zweiten Teil der Arbeit ermöglichte die mechanischen Interaktionen zwischen Filopodia-ähnlichen Aktinbündeln und der Membran zu untersuchen. Nur wenn genug Aktin an der Membran polymerisiert ist, waren fingerähnliche Membranausstülpungen zu erkennen. Beide untersuchten Netzwerke waren statisch sobald sie an der Membran aufgebaut waren. Aktinpolymerisation ist jedoch dynamisch. Daher wurde in dem dritten Teil der Arbeit Xenopus Extrakt in GUVs eingekapselt, um aktiv polymerisierende Aktin-Myosin Kortexe an der

Membrane aufzubauen. Membrandeformationen waren jedoch nicht zu beobachten. Erst das Hinzufügen von α-actinin hat einen Symmetriebruch des Kortexes erzeugt und stabile Aktindomänen waren an der Membran zu beobachten. Dadurch wurde die Bildung von Membranausstülpungen und negativen Krümmungen der Membran verursacht. Symmetriebrüche können aber auch durch eine inhomogene Membrankomposition erzeugt werden. Um solche Prozesse zu untersuchen, wurde in dem letzten Teil der Arbeit das Protokol für die Vesikelherstellung weiterentwickelt. Hierbei war die richtige Zusammensetzung der Lipid-Öl Mischungen entscheidend, um genug Cholesterol in die Membran einzubauen. Nur, wenn genügend Cholesterol in die Membran segregiert, können phasenseparierte Vesikel entstehen.

Das erfolgreiche Einkapseln unterschiedlicher zellulärer Prozesse verdeutlicht, dass nur eine ausreichende Lokalisation und inhomogenes Wachstum von Aktin zu Membrandeformationen führt. Hierbei bestimmen die örtlichen Wachstumsprozesse im Nichtgleichgewicht den Krafübertrag durch die polymerisierten Mikrostrukturen. Die Kombination von in-Vitro Rekonstitution und mathematischer Modellierung ist ein vielversprechender Ansatz, um zukünftig eine Zelle vollständig künstlich nachbauen zu können.

PUBLICATIONS

Some results and figures have appeared previously in the following publications:

DÜRRE K., KEBER F. C., BLEICHER P., BRAUNS F., CYRON C. J., FAIX J., BAUSCH A. R. Capping protein-controlled actin polymerization shapes lipid membranes. NATURE COMMUNICATIONS, 9.1 (2018), p. 454

ACKNOWLEDGMENTS

An dieser Stelle möchte ich mich bei Allen bedanken, die zu der Erstehung dieser Arbeit beigetragen haben.

Besonders bedanken möchte ich mich bei meinem Doktorvater *Prof. Andreas Bausch*. Nicht nur wissenschaftlich, sondern auch persönlich habe ich in den letzten Jahren Einiges dazugelernt. Vielen Dank dafür. Eine bessere Vorbereitung für meinen zukünftigen Weg, kann ich mir nicht vorstellen.

Auch *Felix Keber*, *Prof. Jan Faix* und *Christian Cyron* sollen nicht unerwähnt bleiben, da ich ohne euch das Paper so nicht hätte schreiben können. Bei Felix bedanke ich mich für seine Geduld bei unseren endlosen Diskussionen, auch wenn ich mal wieder auf dem "Schlauch" gestanden bin. Bei Hans möchte ich mich für die vielen lehrreichen, unterhaltsamen Telefonate bedanken und natürlich für die grandiosen Zellexperimente. Bei Christian bedanke ich mich für die vielen spannenden Diskussionen und Anregungen rund um das Thema der Netzwerkmechanik.

Ich möchte mich bei Allen aktuellen und ehemaligen Mitgliedern der Bauschgruppe für die wunderbare Arbeitsatmosphäre bedanken. Man war hier mit seinen "challenges" nie alleine und hat auch immer jemanden gefunden, um über sein "Leid" zu klagen. Hier möchte ich *Philip Bleicher, Ben Buchmann, Joanna Deek, Henry Dehne, Fabian Hecht, Martina Lindauer, Etienne Loiseau, Leone Rossetti und Alfredo Sciortino* danken, die sich zum Teil vor allem in der letzten Phase meiner Doktorarbeit so einiges an Jammern anhören durften. Bei Alfredo, Ben, Henry und Philip bedanke ich mich auch fürs Korrektur lesen dieser Arbeit. Etienne danke ich dafür, dass er mir alles gezeigt hat, was man zur Herstellung der Vesikel benötigt und ich ihm jederzeit noch so viele Fragen stellen konnte. Zudem möchte ich mich bei meiner super motivierten Bachelorstudentin *Julia Schweiger* für ihr großes Engagement beim Einkapseln des Xenopus Extrakts bedanken.

Bedanken möchte ich mich auch bei *Gabi Chmel, Karin Vogt, Monika Rusp* und *Thi-Hieu Ho*, die immer dafür gesorgt haben, dass genug Protein in unseren Eisschränken war.

Bei Herrn *Prof. Ralph Rupp* möchte ich mich für die Froscheier bedanken und bei *Edith Mentele* für die Unterstützung bei der Herstellung des Froschextrakts.

Bei *Prof. Dan Flechter* und seiner Gruppe möchte ich mich für eine ganz tolle und aufregende Zeit in seinem Labor in Berkley bedanken.

Dem gesamten Lehrstuhl E22/E27 möchte für eine wunderbare Zeit, die leider viel zu schnell vorbei ging, danken. Hierbei, danke ich vor allem den Lunchy Luniches, die immer wieder so wunderbare Pasta, leckere Currys, außergewöhnliche Suppenkreationen und einen köstlichen Spargelsalat zum Mittagessen gezaubert haben.

Ein ganz großes Dankschön geht an meine *Eltern*, die mich während meiner gesamten Studienzeit nicht nur finanziell unterstützt und mir somit eine sorgenfreie Studienzeit ermöglicht haben, sondern auch immer ein offenes Ohr für mich hatten. Meinem *Bruder* danke ich für die vielen spannenden und auch immer sehr motivierenden Diskussionen über unsere Doktorarbeiten.

Martin, in den letzten Jahren warst du immer an meiner Seite und hast mich in allem unterstützt, wo du nur konntest. Dafür möchte ich dir von ganzem Herzen danken.

CONTENTS

I INTRODUCTION

1 INTRODUCTION 3
- 1.1 Lamellipodium reconstitution 4
- 1.2 Filopodium reconstitution 5
- 1.3 Xenopus leavis extract 6
- 1.4 Phase separated vesicles 7

II PHYSICAL BACKGROUND

2 PHYSICAL BACKGROUND 11
- 2.1 Polymerization forces in cells 11
  - 2.1.1 Force generation by network formation 11
  - 2.1.2 Biochemical and physical strategies to steer cell movement 18
- 2.2 Phase transition behavior in composite membranes 20
  - 2.2.1 Thermodynamic behavior of lipid membranes 20
  - 2.2.2 First order phase-transitions in homogeneous membranes 21
  - 2.2.3 Unmixing of in-homogeneous membranes 23

III MATERIALS AND METHODS

3 MATERIALS & METHODS 29
- 3.1 Purified Proteins 29
  - 3.1.1 Actin 29
  - 3.1.2 Arp2/3-complex and VCA 30
  - 3.1.3 Non-muscle myosin II 30
  - 3.1.4 Profilin 31
  - 3.1.5 Capping Protein 31
  - 3.1.6 Vasodilator stimulated phosphoprotein 32
  - 3.1.7 Fascin 32
  - 3.1.8 α-actinin 33
  - 3.1.9 Pyrene Assays 33
- 3.2 Preparation of Xenopus laevis extract 33
- 3.3 Spatial network growth on a monolayer 35
  - 3.3.1 Preparation of a monolayer 35
  - 3.3.2 Polymerization of dendritic networks on the monolayer 35
- 3.4 GUV preparation and protein encapsulation 35
  - 3.4.1 Continuous droplet interface crossing encapsulation (cDICE) 35
  - 3.4.2 Preparation of Lipid-Oil emulsions 37
  - 3.4.3 GUV encapsulation of purified proteins by cDice 37

3.4.4 GUV encapsulation of Xenopus laevis extract by cDICE 38
3.5 Fluorescence Microscopy 39
3.5.1 Epifluorescence and confocal microscopy 39
3.5.2 TIRF-microscopy 39

IV RESULTS AND DISCUSSION

4 CP CONTROLLED ACTIN POLYMERIZATION INDUCES MEMBRANE DEFORMATIONS 43
4.1 Membrane localized polymerization is induced by Arp2/3 complex 43
4.2 Membrane localized network formation is controlled by CP 45
4.3 Domain nucleation and growth is controlled by CP 47
4.3.1 Time resolved domain growth inside of vesicles 48
4.3.2 Time resolved domain growth on a supported lipid monolayer 50
4.4 Contractile behavior of NMM II is most efficient at high CP concentrations 51
4.5 Structure of actin domains depends on CP 56
4.5.1 Implementation of the model 56
4.5.2 Theoretical discussion 60
4.6 Discussion 63
5 IN-VITRO RECONSTITUTION OF FILOPODIA FORMATION MEDIATED BY VASP 67
5.1 VASP promotes the formation of filopodia like actin bundles 68
5.2 Filopodia-like network formation localized to the membrane inside of GUVs 68
5.3 Membrane restricted actin elongation and bundling induce membrane protrusions 72
5.4 Fluorescently labeled VASP localizes to the membrane localized actin network and filopodia 74
5.5 Discussion 75
6 RECONSTITUTED ACTIVE ACTIN CORTICES IN GUVS RESHAPE MODEL MEMBRANES 79
6.1 Efficient reconstitution of active cortices in GUVs 79
6.2 Effect of α-actinin on cortex structure 82
6.3 Membrane bending and blebbing induced by inhomogeneities in the actin cortex 82
6.4 Actin cortex collapse induced by global myosin contraction 85
6.5 Discussion 86
7 PHASESEPARATION 91
7.1 Phase separated vesicles produced by cDice 91

7.1.1 Liquid-liquid coexistence depends on mineral oil content 91
7.1.2 Lipid aggregate size is controlled by cholesterol and mineral oil 93
7.1.3 Cholesterol incorporation in the lipid membrane via double layer cDICE 93
7.2 Physical characterization of phase separation 95
7.3 Functionalization of liquid-disordered domains by NiNTA-lipids 98
7.4 Discussion 99

V CONCLUSION AND OUTLOOK

8 CONCLUSION AND OUTLOOK 105

BIBLIOGRAPHY 107

ACRONYMS

ABP	actin binding protein
Arp2/3*	activated Arp2/3
B	barbed end density
cDICE	continuous droplet interface crossing encapsulation
CP	Capping Protein
dlcDICE	double layer cDICE
ECM	extracellular matrix
FAB	F-actin binding domain
F-actin	filamentous actin
F_{mix}	Helmholtz free energy of mixing
GAB	G-actin binding domain
G-actin	actin monomer
GUV	giant unilamellar vesicle
hVASP dGAB	human VASP besides the GAB domain, which was from Dictyostelium discoideum
L_d	liquid disordered phase
LO1	mineral oil layer without cholesterol but mineral oil
LO2	mineral oil layer without mineral oil but cholesterol
L_o	liquid ordered phase
NMMII	non muscle myosin II
NPF	Nucleation promoting factor
T_C	critical temperature
T_M	miscibility temperature
VASP	Vasodilator Stimulated Phosphoprotein
V^+	paused state VCA
VCA	Arp2/3 activator containing a verprolin, center and acidic region

VCA*	G-actin bound VCA
WASP	Wiskott Aldrich Syndrom Protein

Part I

INTRODUCTION

1

INTRODUCTION

Various cellular processes rely on the mechanical interplay between the plasma membrane and the dynamic actin cytoskeleton. During cell migration dendritic actin networks, the so called lamellipodium, polymerize at the leading edge to push the membrane forward. The same growth processes are also found during endocytosis and induce an negative bending of the membrane [16, 70, 80, 124]. The formation of stiff actin bundles, called filopodia, induce fingerlike membrane protrusions, which are not only important for directed cell migration but also sense the environment and establish a direct contact to the extracellular matrix (ECM) [20, 93, 122]. The biochemical composition and basic mechanisms of structure formation of the actin cytoskeleton have been well studied over the past years. Likewise, membrane organization and mechanics have been investigated in-vivo and in-vitro. However, the mechanical interplay between both systems is not well understood. It is not clear, how the microscopic assembly kinetics are linked to their mesoscopic mechanical output, which finally controls membrane bending. Thus, it was the main goal of this thesis to study the underlying physical principles of actin induced membrane deformations by reconstitution of essential biological processes. Thereby, in vitro reconstitution of network formation inside of giant unilamellar vesicles (GUVs) is a promising approach to study these processes [4, 30, 87, 120]. Reconstitution of actin cortices inside of GUVs revealed that only contractile actin cortices are capable to drive shape remodeling and blebbing [30, 89], while in the absence of any molecular motors no shape deformation of the membrane could be observed at all [120].

In the first part of this work dendritic lamellipodia-like actin networks were reconstituted at the lipid bilayer inside of GUVs to understand how the same growth processes can induce different deformation modes of the membrane. Additionally, a mathematical model was developed to fully resolve the microscopic growth processes of localized actin polymerization. The second part focuses on a complete different network architecture. A network of actin bundles is localized to the membrane in order to mimic the mechanical interplay between the filopodium and the plasma membrane. Both reconstituted network structures remained stable for hours once they formed at the membrane. However, the actin cytoskeleton is dynamic in cells and continuously polymerizes and depolymerizes. The encapsulation of actin-intact Xenopus laevis extract inside of GUVs in the third part of this thesis allowed to study the interplay between dynamic network formation and the plasma membrane. For all encapsulation experiments the recently developed method continuous droplet interface crossing encapsulation (cDICE) was used [1, 89]. The advantages of this methods are an efficient protein encapsulation, fast production time (∼ 5 min), production at low temperatures (∼4°C), low protein consumption and waste (∼50 µl). In short, centrifugal forces push protein droplets trough a lipid-oil layer towards an aqueous glucose solution. In the lipid-oil layer, lipid aggregates diffuse to the water-oil interface and form a stable monolayer around the droplet. This monolayer zips together with a second monolayer, which is present at the lipid-oil/glucose interface and a vesicle is formed [1]. It was one of the main achievements of this work to find the right encapsulation conditions for every experimental setup and to adapt the production protocol accordingly. Only, when polymerization was heterogeneous and symmetry broken, membrane deformations occurred. The observed symmetry break was controlled by the presence of different actin binding proteins (ABPs) and not by membrane organization. However, it is known that also heterogeneous membrane organization drives symmetry breaks [109, 114]. Thus, the last part of this thesis focuses on the development of phase-separated vesicles to study the feedback of heterogeneous membrane organization on active network formation and the resulting symmetry break. To this end, a modified version of cDICE was developed in the last part to produce phase separated vesicles. This enables a complete new set of experiments to study the interdependence between network formation and membrane organization.

The combination of in-vitro reconstitution inside of GUVs and mathematical modeling provides a powerful tool to understand the coupling between microscopic growth kinetics at non-steady-state conditions and the resulting mechanical output. Such approaches lay the foundation for the full reconstitution of an artificial cell.

1.1 LAMELLIPODIUM RECONSTITUTION

One key player of lamellipodium formation is the nucleating Arp2/3 complex, which initiates the formation of dendritic-like, branched networks at the plasma membrane. Likewise Arp2/3 mediated network polymerization drives the propulsion of spherical objects in absence of any motor proteins [6, 153, 165]. ATP hydrolysis driven filament polymerization against the plasma membrane is sufficient to push the membrane forward. Thereby, the resulting membrane growth speed depends on the number of pushing actin filaments [98, 113]. The biochemical properties of the Arp2/3 complex are well characterized [101, 111]. It is activated at the plasma membrane by the Arp2/3 activator containing a verprolin, center and acidic region (VCA) of Wiskott Aldrich Syndrom Proteins (WASPs). After activation it binds to an already existing mother filament and forms a new actin branch with a 70° angle between mother and daughter filament [90, 151]. When dendritic networks are coupled to the outside of a lipid vesicle, such actin networks can create enough force to induce membrane protrusions by self-stabilization of the membrane [87]. A critical regulator of the microscopic network properties is heterodimeric Capping Protein (CP) [6, 52, 67, 94, 164]. It binds to actin filament barbed ends and inhibits filament elongation [128]. In the presence of CP branching by Arp2/3 complex is favored [6] whereas depletion of CP promotes filament elongation and successive bundle formation by crosslinking. Thus network architecture switches from lamellipodial to a filopodial network organization dependent on CP [94, 159].

To reconstitute lamellipodia like network formation, Arp2/3, its activator VCA and different ABPs were encapsulated inside of GUVs (Chapter 4). Arp2/3 activation was localized to the membrane and any spontaneous actin polymerization in the vesicle's bulk was suppressed by the presence of different ABPs. Additional encapsulation of CP allowed to switch between the different modes of membrane deformation. A mathematical model of the localized growth process was able to link microscopic growth kinetics to the observed shape deformations dependent on CP concentration.

1.2 FILOPODIUM RECONSTITUTION

In filopodia, network architecture is completely different compared to the lamellipodium. Rather than dendritic networks, stiff actin bundles composed of several filaments emerge at the membrane and push the membrane forward. Currently, two models of filopodia formation are discussed. In the "convergent elongation model" filopodia directly emerge from the Arp2/3 nucleated lamellipodium [60, 149], whereas in the "tip nucleation model" formins can directly nucleate and elongate filopodia in an Arp2/3 independent manner [43, 143]. Recently, it was found that a mixture of both models accounts for filopodia assembly in cells. Filopodia formation in suspended cells relied on the presence of Arp2/3 complex whereas adhered cells could form filopodia even in the absence of Arp2/3 [169]. Beside formins, Ena/-VASP are another class of proteins, which were identified to localize to filopodia tips and to be an important regulator for filopodia formation [14, 125]. They have two conserved domains (EVH1 and EVH2), which are interconnected by a proline rich region [79]. While the EVH1 domain is responsible for the correct targeting of VASP in cells, the EVH2 domain takes over all functional tasks. It is comprised of a F-actin binding domain (FAB) and G-actin binding domain (GAB), which allows VASP to bind to filament tips and promote filament elongation by direct delivery of new actin monomers to the barbed ends. Thereby, Ena/VASP increases filament elongation twofold to seven-fold [60, 166].

The encapsulation of VASP instead of Arp2/3 and VCA induced the formation of filopodia-like networks inside and at the membrane of the vesicles (Chapter 5). Complete suppression of bulk polymerization either by the presence of certain ABPs or by the presence of methylcellulose completely shifted network formation towards the membrane. The formation of finger-like protrusions could be observed. Simultaneous encapsulation of Arp2/3 and VASP mediated polymerization promoted the formation of dendritic instead of bundled networks.

1.3 XENOPUS LEAVIS EXTRACT

Extract from Xeonpus leavis extract is a popular tool to study network organization, acto-myosin contraction or actin based motility in-vitro [47, 82, 115, 152, 159]. When, beads or small vesicles, coated with a Nucleation promoting factor (NPF), were transferred into extract, Arp2/3 complex was activated and induced actin polymerization around the objects. As soon as the growth induced stresses at the surface became too high, the cortex ruptured and an continuously polymerizing actin tail was formed, which created enough force to push the objects forward. These experiments show, that all components necessary for active network formation are present in the extract. However, network formation and contraction is cell cycle dependent, as Arp2/3 complex is more active in the meiotic phase than in interphase of the extract [47]. Encapsulation of meiotic Xenopus extract inside of droplet emulsions was already successful to reconstitute the symmetry breaking of active cortices in cells [4], which has been recently identified to drive cell migration by membrane blebbing [32, 110, 126]. In accordance with other in-vitro assays, it was found that not only sufficient network connectivity but also the presence of myosin motors was essential for cortex rupture [4, 6, 153, 165]. Unfortunately, the mechanical interplay between the active actin cortices and membranes could not be studied, as surface tension of the water-oil interface of droplets is too high to be deformed by actin based motility. The surface tension of the water-oil interface is $\sim 0.7\ pN/nm$, whereas the surface tension of membranes is $\sim 0.035\ pN/nm$ [31, 95, 113].

Thus a modified protocol for cDice was developed, that allows to encapsulate Xenopus extract inside of GUVs (Chapter 6). The formation of a homogeneous active actin cortex could be observed, which did not induce any deformation of the membrane. Addition of the crosslinker α-actinin resulted in the formation of stable actin domains, which induced either an inwards bending of the membrane or the emergence of membrane blebs. Thus, only sufficient network connectivity provided by crosslinking led to a symmetry break of the cortex and induced membrane deformations.

1.4 PHASE SEPARATED VESICLES

The molecular composition of cellular membranes is heterogeneous and its lateral organization is diverse. Over the last two decades the lipid raft model was established to account for lateral membrane inhomogeneities [85, 134, 136, 137]. Lipid rafts are dynamic nanodomains in the nanoscale size and have the ability to fuse into large microdomains. They are typically enriched of cholesterol, sphingomyelins and proteins. They serve as a functional platform for various cellular processes like signal transduction and molecular trafficking. In vivo the size of lipid rafts (<200nm) is below the optical resolution limit and therefore hard to study. But in artificial membrane model systems, when a high melting temperature lipid is mixed with a low melting temperature lipid and cholesterol, phase separation into two liquid phases can be observed. The liquid-ordered phase is more packed and less fluid than the liquid-disordered phase. In addition, it is enriched in cholesterol and is therefore considered to be a model system to study lipid rafts [12, 155, 156]. Polymerization of dendritic actin networks around phase separated GUVs found that actin polymerization induces phase separation and controls its organization [86]. Studies about the interaction of contractile actin networks with supported lipid bilayers showed reorganization of membrane organization upon network contraction [77, 161]. However, it still remains an open questions how network organization controls active network formation and force transduction to the membrane. So far the production of vesicles with a liquid-liquid phase coexistence is not possible, as the amount of cholesterol is too low to induce a phaseseparation. Only addition of cholesterol from the outside could induce phaseseparation after production.

In the last part of this work a modified protocol of cDICE was developed to produce phase separated vesicles at room temperature (Chapter 7). The incorporation of cholesterol was dependent on the oil composition of the lipid-oil mixture, in which the lipids were dissolved. Only, in the absence of any mineral oil sufficient amounts of cholesterol segregated in the lipid bilayer. The phase transition behavior of vesicles produced by cDICE was comparable to electroswelled phase separated vesicles. The formation of phase separated vesicles by cDICE enables a complete new set of experiments to study symmetry breaks of active networks driven by membrane organization.

Part II

PHYSICAL BACKGROUND

2

PHYSICAL BACKGROUND

2.1 POLYMERIZATION FORCES IN CELLS

Different levels of force generation induced by the growth of dendritic actin networks can be described. Here I will first summarize the Brownian Ratchet mechanism, which was found to describe well force generation on a microscopic level [113]. On a mesoscopic scale a continuum elastic model accounts for stresses generated within the network during growth towards a surface. As soon as the stresses become too high, they are released by a break up of the actin gel and by a forward movement of the barrier [54]. To achieve a net movement, an inhomogeneous stress distribution and thus inhomogeneous network formation is required [109]. In cells for example the lamellipodium only forms at the leading edge so that pushing forces are only applied at the cell front resulting in a directed movement. How network heterogeneities and what strategies cells have to stir their movement is discussed in the second part of this section.

2.1.1 *Force generation by network formation*

2.1.1.1 *The Brownian Ratchet Model*

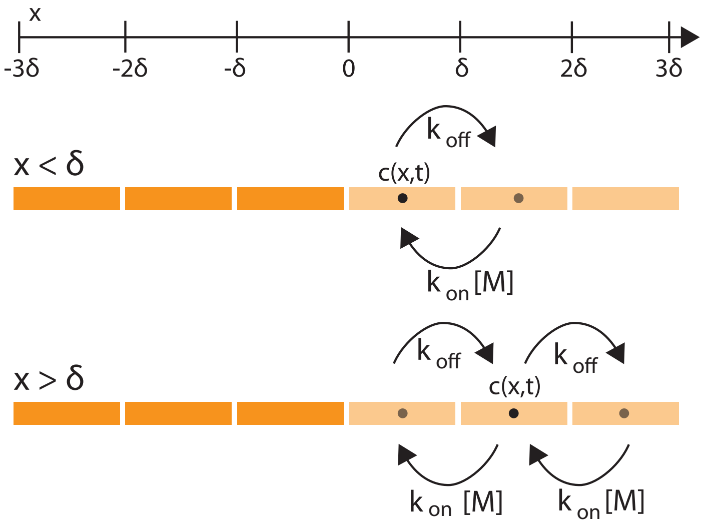

Figure 2.1: Evolution of the local density c in space and time dependent on the gap size δ is shown.

Force generation of single actin filaments pushing against a barrier can be described by the Brownian Ratchet Model (Figure 2.2) [113].

Actin monomers diffuse continuously to the filament's tip and are built in with a certain probability $\sim k_{\text{on}}[M]$, when the distance between the filament end and the barrier is sufficiently high. A minimal distance of $\delta = 2,5nm$ is required in case of actin. Thermal fluctuations of the barrier ensure that the gap size becomes sufficiently high. As soon as a new monomer is built in, the barrier cannot fluctuate back and is pushed forward. The monomers diffuse towards the filament end in a continuous random walk in a constant force field F_{ext} opposing actin polymerization. The local density $c(x,t)$ of actin monomers is described by the following reaction-diffusion equation (Figure 2.1).

$$\frac{\partial c}{\partial t} = D\frac{\partial^2 c}{\partial x^2} + \frac{Df}{k_{\text{B}}T}\frac{\partial c}{\partial x} + k_{\text{on}}[M][c(x+\delta,t) - H(x-\delta)c(x,t)] \\ + k_{\text{off}}[H(x-\delta)c(x-\delta,t) - c(x,t)] \qquad (2.1)$$

Thereby, is D is the diffusion coefficient. The second term of the equation accounts or the drift velocity ($v = f/\gamma$) due to the presence of an external force. The friction coefficient can be rewritten by using the Einstein correlation $\gamma = \frac{k_{\text{B}}T}{D}$. The last two terms describe monomer addition to the filament end dependent on the gap size. As soon as the gap between the filament is large enough ($x > \delta$) monomers are built in with a rate $\sim k_{\text{on}}[M]$. At all distances x monomers can depolymerize with k_{off}. When the monomer is built in at the tip, the binding energy is large enough, that the monomer remains tightly connected even if the barrier diffuses back.

Two different regimes for the filament protrusion velocity can occur. Either diffusion is low and thus the reaction is diffusion limited. In that case depolymerization can be neglected since monomer addition is much faster than depolymerization ($k_{\text{on}}[M] >> k_{\text{off}}[M]$) and the final protrusion velocity is given by the following equation.

$$v = \frac{2D}{\delta}\frac{(f\delta/k_{\text{B}}T)^2/2}{e^{f\delta/k_{\text{B}}T} - 1 - f\delta/k_{\text{B}}T} \qquad (2.2)$$

When the polymerization is limited by the probability, that the gap size is large enough, monomer addition is reaction limited. In that case monomer addition rate is weighted by the force allowing a monomer-sized gap. Depolymerization cannot be neglected anymore.

$$v = \delta(k_{\text{on}}[M]e^{-f\delta/k_{\text{B}}T} - k_{\text{off}}) \qquad (2.3)$$

Assuming, that actin polymerization is not diffusion limited at the cell front, the last equation can be used to determine the maximal force per filament, which is also called the stall force. The protrusion velocity is zero under the maximal force load and thus Equation 2.3 is set equal to zero in order calculate the stall force.

$$f_0 = \frac{kT}{\delta}ln\frac{[M]k_{\text{on}}}{k_{\text{off}}} \qquad (2.4)$$

The maximal stall force per filament is $f_0 \sim 7.8pN$ ($k_{\mathrm{on}} = 11.3\frac{M}{s}$, $[M] = 10\mu M, k_{\mathrm{off}} = 1.6\frac{1}{M}$). Membranes with membrane tension in the range of $0.035 - 0.039\frac{pN}{nm}$ [31] have a load force of about 25 pN. Thus filopodia, which in average consist of 20 filaments produce enough force to overcome the membrane tension and to move the membrane forward. One simplification of this model is that actin filaments are treated as fixed stiff rods, which are oriented perpendicularly to the barrier. However, actin filaments are semi-flexible and also undergo thermal bending. In reality orthogonal networks are found at the leading edge of cells with average angle of 45-55° in respect to the membrane [97, 140]. The elastic Brownian Ratchet model generalizes the Brownian Ratched model and includes filament elasticity (Figure 2.2). As a result it gives an expression for the effective polymerization velocity dependent filament orientation and the opposing load [95]. It also suggests that thermal fluctuations of the filaments promote gap formation between the filament end and the external load [97]. Thermal motion of the barrier alone would not be sufficient to ensure continuous monomer addition to the filament end.

The key assumption of both models is, that filaments ends are free and counteract external load by continuous monomer addition. However, experiments showed that propelling actin gels are tightly coupled to the surface of Listeria and forces up to 10 pN cannot rip them off [54]. To this end the tethered Brownian Ratchet Model was developed [99]. It assumes that membrane attachment of newly nucleated filaments is transient and that soon after nucleation they dissociate from the membrane (Figure 2.2). Attached filaments are tensed and counter-act protrusion, whereas free filaments are compressed and generate the protrusion force [97]. Thus the protrusion forces must not only withstand the external load, but also work against the pulling of the attached filaments [99].

$$F_{\mathrm{ext}} + f_{\mathrm{a}} \cdot a = f_{\mathrm{w}} \cdot w \tag{2.5}$$

Thereby f_{a} is the pulling force per attached filament, a is the number of attached filaments, f_{w} is the protrusion load per free filament and w the number of free filaments.

It was found that lamellipodial protrusion velocity depends on the number of pushing actin filaments. When the number of pushing filaments is too low, the total pushing force of the network is not sufficient to counteract membrane tension and protrusion velocity decreases. Likewise too high numbers of barbed ends are not favorable as many filament ends lead to a fast depletion of the actin monomer pool and again protrusion velocity decreases. A mathematical description of protrusion velocity dependent on the barbed end density is achieved by the translation of the growth processes into a set of partial differential equations (including depolymerization and filament capping) [98]. The output is a direct correlation between protrusion

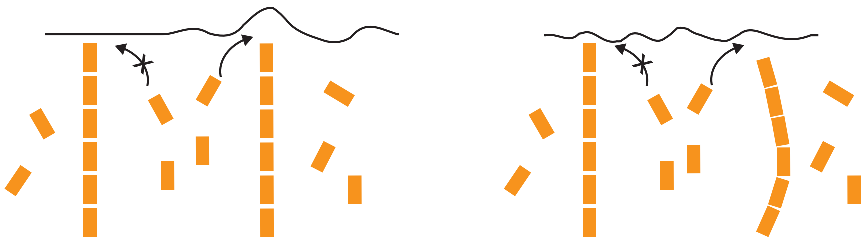

Brownian Ratchet

elastic Brownian Ratchet

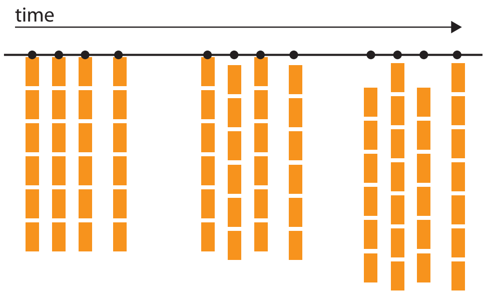

tethered Brownian Ratchet

Figure 2.2: Over the past decades the Brownian Ratchet Model was continuously improved to better fit to experimental results. At first, the Brownian Ratchet Model was developed to provide a general mechanism how stiff actin filaments generate a protrusion force at the membrane. Afterwards, the elastic Brownian Ratchet Model was developed to account for filament stiffness and orientation. The most recent model is the tethered Brownian Ratchet Model, which also implemented surface attached filaments in the force generation mechanism

velocity and number of filament barbed ends pushing against the membrane. This theoretical model sets the base for the modeling of membrane localized polymerization processes in the dependence of CP concentration, which was investigated in Chapter 4 and Chapter 5.

2.1.1.2 *Continuum elastic model*

An elastic model was found to describe force generation induced by continuous actin polymerization on a mesoscopic scale. The focus of this elastic approach is set on the mechanics of the whole actin gel, rather than on the mechanics of single filaments. Optical tweezer experiments allowed to characterize the elastic properties of the actin comet tail growing behind Listeria and support the approach that the actin comet tails can be treated as an elastic gel. The gel has a bending modulus K in the range of $100 - 1000\frac{Pa}{\mu m^4}$ and a Young's modulus of $Y = 10^3 - 10^4 Pa$. As already discussed for the tethered Brownian Ratchet model only a fraction of filaments are free. The other fraction is transiently coupled to the surface. Therefore, continuous monomer addition increases internal stresses within the growing network. Relaxation of this stress results in a forward movement of the beads [116]. A full mathematical description of the mesoscopic force generation mechanism is given in Gerbal et al. [54]. A further achievement of this model is that it also respects the cylindrical geometry of Listeria. The Brownian Ratchet Model in contrast assumes that filaments polymerize against a flat wall. Here a short overview of the force balance is given. The theoretical approach is divided into three parts.
At first, the focus is set on an actin gel growing from the back of a bacterium (Figure 2.3 a). Continuous polymerization at the bacterium's surface with polymerization speed v_{p1} induces internal stresses within the actin gel. The resulting elastic deformations are released within the tail and the bacterium moves forward with a speed v. After Newton's second law the elastic stresses within the network must balance out the external force in steady state ($F_{\text{ext}} = F_1$). Therefore, F_{ext} on every cross section must be balanced by the elastic stress on every cross section. From linear elastic theory and the assumption of volume conservation, an expression for the resulting force dependent on the the bacterium's speed (v) and the polymerization velocity (v_{p1}) is found.

$$F_{\text{ext}} = F_1 = YS_{\text{b}}(1 - \frac{v}{v_{\text{p1}}}) \tag{2.6}$$

Thereby Y is the Young's modulus of the actin gel and S_b the cross section of the bacterium. The resulting force is in the range of a few nN and hence more than sufficient to overcome the external force, which is experienced by the bacterium during movement trough the cytoplasm. Moreover the force to bend a flexible membranes is also several orders of magnitudes lower ($\sim 50pN$) [54].

Second only a cylindrical actin gel growing with speed v_{p2} normal to the lateral surface of the bacterium is considered (Figure 2.3 b). The continuous addition of actin monomers leads to a compression of the already grown actin gel. If the compression becomes too high a symmetry break occurs so that the actin shell breaks up and an actin tail forms behind the bacterium. All radial energy can relax within this tail. To calculate the resulting force the tangential and normal stresses are integrated over the bacterium's surface. Both components are treated separately. Integration of the normal stresses shows that only in the back stresses contribute to bead propulsion and induce F_{mot2}. All other normal stresses balance each other out due to rotational symmetry.

$$F_{\mathrm{mot2}} = YS_{\mathrm{b}}\frac{\alpha \cdot \delta}{3}(\alpha + \delta) \tag{2.7}$$

The parameters α and δ are the dimensionless thickness of the actin gel above the bacterium and the actin tail. The equation can be further simplified and gives a simple scaling law of the force independent on the actin polymerization speed and is thus non-linear.

$$F_{\mathrm{mot2}} \sim YS_{\mathrm{b}}\alpha^3 \tag{2.8}$$

The resulting force pushes forward the bacterium and resembles to the one, which one would apply on a piece of soap, when it slips out of the hand. Thus, it is also called the "soap effect".
The tangential stresses can be described by a simple friction law, as long as the lateral gel moves slowly.

$$F_{\mathrm{fric}} = -\gamma v_0 \tag{2.9}$$

The total force resulting from the cylindrical actin gel is given by the following force balance.

$$F_{\mathrm{ext}} = F_2 = F_{\mathrm{mot2}} + F_{\mathrm{fric}} \tag{2.10}$$

This geometry couples the non-linear contribution of the soap effect and antagonistic the friction force. An advantage of this model is that any change of external force or the friction coefficient can be easily compensated. The actin gel only has to adapt its growth size to adjust the elastic force, which finally determines the driving force. This leads to much steadier protrusion velocities of the bacterium in comparison to the first approach.
Last, both geometries are coupled, which results in the following force balance(Figure 2.3 c).

$$F_{\mathrm{ext}} = F_1 + F_2 = F_{\mathrm{mot1}} + F_{\mathrm{mot2}} + F_{\mathrm{fric}} \tag{2.11}$$

Combination of both geometries ensures that the forces of the internal gel ($\sim 1nN$) are slowed down by the antagonistic forces of the second geometry. So forces nearly balance each other out to account for the small counter-acting external force in vivo ($\sim 50pN$). But in the case, that the external forces increase, there would be still enough energy stored within the comet tail to move the bacterium forward as discussed for the second geometry. Again, the speed of the bacterium is much more stable in comparison to the first geometry even though the internal gel is also present. An important note is that polymerization speed is force dependent and depends on the normal stresses generated at the bacterium's surface [64]. Otherwise the occurring deformations would be too large and non realistic.

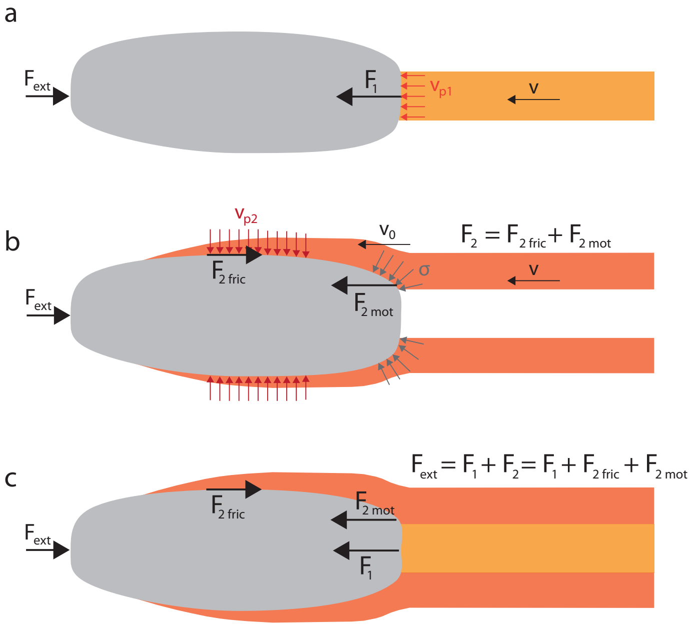

Figure 2.3: A continuum elastic model describes force generation by internal stress release. Two different actin gels emerge at the bacterium's surface. The force balance of both gels separately is shown in a) and b). The force balance of the whole system is shown in c).

This theoretical description is the first approach considering the interactions between different filaments and also includes elastic properties resulting from internal crosslinking or tight binding to the surface. So far the model was only applied to the propulsion of Listeria. It remains open if elastic effects like the soap effect can be applied to lamellipodial protrusion or negative bending of cell membranes upon actin polymerization. The mathematical modeling of the membrane localized actin polymerization in Chapter 4 is only based on the assumptions of the Brownian Ratchet model. But a mesoscopic description could reveal if density gradients within the network can lead to stress gradients resulting in different deformations of the actin gel dependent on the orientation of the density gradient.

2.1.2 *Biochemical and physical strategies to steer cell movement*

Parameters like network density, architecture or filament orientation determine final force transduction of the polymerizing network and migration processes. Directed cell migration is driven by the formation of a leading edge and thus requires spatially controlled actin polymerization at the membrane [19, 157]. Cells contain a complete and versatile signaling machinery to control network localization at the membrane [18, 78]. For example nucleation promoting factors (NPFs) such as VCA are activated by the Rho GTPases Rac and Cdc42 [78]. The VCA domain of N-WASP complex in turn activates the Arp2/3 complex. Thereby, the number of pushing filaments can be controlled. Likewise the negative feedback of filament nucleation is controlled by Rac. It also seems to activate Arpin, which inhibits Arp2/3 activity [38].

Over the past years evidence was found that internal forces due to actin polymerization or externally applied forces modulate network organization and such have a direct feedback on cell motion [109, 157]. Experiments demonstrate that external forces directly affect growth velocity and such have a direct feedback on network architecture resulting from mechanical reorganization. When an increasing force is applied to a dendritic network during growth, network protrusion remains at first constant until the velocity decreases to zero [112]. These observations can be explained by a microscopic remodeling of the network. The membrane localized network can be split in two regions. First a semiflexible region, where single filaments push against the membrane and are not crosslinked. Second a stiff region behind the semiflexible one, where filaments are crosslinked and serve as a stable base. If the force load increases, the size of the semiflexible region decreases so that filaments get compressed. Higher forces are transmitted and the growth velocity remains constant at first until the external load becomes too high. Then the growth velocity decreases to zero and the network stalls [171]. In accordance, recent experiments confirm that an increasing external load increases network stiffness and failure on a macroscopic level. On a microscopic level, network density and geometry changed leading to increased network stiffness and resistance [17]. This force feedback system makes cells more resistant and reliable as they are able to adapt quickly to changing external conditions.

Also the interdependence between filament density and the resulting network protrusion can control actin based motility. When network density is too high protrusion velocity decreases due to local monomer depletion. Also spatial arrangement of network nucleation affects protrusion. Protrusion velocity increases with higher nucleation density as force transduction was more efficient. Thus cells could create network protrusion gradients by controlling network or

nucleation density and such steer their directionality [22].
To control microscopic network architecture, a whole set of proteins is present in cells. One key player is Capping Protein (CP), which terminates filament growth by binding to filament barbed ends and such promotes filament nucleation by shuffling actin monomers towards Arp2/3 complex. Thus, CP enhances actin based motility by promoting Arp2/3 mediated filament nucleation [6]. Moreover, the presence of CP ensures directed network growth. In the absence of any CP, starlike actin patterns with filaments pointing towards all directions grew from a micro-patterned surface, whereas the presence of CP led to the formation of spatially constricted and fast protruding dendritic network cylinders [52]. Also, surface localized network nucleation and growth is controlled by CP. Dendritic network formation around beads, indicates that only in the presence of sufficient CP network growth is fully restricted towards the bead surface and a closed dense actin shell forms around the bead [5, 159]. If the internal stress become now too high, due to continuous polymerization at the surface, the actin shell breaks up and a symmetry break occurs. As a result, a comet tail forms on one bead side , which generates enough force for bead propulsion. Shell rupture often start at local network defects, which could be also triggered by local photo damage [173]. The cell could trigger symmetry breaking by locally disrupting the network polymerization.
Presence of VASP or formins leads to a full rearrangement of network architecture. VASP prevents filament ends from being capped by CP. Thus filament branching is less pronounced and parallel filament elongation is favored. The resulting protrusion speed is faster, but less persistent compared to dendritic networks [78]. The reason is that long filaments are more flexible than short branched filaments. Thus they have the tendency to align parallel to the membrane when the external load becomes too high and cell movement stops [14]. Together with actin crosslinkers like fascin, they form stiff actin bundles composed of about 20 filaments, which create sufficient force to locally push the membrane forward to form a filopodium[160]. The presence of crosslinkers like α-actinin, filamin, but especially fascin stiffens filopodia like structures and makes them more resistant against external load. Likewise, dendritic networks are stabilized by crosslinkers as the time to induce a symmetry break increases with an increasing crosslinker concentration due to the higher resistance against internal stresses [173]. But simultaneous growth of dendritic networks is slowed down in the presence of crosslinkers, probably due to the higher internal friction and decreased depolymerization. Encapsulation of Xenopus Laevis extract inside of droplets demonstrated that the presence of crosslinkers provided sufficient network connectivity to induce a symmetry break [4]. The here presented strategies of cells to adapt actin mediated force transduction allow them to adapt

quickly to any changes of their environment and to control their migration behavior [3].

2.2 PHASE TRANSITION BEHAVIOR IN COMPOSITE MEMBRANES

2.2.1 *Thermodynamic behavior of lipid membranes*

Cellular membranes are composed of different types of double-chained phospholipids [172]. Lipids, in general, are amphipatic, as they posses a polar headgroup and a hydrophobic tail. The self-assembly of lipids into higher ordered structures is driven by the hydrophobic effect and leads to the formation of lipid bilayers and vesicles in an aqueous environment [7]. The self-assembled structures are fluid, as van der Waals forces and hydrophobic interactions, which hold together the membrane, are short-range and not as strong as a covalent or ionic bonds. The fluidity is determined by the strength of van der Waals and hydrophic interactions, which depends on the lipid head group, chain length and degree of saturation [69]. Dependent on the temperature, membrane fluidity undergoes a transition from a gel-like state below the miscibility temperature (T_M) to a liquid disordered phase (L_d) above T_M. This process is called a phase transition. T_Ms for different lipids are listed in Table 2.1. T_Ms are low for short lipid chains and unsaturated lipids. In case of a short chain length, the van der Waals interactions are lower and therefore a lower temperature is required to break up the gel phase. The presence of double-bonds in one of the fatty acids induces a kink in the lipid tail, so that the membranes are still fluid even at low temperatures due to the higher packing volume [7].

Besides the gel-L_d transition also the transition from a L_d state to a gaseous state is observed. Both phase transitions are discontinuous and therefore of first order. They can be theoretically described by the van der Waals equation of state. A more detailed description is given in the next subsection. The transition from a gel-like phase to a solid, crystalline phase is of higher order and continuous as the free energy curve at the transition point is continuous. All phase transitions, which have a discontinuity in the second or higher derivative of the free energy are of second or higher order [71, 132]. Another example for higher order transitions is the transition between two crystalline phases, which have different order of lipids. A mixing of unsaturated and saturated lipids leads to a more complicated thermodynamic behavior. Dependent on external parameters like temperature, the two lipid types can segregate into their own species. Two phases of different fluidity and lipid compositions occur. The presence of cholesterol complicates the lipid phase behavior even more as it preferentially interacts with fully saturated lipids. The reason is that saturated lipids prefer, like cholesterol, a more ordered envi-

LIPID CHAIN TYPE	HEADGROUP TYPE			
	PC	PG$^-$	PS$^-$	PE
Saturated				
Dilauroyl(12)	-2	0	13	30
Dimyristoyl(14)	23	24	36	49
Dipalmitoyl(16)	41	55	68	74
Distearoyl(18)	55	55	68	74
Unsaturated				
Dioleoyl(18)	-22	-18	-7	-16

Table 2.1: Transition temperatures T_M for different Phospholipid. The number of C-atoms is written in brackets behind the lipid chain type. T_M is given in °C. The Table was compiled from D. Marsh [92].

ronment due to their small packing volume. The interaction between cholesterol and saturated lipids leads to the formation of a new lipid phase, which is called liquid ordered phase (L_o) and resembles to the cholesterol rich 'lipid rafts' found in biological membranes [135]. The L_o phase is less fluid and their structure is more ordered compared to the L_d phase. Below a certain temperature T_M, membranes, containing a ternary lipid mixture (an unsaturated lipid type, a saturated lipid type and cholesterol), the phase separate into a L_d and L_o phase. In the last part of this thesis, a protocol to form phase separated vesicles was developed and the behavior of phase separation was characterized. The observed behavior can be described by a thermodynamic model. The theoretical approach behind lipid-lipid de-mixing is described in Section 2.2.3.

2.2.2 *First order phase-transitions in homogeneous membranes*

In this section the basic thermodynamics of membranes composed of one lipid type are discussed. Dependent on external parameters like lateral pressure, area or temperature they undergo different phase transitions. The main first-order transitions are first, from a gaseous phase, where lipid-lipid interactions are weak, to the L_d phase, where lipids get closer packed and increase their interaction, second from the L_d to a gel-like phase, where the interactions between lipids are strong. Theoretically, the phase transition behavior of two-dimensional and three-dimensional systems is described by the van der Waals equation of state.

$$(\Pi + \frac{aN^2}{A^2})(A - Nb) = Nk_BT \tag{2.12}$$

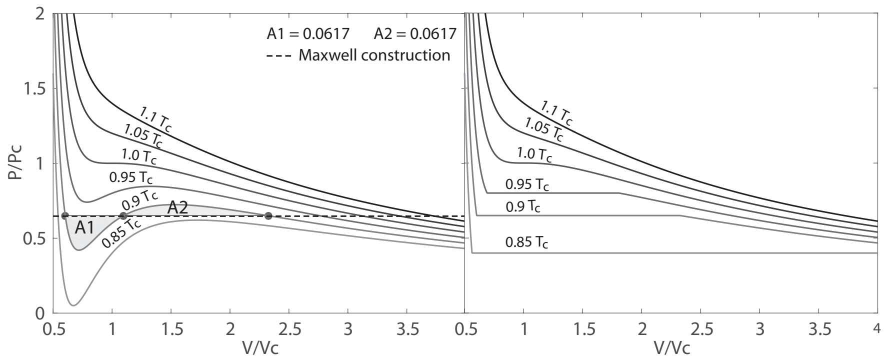

Figure 2.4: The reduced van der Waals equation is plotted for different temperatures. All quantities are normalized to their critical point. The axis are labeled with the volume and pressure.The Maxwell construction is shown for the isotherm T = 0.9 $\mathrm{T_C}$.

This equation is an extension of the ideal gas law and sets the $\Pi =$ lateral pressure, the $A =$ area, the $T =$ temperature and the $N =$ number of particles in relation to each other. The two constants a and b are the van der Waals constants and specific for every lipid type. The constant a is a measure of the van der Waals forces between the lipids and b gives the excluded area. Phase separation occurs below the critical point. The critical point is defined by the point, where the first and second derivation of Π after A are equal to zero. The critical variables are $A_c = 3Nb$, $\Pi_c = \frac{1}{27}\frac{a}{b^2}$,$k_B T_c = \frac{8}{27\frac{a}{b}}$ and are used to find the reduced van der Waals equation. Thereby, $\mathrm{T_C}$ is equivalent to $\mathrm{T_M}$. The reduced van der Waals equation is usually used to plot van der Waals isotherms in a PA-diagram at different temperatures, as it does not include any material specific parameters (Figure 2.4).

$$\Pi = \frac{8T}{3A-1} - \frac{3}{A^2} \tag{2.13}$$

Coming from a high area, the lateral pressure increases continuously. Below $\mathrm{T_C}$, the isotherms show non-physical behavior, where an additional reduction of area leads to a pressure decrease. Here, the phase transition takes place and the locally thermodynamically stable state is a combination of two phases (either gaseous and $\mathrm{L_d}$ phases or $\mathrm{L_d}$ and gel like phases). Even though the pressure seems to vary in the isotherms, it must remain constant, as the free energy is constant during the phase transition [132]. To find the right transition pressure, the Maxwell construction must be applied: Here, a straight line is constructed trough the isotherm such that the two areas enclosed by the line and the PA-curve equal each other out (Figure 2.4) as no energy is consumed nor generated by applying the Maxwell construction. This can be applied to all isotherms below $\mathrm{T_C}$, to retrieve the transition pressure and to construct the final isotherms. Here, the lateral pressure remains constant during the phase transitions [8] and the final isotherms are in accordance with experimentally measured isotherms.

2.2.3 *Unmixing of in-homogeneous membranes*

Phase transitions of composite systems are far more complicated and can be described by looking at the free energy. Examples of such systems are binary and ternary membrane compositions. They are completely miscible above T_M and separate in phases of different fluidity and composition below T_M. The equilibrium state of the system depends on its composition and the temperature. It is defined by the balance between entropy and energy. This balance is reflected in the free energy of a system. For systems at constant volume the appropriate free energy is the Helmholtz energy $F = U - TS$, whereas for systems at constant temperature, the Gibbs free energy $G = U - TS + PV$ is the adequate choice. In this section, we stick to isochor, binary system with lipids of type A and B. To calculate the phase diagram we need to determine the Helmholtz free energy of mixing (F_{mix}) dependent on temperature and lipid composition.

$$F_{\text{mix}} = F_{\text{A+B}} - (F_{\text{A}} + F_{\text{B}}) \tag{2.14}$$

$F_{\text{A}} + F_{\text{B}}$ describes the total free energy of the system before mixing and $F_{\text{A+B}}$ is the free energy of the mixed system. To calculate the total free energy, first the S_{mix} must be determined. The famous Boltzmann formula ($S = -k_{\text{B}} \sum_i p_{\text{i}} ln p_{\text{i}}$) can be used for that.

$$S_{\text{mix}} = -k_{\text{B}}(\Phi_{\text{A}} ln \Phi_{\text{A}} + \Phi_{\text{B}} ln \Phi_{\text{B}}) \tag{2.15}$$

Thereby a mean-field approximation was used as the assumption was made that every lipid position can be either occupied by the species A or B independent of their neighbor. Φ gives the volume fraction of every species. Second, we need to determine the U_{mix}. Here, the following assumptions are made: (1) energetic interactions can only occur between lipids in direct neighborhood and (2) the number of neighbors is the sum of $z\Phi_{\text{A}}$ and $z\Phi_{\text{B}}$ neighbors, independent if the site is occupied by lipid A or B, which is again a mean-field approximation. The interactions of energy between lipids of the same type are described by ϵ_{AA} and ϵ_{BB}. Interactions between different types of lipids are described by ϵ_{AB}. Subtraction of the inner energy at the mixed state from the unmixed state give the total inner energy of mixing.

$$U_{\text{mix}} = \frac{z}{2}[({\Phi_{\text{A}}}^2 - \Phi_{\text{A}})\epsilon_{\text{AA}} + ({\Phi_{\text{B}}}^2 - \Phi_{\text{B}})\epsilon_{\text{BB}} + 2\Phi_{\text{A}}\Phi_{\text{B}}\epsilon_{\text{AB}}] \tag{2.16}$$

By defining an interaction parameter $\chi = \frac{z}{2k_BT}(2\epsilon_{AB} - \epsilon_{AA} - \epsilon_{BB})$, which characterizes the energy between A and B relative to their self-interaction, U_{mix} can be simplified.

$$U_{mix} = \chi\Phi_A\Phi_B \tag{2.17}$$

The resulting F_{mix} is can be calculated from S_{mix} and U_{mix} by using the Helmholtz formula.

$$\frac{F_{mix}}{k_BT} = \Phi_A ln\Phi_A + \Phi_B ln\Phi_B + \chi\Phi_A\Phi_B. \tag{2.18}$$

This gives us now a formula, which allows us to plot the free enery dependent on its composition and interaction parameter. F_{mix} is plotted against the volume fraction of one lipid type. We assume that $\Phi_A + \Phi_B = 1$ and therefore when $\Phi_B = \Phi$ then $\Phi_A = 1 - \Phi$ (Figure 2.5). The free enery curve depends on the interaction parameter χ. At values of $\chi \leq 2$ only one minima is observed, whereas the curves have two minima and one maxima for values $\chi > 2$ (Figure 2.5).

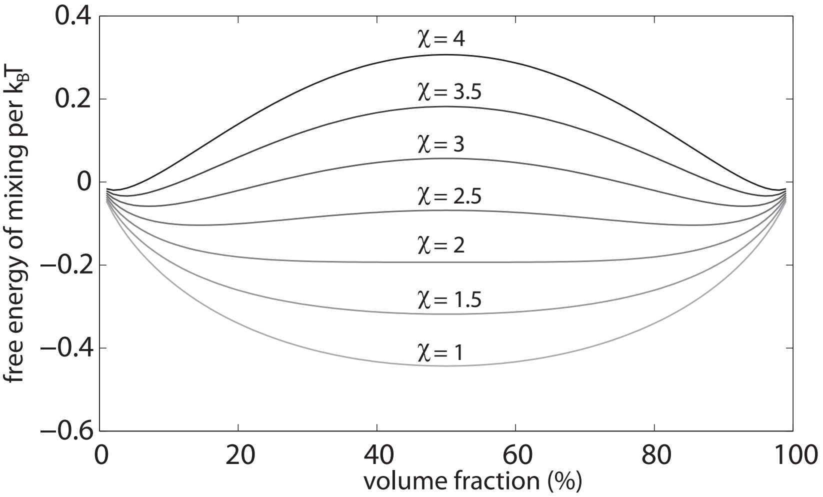

Figure 2.5: The free energy is plotted for different interaction parameters χ.

In order to correlate the curve trend to its physical meaning, we consider certain volume fraction Φ_0 of one lipid type e.g. type A. When this mixture phase separates into two phases, one phase has the volume V_1 and the volume fraction Φ_1 of lipid type A. The other phase has the volume V_2 and the volume fraction Φ_2 of lipid type A. Then due to the mass conservation: $\Phi_0 V_0 = \Phi_1 V_1 + \Phi_2 V_2$. Therefore we can write $\Phi_0 = \alpha_1\Phi_1 + \alpha_2\Phi_2$ where $\alpha_1 + \alpha_2 = 1$. The free energy of separation for this system is given by $F_{sep} = \alpha_1 F_{mix}(\Phi_1) + \alpha_2 F_{mix}(\Phi_2)$ and can be rewritten by using the expressions for Φ_0.

$$F_{sep} = \frac{\Phi_0 - \Phi_2}{\Phi_1 - \Phi_0} F_{mix}(\Phi_1) + \frac{\Phi_1 - \Phi_0}{\Phi_1 - \Phi_2} F_{mix}(\Phi_2) \tag{2.19}$$

Graphically, F_{sep} can be read by the double tangent construction when the mix starts to separate into the two fractions Φ_1 and Φ_2 from its starting position Φ_0, so that the total free energy of separation is given by the straight line joining $F(\Phi_1)$ and $F(\Phi_2)$.

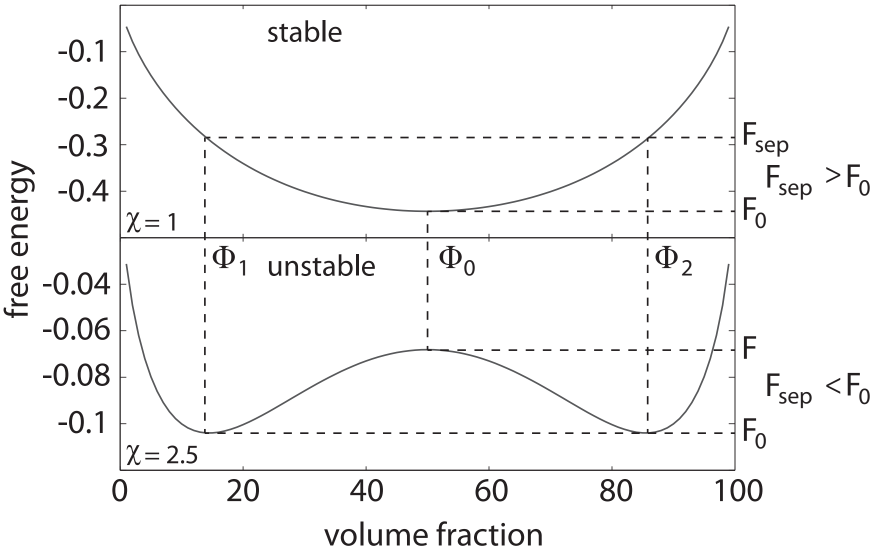

Figure 2.6: The free energy is plotted for a stable mixture ($\chi = 1$) and unstable mixture ($\chi = 2.5$). Φ_0 is the starting volume fraction of one lipid type, which can phase separate into two subfractions Φ_1 and Φ_2. F_{sep} is higher than the starting free energy for $\chi = 1$. Therefore lipid segregation is not favored and the mixture remains stable. F_{sep} is smaller than the starting free energy for $\chi = 2.5$ and thus the lipid mixture separates into the fractions Φ_1 and Φ_2.

In case of $\chi \leq 2$ the curve is concave and F_{sep} would be always higher than F_0 (Figure 2.6). Therefore phase separation is not favored and the mixtures remains stable. In case of $\chi > 2$ the curve also shows convex areas. Here F_{sep} is lower than F_0, when the starting composition Φ_0 is in between the two minima and thus the mixture is no longer stable (Figure 2.6). Phase separation into Φ_1 and Φ_2 occurs.
The area between the two minima is the coexistence area of the composite system, in which mixing is not stable and two subfractions Φ_1 and Φ_2 coexist. The binodale separates stable from unstable mixtures and is defined by $\frac{dF}{d\Phi} = 0$. The spinodal is set by $\frac{d^2F}{d\Phi^2} = 0$ and subdivides the coexistence area in metastable and unstable mixtures.

Both the binodale and spinodale can be drawn into a phase diagram dependent on the volume fraction Φ of one lipid type and χ(Figure 2.7). The fix point of the binodale and spinodale is known as the critical point and definded by $\frac{d^3F}{d\Phi^3} = 0$. Unstable mixtures are characterized by a spinodal decomposition. Here local concentration fluctuations are sufficient to induce phase separation and lead to a continuous change in the composition. Demixing in metastable mix-

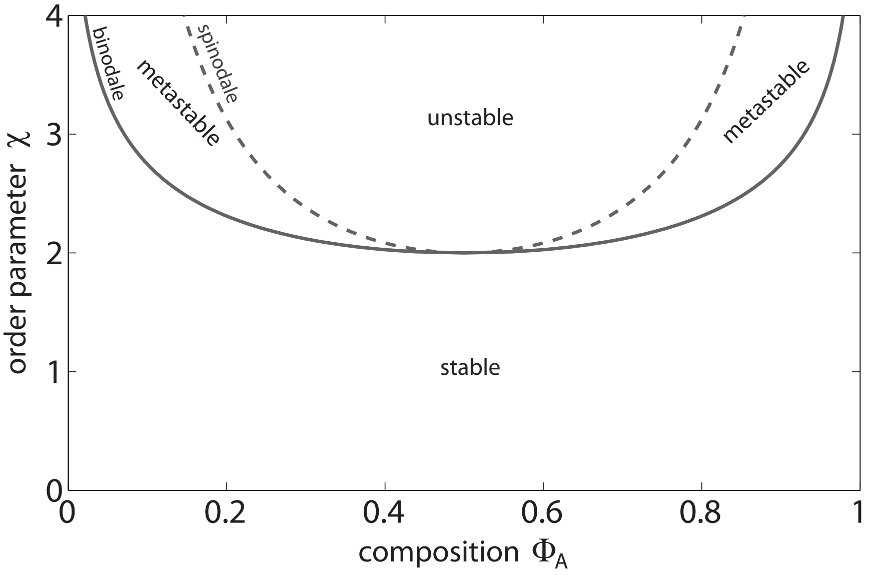

Figure 2.7: The phase diagram calculated from Equation 2.18 is plotted against the composition of Φ_A. The binodale is defined by $\frac{dF}{d\Phi} = 0$ and the spinodale by $\frac{d^2F}{d\Phi^2} = 0$.

tures occurs only at large concentration fluctuations and cannot be induced by small fluctuations. This process is called homogeneous nucleation. Most system are not free from impurities and they can already phase separate at lower activation energies as the impurities serve as nucleation seeds for separation. Both process are described in more detail in chapter 3 of [71]. In our case the energy function is symmetric and therefore the condition for the double-tangent construction can be simplified to $\frac{dF}{d\Phi} = 0$. But it must be pointed out that this definition is not general and holds only for the symmetrical case. Naturally the chemical potential must be constant for every phase and by that defines the condition for the double tangent construction.

To draw a conclusions from our phase diagram we must look at the interaction parameter χ. If we assume that the energetic interactions are temperature independent and χ is proportional to $\frac{1}{T}$, we can conclude that the composite system is stably mixed at high and decomposes at lower temperatures in the here presented system.

Part III

MATERIALS AND METHODS

3

MATERIALS & METHODS

Bottom up approaches allow the study of the mechanisms behind complex cellular behavior. To study cytoskeletal dynamics, all proteins of interest must be purified either recombinantly from E.coli cultures or directly from tissue. An elegant and more physiologic alternative to purified proteins is the use of Xenopus extract, as it contains all proteins of the cytoplasm and is easy to manipulate. For example over-expression of a certain protein is simply achieved by the addition of purified proteins. GUVs are used to mimic the cell membrane and to study their interaction with the cytoskeleton. CDICE is currently the most promising method to encapsulate purified proteins or Xenopus laevis extract to study not only protein membrane interaction but also the influence of confinement. The encapsulation method is fast, requires small protein volumes despite the high encapsulation efficiency, is low cost and easy to implement [1]. In this work I was able to encapsulate complex purified protein systems, to develop an encapsulation protocol for Xenopus laevis extract and a protocol for the formation of phase separated vesicles.

3.1 PURIFIED PROTEINS

3.1.1 *Actin*

Actin is one key component of the cytoskeleton in cells and indispensable for various cellular processes like migration, adhesion or endocytosis. It is a globular protein and 42 kDa large. Upon addition of divalent ions, actin monomer (G-actin) polymerizes and forms filamentous actin (F-actin). G-actin is purified from rabbit skeletal muscle by a already published protocol [141]. An additional gel filtration step is performed to separate the monomer fraction from minor contaminants. One part of the purification is stored at 4 °C in G-Buffer (2 mM Tris, 0.2 mM ATP, 0.2 mM CaCl2, 0.2 mM DTT and 0.005% NaN3, pH 8.0) and ready to use. Fresh actin is used for 1 week. The other part is lyophilized to store longterm. For experiments lyophilized actin is dialyzed overnight against G-buffer. The buffer is exchanged 3 times in the first three hours. The next day it is centrifuged for 2 h at 90000 g to remove any small actin filaments. The supernatant containing G-actin is stored at 4°C and can be used for 1 week. For fluorescence microscopy 10% of the G-actin is replaced with covalently labeled actin. It is labeled with Atto 488 NHS-ester (Jena Bioscience) at cysteine 374 [75]. For pyrene assays 20% of the actin monomers are replaced with pyrene-actin. Pyrene actin are actin monomers, which are covalently bound to N–(1-pyrenyl)iodoacetamide [36]. For polymerization, actin monomers are transferred into a 10x polymerization buffer (100 mM imidazole, 30 mM MgCl2, 300 mM KCl, 10 mM EGTA, pH 7.4).

3.1.2 *Arp2/3-complex and VCA*

Arp2/3 complex mediates dendritic network growth in the lamellipodium during cell migration. The same nucleation and growth processes are also thought to be responsible for the formation of negative curvatures in the plasma membrane as found in endocytosis. Thereby, the Arp2/3 complex must be activated by the VCA domain of WASP. WASP itself is activated by different signal-transduction pathways for example by Rho family GTPases CDC42 [55, 63]. The Arp2/3 complex is 224 kDa large. Arp2/3 complex is extracted from pig brain and purified as described previously [41]. It is fluorescently labeled by adding a 3-fold excess of maleimide Atto 647N dye (Atto-Tec) and incubated while rotating for 2 h at -4°C. Finally, the reaction is stopped by the addition of 1 mM DTT and the excess dye is removed by a NAP size exclusion chromatography column (NAP-25 Columns, GE Healthcare). The C-terminal VCA domain of murine N-WASP is expressed in BL21 Codon Plus DE3-RIPL (Agilent Technologies) as a histidine-tagged protein overnight in LB medium. After purification by Ni-NTA affinity chromatography in SoniBuffer (50 mM Na2HPO4, 50 mM NaH2PO4·2H2O, 300 mM NaCl, pH 8.0), the protein is dialyzed against storage buffer (20mM Tris/HCl, 100mM KCl, 1mM MgCl2, 5mM EGTA, 2 mM DTT, pH 7.0) and stored at -80 °C. The histidine-tag is kept to enable the binding of VCA to Ni-NTA-lipids. His-Tagged VCA is 12 kDa large.
For labeling VCA is dialyzed overnight against 20 mM Tris/HCl (pH 7.4), 100 mM KCl, 1 mM $MgCl_2$, 2 mM EGTA, 2 mM TCEP. The next day VCA is incubated with a 3-fold excess of maleimide dye Atto 647 N (Atto-Tec) for 2 hours at 4°C. Afterwards, it is quenched by 1 mM DTT and the excess dye is removed by size exclusion chromatography using a NAP-25 column (GE Healthcare).

3.1.3 *Non-muscle myosin II*

Myosin II is not only found in muscle cells, but also in all non-muscle eukaryotic cells [158]. This type of myosin II is called non muscle myosin II (NMMII). Like skeletal muscle it forms bipolar filaments and builds a contractile unit when bound to actin. The contractile forces are smaller compared to muscle myosin II due to a smaller filament size and thickness. But they are sufficient to induce cellular reshaping and movement. Moreover, their small filament size ensures a higher flexibility when diffusing through the cytoplasm to ensure a fast transport to the force active regions of the cell [105]. Non muscle myosin is purified from human blood platelets and stored at -20 °C in 60% sucrose following a standard protocol [118]. The molecular weight of 200 kDa is estimated from electrophoresis gels to calculate the molar concentration of NMMII.

3.1.4 *Profilin*

Profilin is a small globular protein, 15 kDa large and a nucleotide exchange factor for actin. It ensures the ADP to ATP exchange of actin monomers and such maintains the ATP-actin-profilin pool. It promotes filament assembly at the fast growing plus end of actin filaments and suppresses any polymerization at the slow growing minus end. When filament plus ends are as well blocked, polymerization is completely suppressed in the presence of profilin. Filament elongation is also completely suppressed in the absence of any actin seeds and the presence of profilin [119]. For this study mouse (mPfn2a) is cloned in pGex-6P-2 and expressed in BL21 Codon Plus DE3-RIPL (Agilent Technologies) as a glutathione S-transferase (GST) fusion protein. After its purification it is dialyzed against 20 mM Tris (pH 7), 150mM NaCl, 1 mM DTT and stored at 4 °C. The GST-tag is removed by proteolytic cleavage after purification.

3.1.5 *Capping Protein*

CP is 63 kDa large and terminates filament elongation at the fast growing actin filament end by binding to it [119]. The mouse $\alpha 1$ and $\beta 2$-subunits of CP cloned into pRSFDuet$^{\mathrm{TM}}$-1 (Novagen) are expressed in BL21 Codon Plus DE3-RIPL (Agilent Technologies) and purified using flag-tag affinity chromatography [44]. The cells are grown at 37°C until the optical density reached 0.6 at $\lambda = 600nm$. The expression is induced by the addition of 0.5 mM IPTG and shaking is continued overnight. The cells are harvested and resuspended in 20 mM Tris (pH 8.0), 250 mM NaCl, 1 mM EDTA and 5% glycerol. After centrifugation (30000 rpm, 10 min, 4°C) the supernatant is mixed with 100 µl ANTI-FLAG M2 Affinity Gel (Sigma Aldrich) per 100 ml supernatant, rotated for 90 min at 4 °C and then centrifuged at low speed (500 rpm). Beads are washed several times with the same buffer before adding 100 μl FLAG peptides (Sigma Aldrich F3290-25mg lyophilized powder) per 1 ml buffer. After 1h incubation on a rotating wheel at 4 °C, they are centrifuged for 2 min at 14 000 rpm. The supernatant, containing CP, is dialyzed overnight against 10 mM Tris/HCl (pH 8.0), 50 mM KCl and 1 mM DTT, then flash-frozen in liquid nitrogen and stored at -80 °C.

3.1.6 *Vasodilator stimulated phosphoprotein*

Vasodilator Stimulated Phosphoprotein (VASP) is an actin elongator and mostly found in focal adhesions, the leading edge of lamellipodia and filopodial tips [14]. It is 43.5 kDa large and was shown to promote filament elongation most efficiently as a tetramer [26]. Human VASP is used in this work, but the GAB domain is replaced by the fast elongating GAB domain of Dictyostelium discoideum (hVASP dGAB) [25]. In order to bind hVASP dGAB to artificial membranes by the interaction between NiNTA and His-Tag, the whole construct is cloned into pET-28a (Novagen) and expressed in BL21 Codon Plus DE3-RIPL (Agilent Technologies). The cells are induced with 1 mM IPTG, after grown to an optical density of 0.6-0.8 at 37°C. Proteins are expressed over-night at 21 °C. The next day cells are harvested at 4600 g for 20 min at 21°C. The cells are resuspended in lysis buffer (PBS (pH 7.8), 2 mM DTT, 1 mM EGTA), 200 μl lysozym (20 mg/ml), one tablet Complete per 50 ml cells (Roche) and 5 μl Benzonase, when purification is started immediately. Otherwise they can be stored at -80 °C. The cells are disrupted 2-3 times either with the cell disruptor or a french press. Afterwards they are centrifuged at 4°C and 17000 rpm for 30-45 min and the supernatant is filtrated. Then the NiNTA resin is added to the supernatant and it is rotated for 1 h at 4 °C. The supernatant is pipetted on a column and first washed with the lysis buffer plus 20 mM immidazole and second with lysis buffer plus 50 mM immidazole. To elute the His-Tagged hVASP dGAP from the NiNTA resin the column is washed with lysis buffer plus 500 mM imidazole. Last a buffer exchange to the VASP storage buffer (PBS (7.6), 2 mM DTT) is done with a NAP-25 column (GE Healthcare). The protein is shock-frozen in liquid nitrogen and stored at -80 °C. To covalently label VASP with Atto 647N maleimide, the protein is directly dialyzed overnight against labeling buffer (PBS (pH 7.4), 2 mM EGTA, 2 mM TCEP). The next day it is incubated with a 10x excess amount of Atto 647N maleimide and rotated for at least 2 h at 4°C. Afterwards it is quenched by 1 mM DTT and the excess dye is removed by size exclusion chromatography using a NAP-25 column (GE Healthcare). The NAP-25 column needs to be equilibrated in the final storage buffer (PBS (7.6), 2 mM DTT). The protein is shock-frozen in liquid nitrogen and stored at -80 °C.

3.1.7 *Fascin*

Fascin is a 55 kDa large parallel actin crosslinker. It is necessary for filopodia and protrusion formation, as it provides them with the necessary stiffness [160]. In vitro fascin organizes actin filaments into networks of bundled filaments [84]. Human fascin was cloned in pGex-4T-3 and recombinantly expressed in [159]. It is stored in 2 mM Tris/HCl (pH 7.4) and 150 mM KCl at -80°C.

3.1.8 *α-actinin*

α-actinin is a homodimer and is found in the z-disc of muscle cells or in stress fibers [139]. Each subunit is about 100 kDa large and arranged in an antiparallel orientation [147]. It cross-links actin filaments in various angles and as such retains a certain network flexibility [37]. It was also shown that activity of α-actinin is calcium dependent [49]. For this work the calcium-insensitive isoform α-actinin 1b is cloned into pET-28c (Novagen) and recombinantly expressed in BL21 Codon Plus DE3-RIPL (Agilent Technologies) [50]. It is stored in 20 mM TES (pH 8), 150 mM NaCl and 2 mM DTT at -80°C.

3.1.9 *Pyrene Assays*

To verify protein quality and activity, pyrene assays were regularly performed. Here 20% of G-actin are replaced by covalently labeled pyrenyl actin. Pyrene actin is excited at 365 nm and emits at 407 nm. When actin is in the filamentous form, the fluorescence intensity increases about 20 times compared to monomeric actin. Therefore, pyrene-actin is an excellent candidate to study the polymerization kinetics of actin in the absence or presence of various ABPs [36]. The polymerization assays were performed with the microplate reader SpectraMax M5 (Molecular Devices).

3.2 PREPARATION OF XENOPUS LAEVIS EXTRACT

The extract is produced from freshly laid eggs of Xenopus laevis frogs. 500-800 units of Ovovgest 1000I.E./ML (Choriongonadotropin) are injected into the dorsal lymph sac. The frogs are incubated overnight in water at 18-21 °C and start to lay eggs about 12-16 h later. The eggs are either freshly squeezed or alternativly, when the frogs were incubated in high-salt MBS buffer (5 mM HEPES, 2.5 mM $NaHCO_3$, 1 mM $MgSO_4$, 1 mM KCl, 108 mM NaCl, 700 μM $CaCl_2$, pH 7.8), the naturally laid eggs can be used. The Xenopus laevis egg extract is prepared without cytocalasin D to keep actin polymerization active. It is prepared according to a modified protocol [162]. All buffers must be freshly prepared besides MBS. A stock solution of 20x XB salts (2 M KCl, 20 mM $MgCl_2$, 2 mM $CaCl_2$) is prepared. Also a protease inhibitor mix, which consists of 10 mg/ml leupeptin, 10 mg/ml pepstatin A, 10 mg/ml chymostadin dissolved in DMSO, is prepared in advance and stored at 4°C. Eggs are collected in MBS high salt buffer and washed at least three times with MBS (5 mM HEPES, 2.5 mM $NaHCO_3$, 1 mM $MgSO_4$, 1 mM KCl, 88 mM NaCl, 700 μM $CaCl_2$, pH

7.8) until the buffer remains clear. Eggs must be kept in the buffer at all times. Before the addition of the dejellying solution (1x XB-salts, 2% cysteine, pH 7.8), to remove the jelly coat, all excess MBS is removed. The beaker is gently shaken during dejeylling until the eggs are tightly packed and the jelly coat is completely removed. The whole process takes about 5-7 min. Afterwards, the eggs are washed first with XB-buffer (10 mM HEPES, 100 mM KCl, 1 mM MgCl$_2$, 0.1 mM CaCl$_2$, 50 mM sucrose, pH 7.7), then with CSF-XB (200 ml XB plus 1 mM MgCl$_2$ and 5 mM EGTA) and finally with CSF-XB+ (50 ml CSF-XB plus 50 μl of LPC). Next, the eggs are transferred into a SW-55 thin-wall tube with a cutoff fire-polished Pasteur pipette. The eggs have to be covered by buffer all times, as exposure to air can damage them. The loaded tube is inserted into a 13 ml Sarstedt adapter tube, filled with 0.5 mL water, before centrifugation to prevent a collapse of the tube during centrifugation. In a table top centrifuge the eggs are more closely packed for 1 minute at 200 g, for 30s at 500 g. Afterwards the excess buffer is removed before the eggs are crushed at 18000 g at 16°C and stored on ice. The eggs separate in four layers Figure 3.1. The third layer from the top is the actin-intact CSF extract. It is harvested with a syringe and stored on ice. The extract is supplemented with 1/1000 LPC and 1/40 of an energy mix (150 mM creatine phosphate, 20 mM ATP, 2 mM EGTA, 20 mM MgCl$_2$ stored at -20°C). Then it is centrifuged at 40000 g for 10 minutes at 4°C to clarify and remove any remaining lipids and pigments. The extract can be flash frozen and kept at -80°C for at least 4 month without loss of activity. Bulk gelation essays are immediately performed after extract preparation to verify acto-myosin activity. To this end 0.5 μl of the crude extract are pipetted into a mineral oil drop and imaged over time at room temperature with a phase contrast microscope. A clear contraction is be visible within the first minutes.

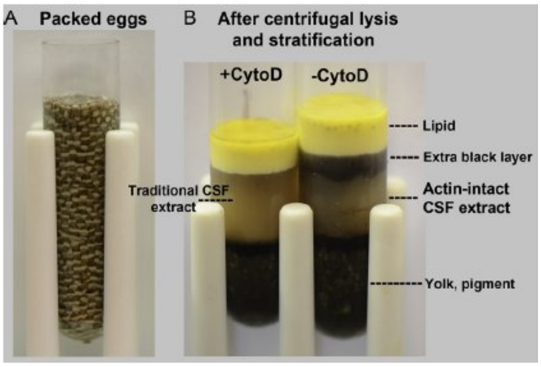

Figure 3.1: On the left side the Xenopus laevis eggs are shown before centrifugation and on the right side after centrifugation. The image is taken from [48]

3.3 SPATIAL NETWORK GROWTH ON A MONOLAYER

3.3.1 *Preparation of a monolayer*

The monolayers are prepared according to the protocol provided by ibidi. At first the desired lipids stored in chloroform (DOPC (Avanti Lipids, 850375), 10% Ni-NTA (Avanti Lipids, 790404C) and 2.5% PEG 2000 PE (Avanti Lipids, 880160C)) are mixed in a glass vial. The total amount of lipids is 1 mg. The chloroform is evaporated under the hood and the glass vial is stored under vacuum for several hours to remove any remaining traces of chloroform. Afterwards, the lipids are dissolved in a mixture of 70%/30% ddH2O/isopropanol and vortexed for 1 min. More isopropanol should be added if the mixture is not clear. 50 μl of the lipid mix are filled into a channel of an μ-Slide VI0.4 uncoated (ibidi, 80606). The channel is washed slowly with 1 ml ddH2O and rinsed quickly a few times with water to remove any traces of isopropanol.

3.3.2 *Polymerization of dendritic networks on the monolayer*

The monolayers are washed with VCA buffer (20 mM Tris/HCl, 100 mM KCl, 1 mM MgCl2, 5 mM EGTA, 2 mM DTT, pH 7.0) and incubated with 300 nM His-VCA. After 10 min the channels are extensively washed with VCA buffer to remove any unbound VCA. To prepare the branched network polymerization mix, 3 μM actin, 0.3 μM Arp2/3 complex, 13.5 μM profilin and the desired amount of CP are added to polymerization buffer (10 mM imidazole, 3 mM MgCl2, 30 mM KCl, 1 mM EGTA, pH 7.4). The mix is filled into the channels and imaging can be started immediately. To image the network growth 10% of unlabeled actin are replaced by Atto 488 actin. The polymerization mix is supplemented with 0.4% glucose, 0.18 mg/ml glucose-oxidase and 0.06 mg/ml catalase to minimize photobleaching of Atto 488.

3.4 GUV PREPARATION AND PROTEIN ENCAPSULATION

3.4.1 *Continuous droplet interface crossing encapsulation (cDICE)*

The method was first introduced by Abkarian et al. in 2011 and successfully encapsulates different protein system ranging from microtubules to actin inside of GUVs [74, 89]. For production, protein droplets are inserted into a rotating chamber by a glas capillary. The chamber is filled with three different layers: (1) The inner most layer controls droplet formation. (2) The second layer is an lipid-oil emulsion, where lipids adsorb to the water-oil interface due to their amphiphatic behavior and a first monolayer is formed. (3) The third layer is a glucose solution. At the interface between the lipid-oil emulsion and the glucose solution, a second monolayer is self-assembled. This monolayer zips together with the monolayer formed around the protein droplet. To detach the vesicles from the interface, a high density difference between the protein solution and the glucose solution is required. To this end, about 30% of the encapsulated volume are replaced by sucrose. The vesicles can be harvested with a pipette from the glucose solution. The osmotic pressure of the glucose solution must adapt to the protein solution to ensure the GUV's stability. The protein droplets are pushed trough the different layers by centrifugal forces induced by rotation of the cDICE chamber. A clear separation of the three layers is ensured by their different densities, which increase from inwards to outwards. The droplet and thus vesicle size is controlled by the balance between the drag force and surface tension.

$$F_{\mathrm{Stokes}} = F_{\mathrm{Surface}} \tag{3.1}$$

$$3\eta_1 v_1 d_{\mathrm{droplet}} = \gamma d_{\mathrm{cap}} \tag{3.2}$$

The final droplet diameter can be tuned by the the balance between the diameter of the capillary's tip and the the capillary number.

$$d_{\mathrm{droplet}} = A\frac{d_{\mathrm{cap}}}{C_{\mathrm{a}}} \tag{3.3}$$

The capillary number is defined as $C_{\mathrm{a}} = \frac{\eta v}{\gamma}$. Surface tension must be sufficiently high that stable droplets form at the capillaries tip and rip of as soon as the drag force becomes to high. This regime is called dripping regime and $C_{\mathrm{a}} < 1$. In summary, the diameter of the capillaries tip d_{cap}, speed of rotation v and the viscosity η of the solution in which the droplets are inserted, can be tuned to adjust the droplet diameter. For the encapsulation of the protein system used in Chapter 4 (Actin, Arp2/3 complex, VCA, profilin and CP) a diameter tip of 40 μm is used to avoid protein clogging, as polymerization is fast due to the presence of Arp2/3 and VCA. The speed of rotation is decreased to 1200 rpm and the viscosity is increased by addition of mineral oil. A mixture of 30% mineral oil and 70% decane is used. For the protein system studied in Chapter 5 (Actin, VASP, profilin and CP), a capillaries tip of 20 μm is used, as clogging appears less likely. Speed of rotation is 1800 rpm and 100% decane are used. Vesicles are produced for 5-10 min at 5 °C, when proteins are encapsulated. Otherwise production lasts until the capillary is empty. The vesicles are imaged 30 min after production and remain stable for several hours.

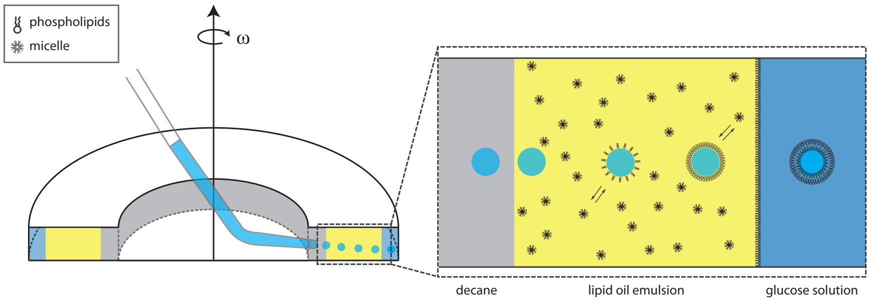

Figure 3.2: A scheme of the cDICE setup is shown.

3.4.2 *Preparation of Lipid-Oil emulsions*

Vesicle production by cDICE requires the formation of two monolayer, which then zip together to form a bilayer. The first monolayer assembles around the protein droplet, when passing the lipid oil emulsion and the second one self-assembles at the interface between the lipid-oil emulsion and the glucose solution. Especially, the second monolayer must regenerate continuously, to ensure defect free zipping. To this end, it is necessary to produce stable lipid-oil emulsions, which serve as an endless reservoir and ensure that lipids get adsorbed to the water oil interface due to their amphipatic behavior. The "solvent-shifting" effect is used to produce such stable lipid-oil emulsions [35]. Here, the lipids are dissolved in decane. Afterwards, an oil solution is added, in which the decane is soluble, but the lipids are not. This results in the formation of a micro-emulsion, where decane stabilizes the formation of lipid aggregates within the oil solution. Over time decane dissolves in the oil solution and the lipid aggregates are thought to consist purely of lipids. Aggregate size depends on the oil composition. The following protocol was used to produce lipid oil emulsions: A total concentration of 0.5 mM lipids are dissolved in a mixture of 14% mineral oil (Sigma Aldrich, M3516), 80% silicone oil (Roth, 4020.1) and 6% decane (Sigma Adlrich, D901) as previously described [89]. The final lipid oil mixture contains 85.7% EggPC (Sigma Aldrich, P3556), dissolved at 50 mg/ml in a chloroform/methanol mixture (9:1, v/v), 10% Ni-NTA (Avanti Lipids, 790404C) and 2.5% PEG2000 PE (Avanti, Lipids, 880160C). To label the membrane, 0.03% of the fluorescent lipid Texas Red (Thermo Fischer, T1395MP) are added to the lipid mix.

3.4.3 *GUV encapsulation of purified proteins by cDice*

The encapsulated protein solutions are mixed on ice, directly before vesicle production. To study the interaction of dendritic networks and membranes (Chapter 4), 3 μM G-actin, 300 nM VCA, 300 nM Arp2/3 complex, 13.5 μM profilin and the desired amount of CP are added to the polymerization buffer (10 mM imidazole, 3 mM MgCl2, 30 mM KCl, 1 mM EGTA, pH 7.4). 10% of unlabeled G-actin are replaced by covalently labeled Atto 488 actin to visualize the network structures by fluorescence. To measure the contractile behavior dependent on CP, 5 μM NMMII are added additionally to the encapsulation mix. Only, 300 nM VCA (25% are labeled with Atto 647N) are encapsulated in the absence of any other proteins to study effects of VCA clustering on domain formation. To study VCA induced Arp2/3 clustering, 300 nM of Arp2/3 (35% are labeled with Atto 647N) are encapsulated additional to 300 nM VCA. To reconstruct filopodia like structures at the membrane, 3 μM G-actin, 1 μM VASP, 60 nM CP and 13.5 μM Profilin are encapsulated. Again 10% of G-actin are replaced by covalently labeled Atto 488 actin. To study the influence of additional crosslinking on filopodia formation, 1 μM fascin is encapsulated. For colocalization assays between actin and VASP, 20% of VASP are covalently labeled with Atto 647N. In all experiments the amount of all protein buffers is kept constant. The osmotic pressure of the outside solution, which was prepared from 1 M glucose, is adapted 10 to 20 mosmol higher than the encapsulated solution.

3.4.4 *GUV encapsulation of Xenopus laevis extract by cDICE*

Before encapsulation, Xenopus extract must be diluted to prevent capillary clogging and avoid protein adsorption to the water-oil interface, as protein density is very high. For one vesicle preparation, a volume of 30 - 50 µl is required. The extract dilution is composed of 3.6 % extract, the desired amount of His-VCA and α-actinin (the maximum concentration is 30 μM of His-VCA and 2.4 μM of α-actinin), 11% sucrose solution (1 M) and the remaining volume is filled up with 10x diluted XB salts (2 M KCl, 20 mM $MgCl_2$, 2 mM $MgCl_2$). Everything is mixed on ice and vortexed directly before encapsulation to minimize phase separation of the extract into a protein-rich and protein-poor phase during encapsulation. The osmotic pressure of the extract dilution is measured before addition of the Arp2/3 activator His-VCA and α-actinin to prevent Arp2/3 activation and fast polymerization during the measurement. The osmotic pressure of the glucose solution in the cDICE chamber is adjusted 10 -20 mOsm higher than the extract dilution. The lipid composition of the lipid-oil emulsions is 87.2% DOPC (Avant Polar Lipids, 850375), 2.5% PEG2000 PE (Avanti, Lipids, 880160C), 0.3% PEG-Biotin (Avanti Lipids) and 10% Ni-NTA (Avanti Lipids, 790404C). To label the membrane 0.03% of the fluorescent lipid Texas Red (Thermo Fischer, T1395MP) is added to the lipid mix. A total concentration of 0.5 mM lipids is dissolved in an oil mixture composed of 24% mineral oil (Sigma Aldrich, M3516), 70% silicone oil (Roth, 4020.1) and 6% decane (Sigma Adlrich, D901). Higher amounts of mineral oil are used compared to the already published protocol [1], in order to increase the lipid aggregate size. This ensures fast lipid adsorption at the water-oil interface of the droplet. However, the higher mineral oil content decreases the emulsion's stability. Thus, it is recommended to prepare the lipid-oil emulsion directly before production. Vesicles are produced in the cold room at 5°C, a capillary with a tip diameter of 30 µm is used, the innermost layer in the cDICE chamber is composed of 100% decane and the speed of rotation is set to 1800 rpm.

3.5 FLUORESCENCE MICROSCOPY

3.5.1 *Epifluorescence and confocal microscopy*

Bright-field and epifluorescence images of the vesicles are taken by a 63× numerical aperture (N.A.) 1.3 oil immersion objective on a commercially built Leica Microscope DMI3000 B in combination with a Hamamatsu ORCA-ER camera. Confocal images are taken by a 63× N.A. 1.4 oil immersion objective with on a Leica TSC SP5. The temporal evolution is observed by acquiring 3D stacks of epifluorescence snapshots with a 100× numerical aperture (N.A.) 1.4 oil immersion objective or a 40x numerical aperture (N.A. 1.25-0.75) oil immersion objective on a commercially built Leica Microscope DMI3000 B. 3D Image acquisition is started one minute after finishing the encapsulation process. 3D snapshots of the vesicles are taken every three minutes with a epifluorescence microscope in order to avoid any artefacts by phototoxicity. Confocal and fluorescent images are used to measure the domain length and curvature by ImageJ. Actin domains at the membrane were counted with the 3D object counter provided by ImageJ.

3.5.2 *TIRF-microscopy*

Branched network formation on a supported lipid monolayer is imaged at room temperature on a commercially built TIRF microscope (Leica AF6000 Modular Systems, Leica). Images are taken with an iXon Ultra EMCCD camera (Andor).

Part IV

RESULTS AND DISCUSSION

4

CP CONTROLLED ACTIN POLYMERIZATION INDUCES MEMBRANE DEFORMATIONS

Actin, Arp2/3 complex and CP are encapsulated inside of GUVs to study the mechanical interplay between lamellipodia-like actin networks and a free standing membrane. Arp2/3 complex activation and consequently actin nucleation was localized to the membrane by coupling His-tagged VCA to Ni-NTA lipids and spontaneous actin polymerization within the vesicle's bulk was suppressed by CP and profilin. The encapsulated limited pool of actin monomers was responsible for the formation of inhomogeneous actin polymerization at the membrane. Two distinct network architectures emerged at the membrane, which induced either an outwards or inwards bending of the membrane. The appearance of the different shape deformations correlated to CP concentration. Only at high CP and in presence of the molecular motor non muscle myosin II (NMMII) membrane invaginations were induced that ultimately fissioned from the membrane. A detailed simulation of the underlying growth kinetics under depleting protein pool conditions showed that two distinct network patterns of actin growth emerged beneath the membrane. The resulting inhomogeneous growth velocity profile of the network led to the formation of membrane protrusions at low CP concentration and promoted negative membrane bending at high CP concentration. Altogether, CP controls membrane localized growth kinetics of actin mediated by Arp2/3 complex and such determines lamellipodia formation and the resulting membrane shape deformations.

4.1 MEMBRANE LOCALIZED POLYMERIZATION IS INDUCED BY ARP2/3 COMPLEX

CDICE was used to encapsulate actin monomers and ABPs into vesicles with a radius of 10-25 µm (Figure 4.1 a). The GUV's membrane was composed of EggPC and PEG-PE to prevent any non specific interactions. NiNTA lipids were incorporated into the membrane to bind His-tagged proteins.

Encapsulation of actin monomers alone resulted in the formation of a volume spanning network without any localization of the actin network to the membrane (Figure 4.1 b). Thus, His-tagged VCA, Arp2/3 complex and profilin were added to the polymerization mix prior to encapsulation in order to shift actin polymerization to the membrane. VCA, which activates Arp2/3, binds to NiNTA lipids via the His-tag and such shifts Arp2/3 mediated filament nucleation and

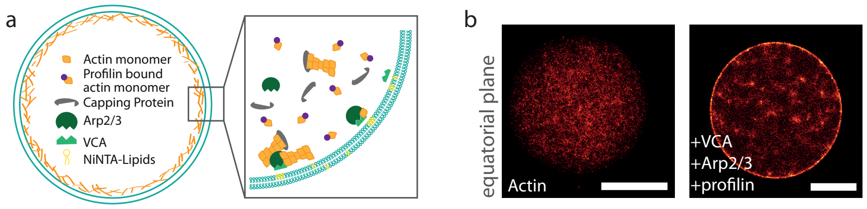

Figure 4.1: a) Molecular scheme with all components, required to produce cytoskeletal vesicles, is shown: Actin, His-tagged VCA, Arp2/3 complex, CP and profilin were encapsulated inside of GUVs. They contained 10% Ni-NTA lipids and 2.5% PEG 2000 PE to avoid unspecific protein-membrane interactions. b) Confocal images of the equatorial plane of the cytoskeletal vesicles are shown. The encapsulation of only 3 µM actin (red hot) resulted in pronounced bulk polymerization (left side). Addition of 0.3 µM Arp2/3, 0.3 µM His-tagged VCA and 13.5 µM profilin to the solution prior to encapsulation induced localized actin polymerization at the membrane (right side). All scale bars are 20 µm.

elongation to the membrane. Profilin binds to actin monomers and prevents spontaneous polymerization inside the GUVS. Indeed, membrane localized actin polymerization was observed, but still a volume spanning network was formed (Figure 4.1 b). Pyrene Assays confirmed that the amount of VCA and Arp2/3 was sufficient to induce polymerization instantaneously despite the presence of profilin (Figure 4.2 a).

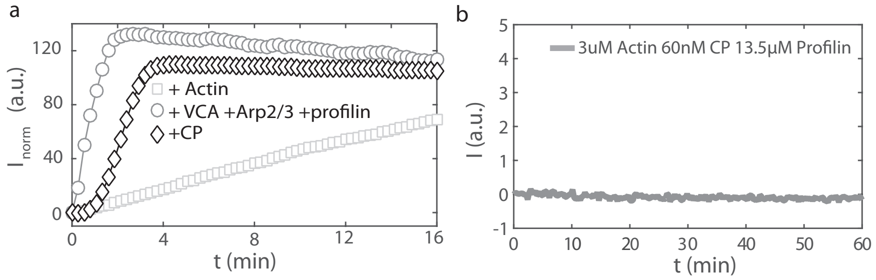

Figure 4.2: a) Pyrene fluorescence assays of actin polymerization in the dependence of actin binding proteins (ABPs): The polymerization rate of 3 µM actin (squares) was increased upon addition of 0.3 µM VCA, 0.3 µM Arp2/3 complex and 13.5 µM profilin (circles). Further addition of 0.02 µM CP (diamonds) resulted in a distinct lag phase before polymerization was initiated. The polymerization curves were normalized by the average of the last 10 measurement point. b) Actin polymerization was completely suppressed for at least one hour when 60 nM CP and 13.5 µM Profilin were added to 3 µM actin monomers. The offset at polymerization start was subtracted from the measurement curve.

4.2 MEMBRANE LOCALIZED NETWORK FORMATION IS CONTROLLED BY CP

CP binds to actin filament ends and inhibits monomer addition. In cooperation with profilin, it suppresses spontaneous nucleation and elongation of filaments in solution, which can be seen in actin-pyrene fluorescence measurements (Figure 4.2 b). the measurements of pyrene fluorescence of the full system (actin, Arp2/3, VCA, profilin and CP) in the presence of 20 nM CP indicated a distinct lag phase of 1.5 ± 0.3 min in the polymerization curve (Figure 4.2 a). This lag phase should ensure that the Arp2/3 complex can freely diffuse to the membrane before its activation as polymerization of actin is effectively suppressed. Indeed, encapsulation of the full system resulted in a complete localization of the actin network to the membrane for 78% of the vesicles (Figure 4.3). The remaining 22% still presented a volume spanning actin network. Two different morphologies were observed when the network localized to the membrane. Actin polymerized homogeneously in 42% and spatially separated in 36% of the vesicles. This indicates that already small fluctuations of CP protein are sufficient to vary nucleation rates for localized polymerization and different network morphologies appear.

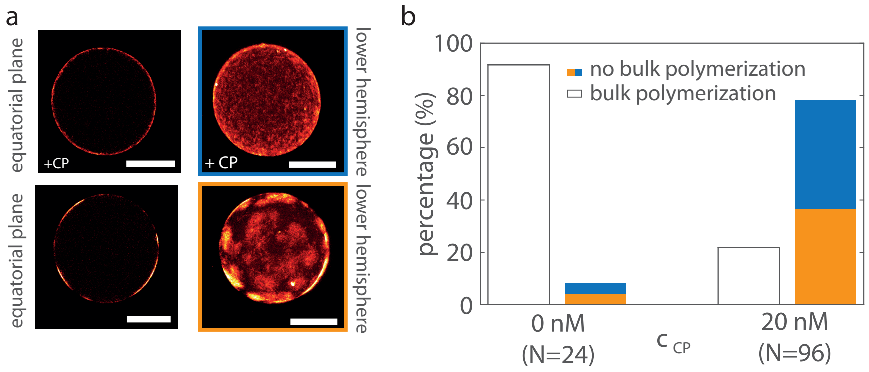

Figure 4.3: a) The equatorial plane and lower hemisphere of vesicles, which contained 3 µM actin, 300 nM Arp2/3, 300 nM VCA, 13.5 µM profilin and 20 nM CP, are shown. Two different network morphologies can be differentiated. Homogeneous actin polymerization is shown on the top and heterogeneous polymerization on the bottom. b) The histogram shows that CP shifts actin polymerization to the membrane. The right bar for each CP concentration is split in two subgroups: homogeneous polymerization (blue) and heterogeneous domain formation (orange). Scale bars are 20 µm.

An increase of CP led to the formation of three distinct domain morphologies of actin, which could be distinguished based on their curvature: (i) Convex actin protrusions (protrusion) with a length of up to 4 µm (Figure 4.4 a). These were able to push forward the vesicle's membrane and induced a convex deformation of the membrane (Figure 4.5 a). (ii) Concavely bent actin domains (concave domain), which induced a localized negative curvature into the vesicle's membrane (Figure 4.4 b and Figure 4.5 b) and (iii) flat actin domains, which had no discernible change of membrane curvature (Figure 4.4 c).

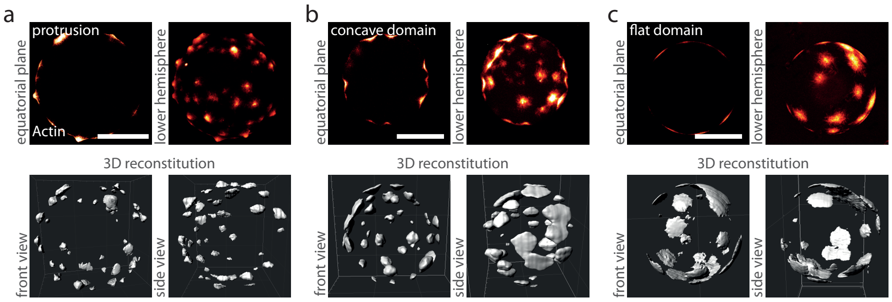
a
protrusion
Actin
equatorial plane
lower hemisphere
b
concave domain
equatorial plane
lower hemisphere
c
flat domain
equatorial plane
lower hemisphere
3D reconstitution
3D reconstitution
3D reconstitution
front view
side view
front view
side view
front view
side view

Figure 4.4: CP controlled actin polymerization led to three distinct membrane localized domain morphologies. On the top, confocal images of the equatorial plane and the lower hemisphere are shown. On the bottom, the front and side view of a computer 3D reconstruction from the confocal data are shown. a) Actin protrusions are presented. Their actin density was high and their lateral growth spatially confined. b) The formation of concave domains is shown. The lateral growth is more extended and the domains are bent inwards. c) Flat actin domains can be observed. Their lateral growth is more extended and flat. This type of morphology adapted to the membrane's curvature and induced no shape deformation of the membrane. All scale bars are 20 µm.

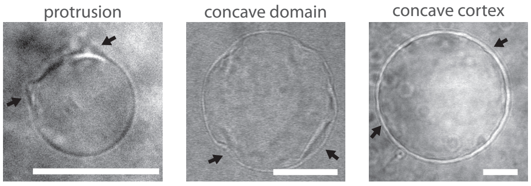
protrusion
concave domain
concave cortex

Figure 4.5: Bright-field images of the membrane are shown. On the left side, actin protrusion formed and pushed the membrane forward. In the center, shape deformations of the membrane induced by concave domains are shown. On the right, a negative bending of the membrane is induced due to the polymerization of a closed cortex formed by the overlap of many small concave domains. All scale bars are 20 µm.

The appearance and distribution of the different morphologies correlated to the concentration of CP (Figure 4.6 a). Protrusions appeared nearly exclusively at 40 nM CP, whereas formation of concave domains was more conserved and could be observed from 40 nM to 120 nM CP (Figure 4.6 a). Flat domains appeared at all studied CP concentrations, but the frequency decreased with an increasing amount of CP. At low (20 nM CP) and high CP concentrations (120 and 180 nM) closed cortices formed rather than spatially separated domains. Yet, the morphology changed. At high CP, the cortices were formed from many small overlapping actin domains, whereas at low CP densely grown actin networks appeared at the membrane. 50% of the closed cortices induced a negative bending of the membrane at 120 nM CP (Figure 4.6 a). Bulk polymerization was completely suppressed at 40 nM CP and increased continuously with an increasing CP concentration. It should be noted that protrusion and concave domains were not observed at the same time in one vesicles. Their appearance was exclusive.

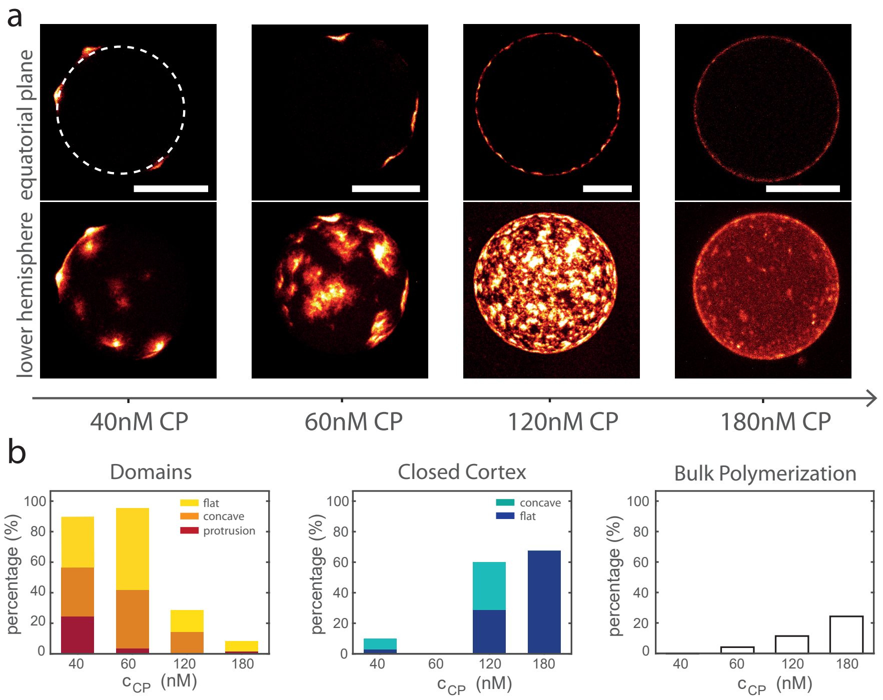

Figure 4.6: a) Confocal images of the equatorial plane and lower hemisphere of membrane localized actin polymerization are shown at different CP concentrations. b) The appearance and frequency of the different morphologies were dependent on the CP concentration. The distribution of the different morphologies is presented in three different histograms. The morphologies were split in three subgroups (domains, closed cortex and bulk polymerization). The histogram about domain formation was split in three sub classes (flat domains, concave domains and protrusion) and the closed cortex was sub-split into flat cortices and concave cortices. Histogram counts were N= 159, 218, 70, 74 at c(CP) = 40, 60, 120, 180 nM respectively. All scale bars are 20 µm.

4.3 DOMAIN NUCLEATION AND GROWTH IS CONTROLLED BY CP

In a next series of experiments, either VCA or Arp2/3 were labeled to identify if domain formation is driven by protein clustering of actin polymerization. VCA bound homogeneously to the membrane for several hours in the absence of any actin and Arp2/3 (Figure 4.7 a). Likewise, labeled Arp2/3 was homogeneously distributed, when it was coupled to the membrane via His-tagged VCA in the absence of any actin (Figure 4.7 b). But in the presence of actin polymerization VCA was no longer distributed homogeneously, instead it up-concentrated within the actin domains (Figure 4.7 c). Thus, domain formation results not from VCA or Arp2/3 clustering after binding to the membrane. Rather, domain formation was induced randomly and led to an up-concentration of VCA.

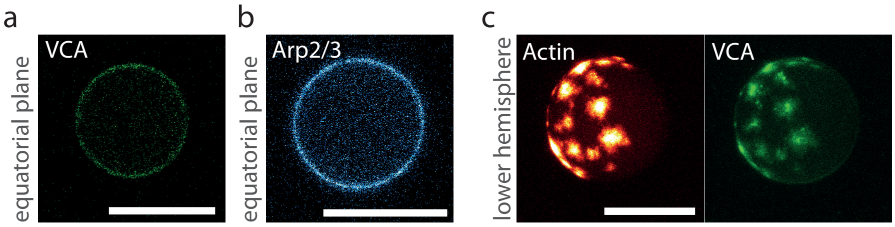

Figure 4.7: The actin binding proteins VCA and Arp2/3 were labeled to study their distribution at the membrane in the presence and absence of actin. a) The equatorial plane of a vesicle, which contained 0.3 µM VCA, is shown. 25% of the VCA were labeled with Atto 647N. b) 0.3 µM VCA and Arp2/3 were encapsulated. 35% of the Arp2/3 was labeled with Atto 647N. c) The actin channel is shown in red hot and the VCA channel in green. 3µM actin, 0.3µM VCA, 0.3µM Arp2/3, 60 nM CP and 13.5 µM profilin were encapsulated inside the GUV. 25% of VCA was labeled with Atto 647N and 10% of actin were labeled with Atto 488. All scale bars are 20 µm.

4.3.1 *Time resolved domain growth inside of vesicles*

Time dependent snapshots were taken at 40 and 120 nM CP every three minutes to study the temporal evolution of domain formation. At 40 nM CP, domain nucleation and formation was fast. Already one minute after production they could be observed at the membrane (Figure 4.8).

At 120 nM CP, domain nucleation was slower as no discernible domains could be observed after one minute (Figure 4.9). Domain formation was fully completed after 4 min at 40 nM CP and after 7 min at 120 nM CP. A negative bending of the membrane could be observed 7 min after production at both CP concentrations.

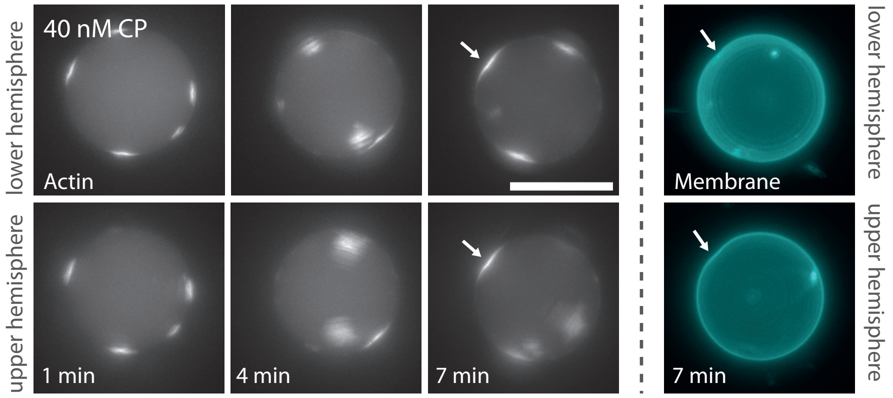
40 nM CP
lower hemisphere
upper hemisphere
Actin
1 min
4 min
7 min
Membrane
7 min
lower hemisphere
upper hemisphere

Figure 4.8: Fluorescence images of a vesicle at three different time points are shown. The actin channel is presented in grey scale and the membrane in cyan. Snapshots were taken every three minutes to minimize any artifacts induced by photo-oxidation. Vesicles were not fixed and therefore rotated during image acquisition. Scale bar is 20 µm.

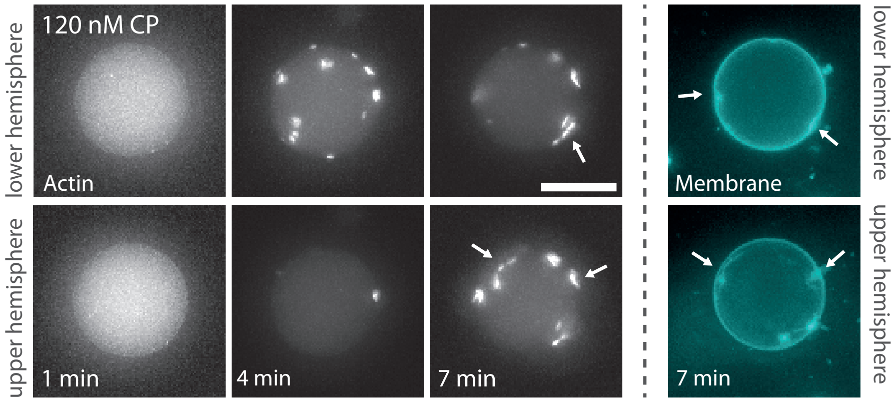
120 nM CP
lower hemisphere
upper hemisphere
Actin
1 min
4 min
7 min
Membrane
7 min
lower hemisphere
upper hemisphere

Figure 4.9: At three different time points fluorescent snapshots of vesicles are shown. 3 µM actin, 0.3 µM Arp2/3, 0.3 µM VCA, 120 nM CP and 13.5 µM profilin were encapsulated. The actin channel is grey and the membrane cyan. Scale bar is 20 µm.

Formation of actin protrusion was quick and only observed at 40 nM CP (Figure 4.10). A positive bending of the membrane was visible already one minute after production.

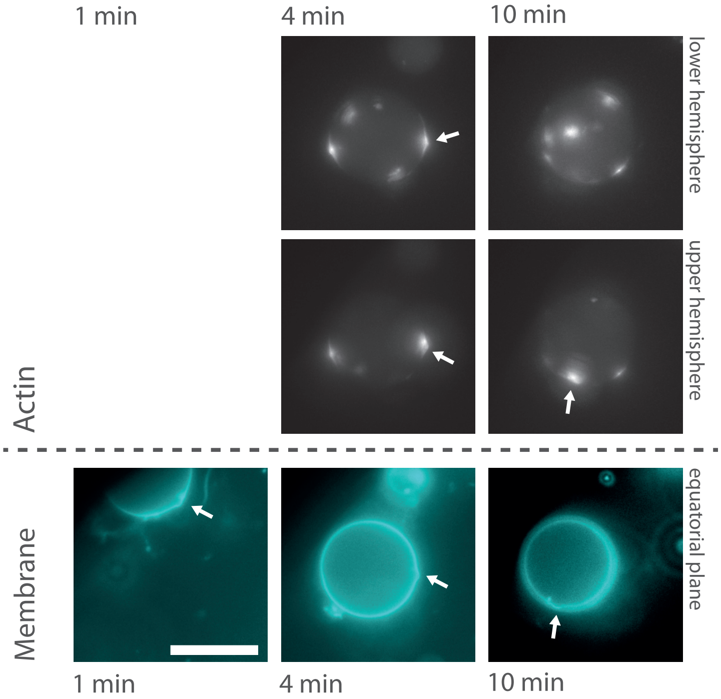

Figure 4.10: Temporal snapshot of protrusion formation at three different time points at 40 nM CP are shown. The membrane is shown is cyan and the actin channel in grey. Scale bar is 20 µm.

The snapshots show that domain nucleation occurs at multiple membrane sites and that all sites compete for the finite pool of actin, encapsulated inside the GUV. The monomers are already consumed before all nucleation sites grew together to form a closed cortex. Thus stable and spatially separated domains of different filament density emerged at the membrane. Also, a correlation between the number of domains and morphology type could be found (Figure 4.11). The domain number was lower in vesicles with protrusions ($\sim$ 15.5 per vesicles) compared to vesicles presenting concave domains ($\sim$ 31 per vesicles). The highest number of domains could be found in vesicles with only flat actin domains ($\sim$ 35 per vesicles).

4.3.2 *Time resolved domain growth on a supported lipid monolayer*

TIRF measurements of domain growth on a supported lipid monolayer were performed at different CP concentrations to better understand their growth behavior dependent on CP. The monolayer consisted of DOPC lipids, where 2.5% were replaced by PEG-PE-lipids and 10% by Ni-NTA lipids. They were incubated with His-tagged VCA and properly washed afterwards, to remove any VCA from the

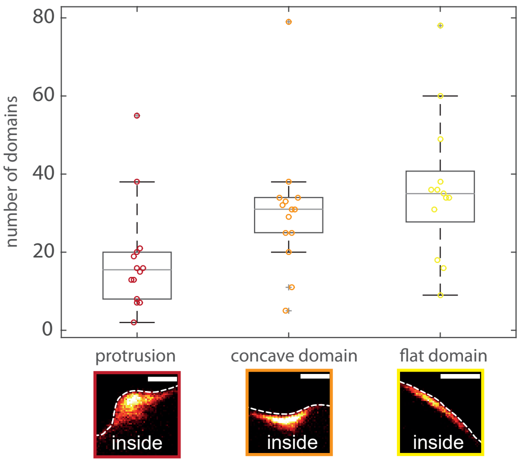

Figure 4.11: Boxplots of the domain number at the vesicle's membrane, dependent on the type of actin domain morphology, are shown. The median of the patch number per vesicle correlated with the observed domain shape. Medians were 15.5 for protrusions, 31 for concave domains and 35 for flat domains. Bottom panels illustrate the deformation types. The central grey line in the boxplots indicates the median. The bottom and top edges of the box mark the 25th and 75th percentiles, respectively. The whiskers go to the most extreme considered data point. Not considered data points are marked by a cross in the center of the data point. Scale bars are 3 µm.

bulk to ensure that Arp2/3 is only active at the surface. The measurements indicate that lateral domain growth was dependent on CP. In the absence of any CP, domains grew up to a size of about 15 µm after 6 min. As soon as CP was present domain growth was spatially confined. At 0.02 µM CP domain diameters grew to ~7 µm after 6 min. A further increase of CP to 0.04 µM CP formed domains with diameters about 5 µm and at a final increase to 0.12 µm CP created domains about 2 µm large (Figure 4.12 and Figure 4.13).

Thus, CP controlled lateral domain growth and size in a concentration dependent manner. Likewise nucleation behavior of actin domains was controlled by CP. In the absence of any CP ~16 domains could be counted on the monolayer after 6 min. Addition of 0.02 µM CP resulted in the formation of ~55 domains. A further increase to 0.06 µM led to the formation of ~65 domains and 112~ domains could be observed at 0.12 µM CP. These observations were consistent with measurements from pyrene assays. Here the polymerization kinetics of actin in the presence of Arp2/3, VCA and profilin were measured at different CP concentrations. The time, before polymerization was initiated, increased and polymerization speed decreased with an increasing CP concentration (Figure 4.14).

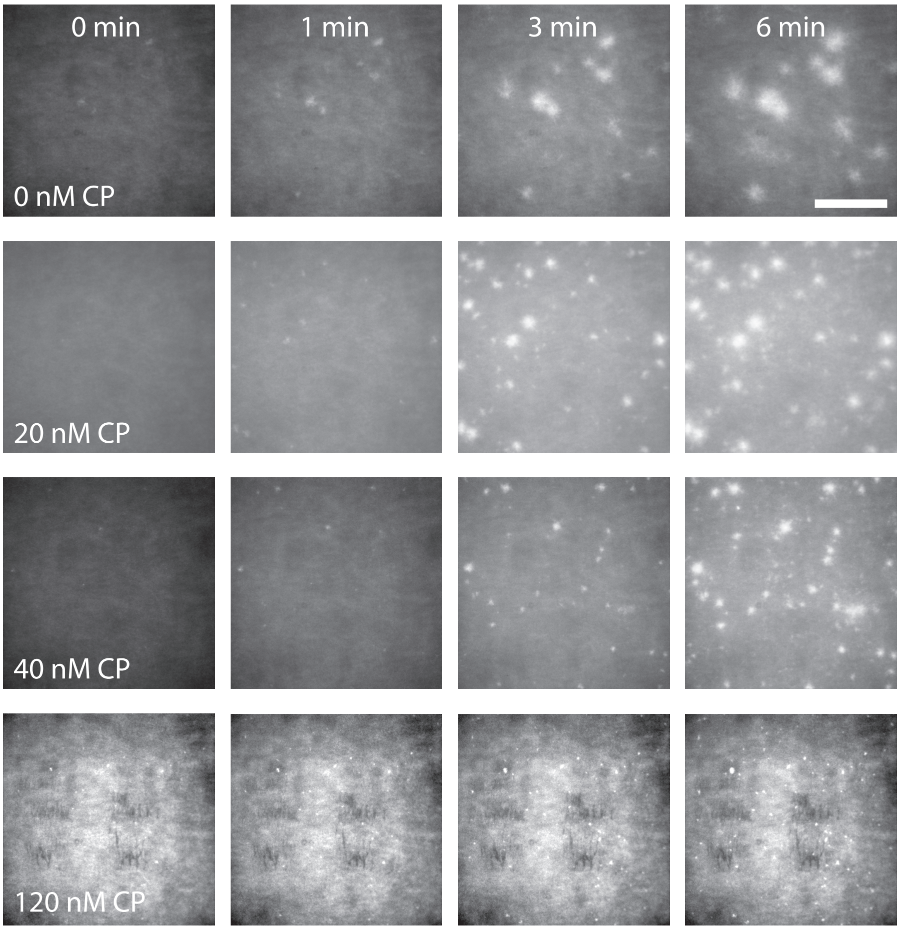

Figure 4.12: TIRF snapshots of domain growth on a supported lipid bilayer incubated with His-Tagged VCA are shown at different CP concentrations. The membranes were incubated with 300 nM HisTagged VCA and after washing 3 µM actin, 0.3 µM Arp2/3, 13.5 µM profilin and the desired amount of CP (0,0.02,0.04,0.12 µM) was added to the monolayer. 10% of actin were labeled with Atto 488. Scale bar is 20 µm.

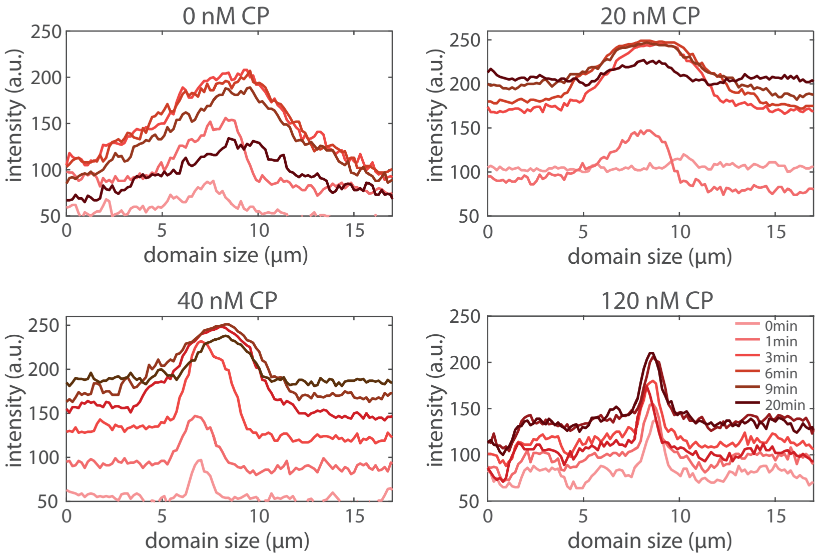

Figure 4.13: The intensity profile of a cut trough the domain center is shown over time. For each CP concentration one domain was measured. The spatial extension of the domains decreased with an increasing CP concentration.

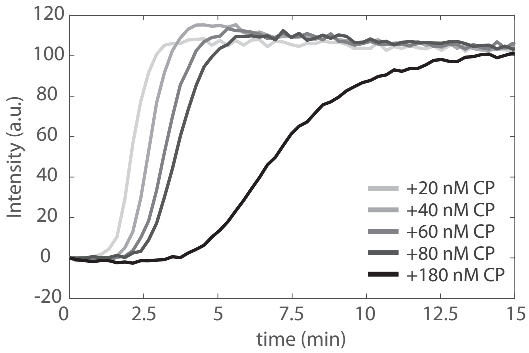

Figure 4.14: Polymerization kinetics of branched network formation at different CP concentrations were measured over time. 3 µM actin, 0.3 µM Arp2/3, 0.3 µM VCA, 13.5 µM profilin and the desired amount of actin were mixed together. 20 % of actin were labeled with pyrene.

4.4 CONTRACTILE BEHAVIOR OF NMM II IS MOST EFFICIENT AT HIGH CP CONCENTRATIONS

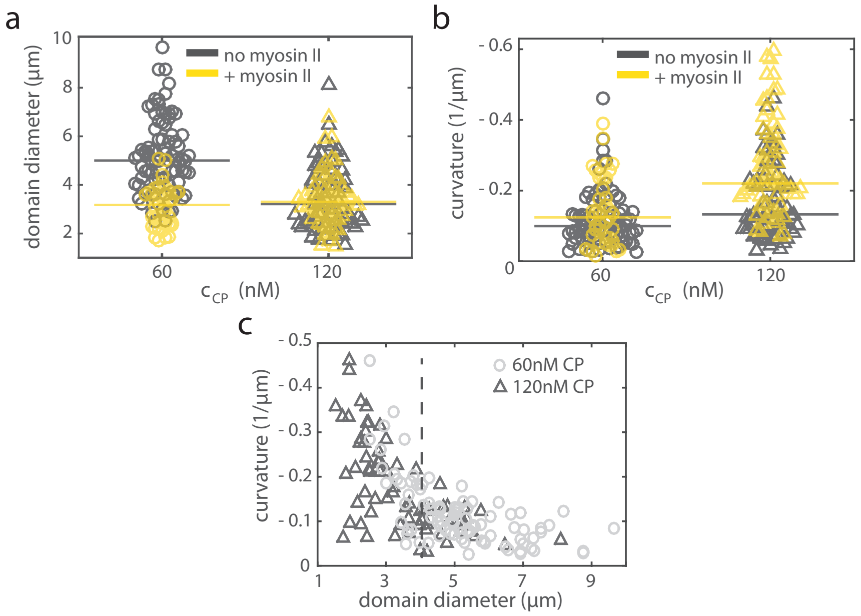

Figure 4.15: Domain diameter and curvature of spatially separated negatively bent domains were measured in the absence or presence of non-muscle myosin II at two CP concentrations. a) Measurements of the median domain diameter are shown. It decreased from 5.2 μm at 60 nM CP (grey circles) to 3.4 μm at 120 nM CP (grey triangles). Upon addition of 5 μm NMMII to the solution prior to encapsulation, the domain diameter contracted to 3.2 μm at 60 nM CP (yellow circles) and remained constant at 120 nM CP (yellow triangles). b) Analysis of the median curvature are shown. The curvature increased from 0.1 μm^{-1} at 60 nM CP (grey) to 0.13 μm^{-1} at 120 nM CP (grey). The addition of 5 μM NMMII increased the curvature to 0.12 μm^{-1} at 60 nM CP (yellow) and to 0.22 μm^{-1} at 120 nM CP (yellow). c) Scatter plots of the domain curvature vs. the domain length show that the domain diameter directly correlated to domain curvature. Only small domains ($< 4 \mu m$) had curvatures up to 0.46 μm^{-1}

The domain size and curvature was evaluated for different CP concentrations to investigate the dependence of the mechanical interplay between the actin domains and the membrane dependent on CP concentration. With an increase from 60 to 120 nM CP the median domain diameter decreased from 5.2 µm to 3.4 µm and the curvature increased from 0.1 to 0.13 1/µm (Figure 4.15 a, b). Thus there was a direct correlation between domain length and curvature, which could be also confirmed by scatter plot of the median diameter versus the curvature. Only at diameters below 3.5 µm, domain curvatures up to 0.5 1/µm could be observed (Figure 4.15 c). The presence of CP therefore led to more compact domain formation, which had a positive feedback on the curvature.

Addition of NMMII prior to encapsulation allowed to study contractile acto-myosin behavior and domain adhesion to the membrane dependent on CP concentration. At 20 nM CP large acto-myosin clusters formed at the membrane and were pulled away (Figure 4.16). At 60 nM CP, the network remained tightly connected to the membrane in the presence of NMMII and different phenotypes of membrane deformations were observed (Figure 4.16). In about 25% of the vesicles only inward bending could be observed with a similar curvature compared to the absence of NMMII (Figure 4.17). Only the domain diameter decreased significantly from 5.2 to 3.2 µm (Figure 4.15). About 15 % did not show any deformation at all. In more than 50% a complete new phenotype occurred. Membrane invaginations, still in contact with the acto-myosin gel, could be observed. About 2-3% of them fissioned from the membrane. At 120 nM CP, domain diameter remained constant, but the curvature clearly increased to 0.22 1/µm (Figure 4.15). The increase of curvature correlated to an increased appearance of vesicles presenting membrane invaginations. They were present in more than 80% of the vesicles (Figure 4.17). Thereby 30% of those vesicles showed fissioned invaginations (Figure 4.16). Thus efficient network adhesion required a minimum concentration of 60 nM CP. Contraction of the membrane attached domains towards the vesicle's bulk and thus invagination formation or fission was clearly promoted at high CP concentration.

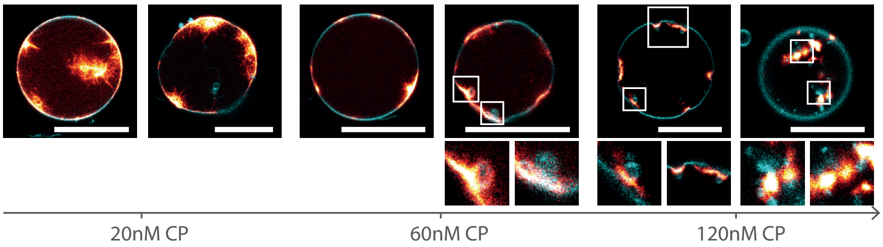

Figure 4.16: Confocal images of the equatorial vesicle's plane show the interactions of the actin network (red hot) with the membrane (cyan) in the presence of 5 μM NMMII at different CP concentrations. At 20 nM CP, the network detached from the membrane and was pulled towards the bulk of the vesicle. At 60 nM CP, membrane invaginations (insets) emerged at the membrane. At 120 nM CP, membrane invaginations (left inset) and fission events (right insets) could be observed. Scale bars are 20 μm.

4.5 STRUCTURE OF ACTIN DOMAINS DEPENDS ON CP

Membrane localized network growth was modeled by a set of consecutive elementary reaction equations using finite element analysis in COMSOL Multiphysics 5.3 (COMSOL Inc.) to better understand its

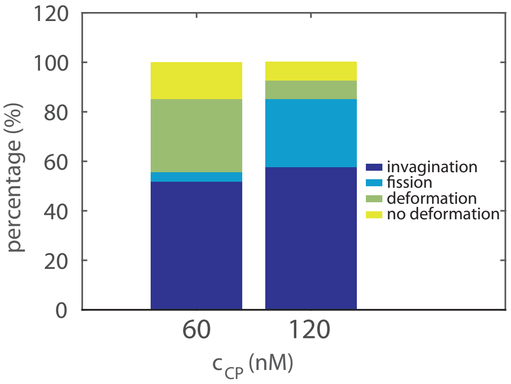

Figure 4.17: The quantification of the contractile response of non-muscle myosin II is shown. It was dependent on the concentration of CP. 3 μM actin, 0.3 μM VCA, 0.3 μM Arp2/3 complex, 13.5 μM profilin and 5 μM NMMII were encapsulated inside of vesicles in the presence either of 60 nM CP or 120 nM CP. This resulted not only in the formation of local membrane deformations but also in the formation of membrane invaginations, which (navy) were visible in more than 50% of the vesicles at both CP concentrations. However, fission events (detached membrane invaginations, blue) occurred preferably at 120 nM CP. The histogram counts CP were 27 at 60 nM and 40 vesicles at 120 nM CP. At least two independent experiments per CP concentration were performed.

dependence on CP concentration. All simulations were performed in close collaboration with F.C. Keber [73]. The final goal was to model network growth against a resistant membrane by simulating the density of barbed end filaments with time. The final membrane protrusion velocity and thus the resulting shape deformations was dependent on the barbed end density. The time dependence reflects the vertical network growth. For the modeling, we followed already published models for lamellipodial growth [98, 150], which were adapted to our studied system. In the first section the implementation of the model is shown, whereas the second section discusses the results.

4.5.1 *Implementation of the model*

Network growth and chemical composition are determined by the two antagonistic key players Arp2/3 and CP. The Arp2/3 complex must be activated by G-actin bound VCA (VCA*), which is localized to the membrane and needs to bind an actin monomer prior to activation (Figure 4.18). The activated Arp2/3 (Arp2/3*) induces the nucleation of new filaments by branching from an existing filament end. CP terminates barbed end elongation, which results in shorter filaments and less branching possibilities. The elongation and branching rates are set by the available monomer pool and the availability

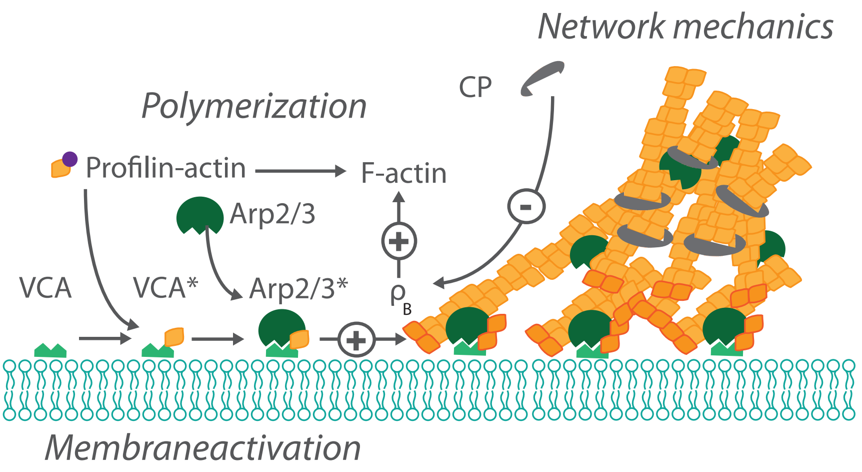

Figure 4.18: Schematic of membrane localized actin assembly kinetics: A finite reservoir of membrane activated Arp2/3 complex nucleates a branched network at the membrane. After polymerization start, the concentration of available Arp2/3 complex decreases and equilibrate towards a new steady state concentration, as the regeneration rate is slow. The balance between branching by Arp2/3 complex and capping by CP determines the final network mechanics, leading to the observed shape deformations of the membrane.

of Arp2/3*. As all monomeric actin is incorporated into the network at the membrane, we computed the network growth as the density of barbed ends with time. Time dependence reflects the vertical network growth.The following kinetic equations describe the full polymerization system as introduced by [73].

$$Nucleation : G + G \rightleftharpoons G_2; G_2 + G \rightleftharpoons G_3 := F_3 \tag{4.1}$$

$$Polymerization : F_n + G \underset{\mathrm{k_{off}}}{\overset{\mathrm{k_{on}}}{\rightleftharpoons}} F_{n+1} \tag{4.2}$$

$$VCA - Activation : VCA + G \underset{k_2}{\overset{k_1}{\rightleftharpoons}} VCA* \tag{4.3}$$

$$Arp2/3 - Activation : VCA^* + Arp2/3 \underset{k_4}{\overset{k_3}{\rightleftharpoons}} Arp2/3^* \tag{4.4}$$

$$Branching : Arp2/3^* + F_n \xrightarrow{\mathrm{k_{Arp}}} F_n + F_1 + VCA \tag{4.5}$$

$$Capping : CP + F_n \xrightarrow{\mathrm{k_{Cap}}} CPF_n \tag{4.6}$$

With the notation $G/G_2/G_3$ for actin monomer/dimer/trimer concentration, F_n for an actin filament with n subunits, VCA for the Arp2/3 activating region of WASP family proteins, VCA* for the complex of VCA and an actin monomer, $Arp2/3^*$ for Arp2/3 complex activated with VCA*, CP for Capping Protein, CPF_n for a n subunits long filament capped by CP and k_i for the respective rates. Starting from

these kinetic equation we developed a set of consecutive differential equations to model the barbed end density (B) over time.
We implemented a paused state of VCA to the equations to account for the local up-concentration of VCA, since it was observed in the experiments. In this paused state VCA (V^+) is immobile and not available for new Arp2/3 activation. The paused state was only implemented for the simulations at finite protein pools to ensure that the reaction kinetics do not rely on the introduction of V^+. The system was split in a membrane bound fraction (VCA, VCA*, Arp2/3*, B,V^+) simulated with 2D diffusion and a cytosol fraction (G-actin, CP, Arp) modeled by 3D diffusion. At first the simulations were performed at infinite protein pools and then at finite protein pools to show that our results do not rely on protein depletion. For simulations at infinite protein pools a cylindrical geometry was used (r=7 µm, h=9 µm). The cytosol concentrations of G-actin, Arp2/3 and CP at the cylinder site, opposing the membrane, obeyed fixed Dirichlet boundary conditions to keep their initial concentration fixed.
For simulations at finite protein pools we chose a cone shaped geometry, where the circular disc describes the actin domain at the membrane and the cone tip the center of the vesicle. The dimensions of the cone were estimated from experimental data. The height was the vesicle's radius (h=18 μm) and the radius of the circular disk was half the center-to-center distance between two domains. According to the experiments, domain distance depended on the CP concentration. For 40 nM CP, 16 domains were observed in average and from that we calculated a center-center distance of 10 μm. At 80 nM CP, 35 domains were observed in average and the distance decreased to 6 μm. At 120 nM CP, a distance of 1.7 μm was directly measured from the images. A Neumann zero flux condition was set at the surface boundary.
The membrane bound protein concentration and reaction kinetics are described by the following differential equations introduced by [73].

$$\frac{\partial V}{\partial t} = D_{\mathrm{V}}\nabla_m^2 V - k_1 G|_0 V + k_2 V^* + k_{re} V^+ \tag{4.7}$$

$$\frac{\partial V^*}{\partial t} = D_{V^*}\nabla_m^2 V^* + k_1 G|_0 V - k_2 V^* - k_3 Arp|_0 V^* + k_4 Arp^* \tag{4.8}$$

$$\frac{\partial Arp^*}{\partial t} = D_{\mathrm{Arp}}\nabla_m^2 Arp^* + k_3 Arp|_0 V^* - k_4 Arp^* - k_{Arp} Arp^* B \tag{4.9}$$

$$\frac{\partial B}{\partial t} = D_{\mathrm{B}} G|_0/G_{int}\nabla_m^2 B + k_{Arp} Arp^* B - k_{Cap} CP|_0 B - k_{Deg} B \tag{4.10}$$

$$\frac{\partial V^+}{\partial t} = k_{Arp} Arp^* B - k_{re} V^+ \tag{4.11}$$

Thereby B denotes the density of actin filaments pushing against the membrane, $|_0$ denotes the concentration of cytosolic species at the membrane and ∇_m^2 denotes the diffusion operator at the membrane. All membrane restricted reactions require a continuous flux of proteins from the cytosol.

$$\frac{\partial G}{\partial t} = D_{\mathrm{G}} \nabla^2 G \tag{4.12}$$

$$\frac{\partial Arp}{\partial t} = D_{\mathrm{Arp}} \nabla^2 Arp \tag{4.13}$$

$$\frac{\partial CP}{\partial t} = D_{\mathrm{CP}} \nabla^2 CP \tag{4.14}$$

The cytosolic concentration are not modeled directly. But appear as boundary conditions.

$$-D_G \partial_z G|_{z=0} = -k_1 G|_0 V - k_{on} G|_0 B + k_{off} B \tag{4.15}$$

$$-D_{Arp} \partial_z Arp|_{z=0} = -k_3 Arp|_0 V^* \tag{4.16}$$

$$-D_{CP} \partial_z CP|_{z=0} = -k_{Cap} CP|_0 B \tag{4.17}$$

where ∂z...$|_{z=0}$ denotes the derivative normal and evaluated at the membrane (z=0). The kinetic rates were all taken from literature besides k_{Arp} and k_{re}: $k_{on} = 11.6/\mu M/s, k_{off} = 1.4/s$ from [117]; $k_1 = 43/\mu M/s, k_2 = 30/s, k_3 = 0.8/\mu M/s$ and $k_4 = 0.6/s$ from [91]; $k_{Cap} = 4/\mu M/s$ from [128]. k_3 was reduced by a factor of 3 to better fit our experimental results. The interaction parameter for branching was set to $k_{Arp} = 0.02 \mu m^2/s$ to enable steady network growth. k_{re} was set to 0.001/s to fit the experimental finding of an approximately 4-fold higher VCA concentration compared to outside the domain. The diffusion constant for actin was taken from literature $D_G = 30 \mu m^2/s$ [81]. The diffusion constant for VCA was determined experimentally by FRAP measurements $D_V = 1.59 \mu m^2/s$. The remaining diffusion constants were estimated by the Stokes-Einstein relation with the assumption that all proteins are globular, ($D_{CP} = 26 \mu m^2/s, D_{Arp} = 17 \mu m^2/s, D_V = 0.96 \mu m^2/s, D_A = 0.84 \mu m^2/s$). The initial values of the protein concentrations were set according to the experimental conditions [39]. Spatial spreading of the network along the membrane was treated as diffusive 2D random walk with the diffusion constant D_B and scaled by the local polymerization speed in a time dependent 2D simulation. $D_B = 0.0077 \mu^2/s$ was chosen according to experimental observations. Also a degradation term $k_{Deg} \cdot B$ for the barbed end density was included to account for the filaments, which are already too far from the membrane to be accessible for branching. A small rate was chosen for k_{Deg}=0.001 /s, which is equivalent to the presence of 1 nM CP, so that it only becomes relevant when the local CP concentration is depleted.

4.5.2 *Theoretical discussion*

At start of the simulation all VCA was bound to the membrane in the inactive state, and all other proteins were monomeric, inactive and in the cytosol. The VCA-actin complex formation and subsequent activation of Arp2/3 was almost instantaneous, while the nucleation of first actin filaments was delayed. These filaments were necessary to initiate network growth (seeding) and once they were formed, a rapid increase in the density of barbed ends was observed due to frequent branching events (initial growth) (Figure 4.19). As the pool of available Arp2/3* was finite and capping antagonized branching, the growth rates of barbed ends decreased (transient phase) and barbed end density finally reached a steady state. The growth processes towards the steady state were controlled by CP.

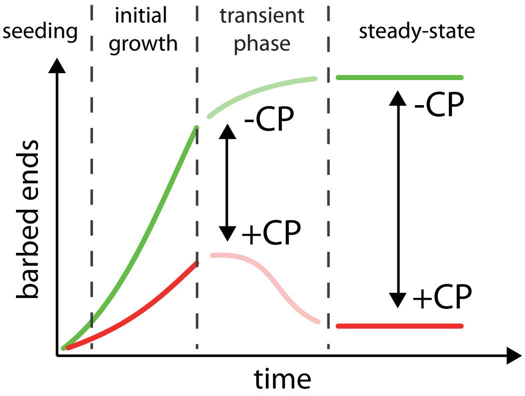

Figure 4.19: Network growth can be observed by modeling the temporal evolution of barbed ends. Four different growth regimes occured. The seeding phase, where first barbed ends were formed, was followed by an initial rapid growth. Finally, the barbed ends leveled off to a steady state by passing a transient phase. The growth processes depended on the concentration of CP.

At first we discuss the case of a distant infinite reservoir of proteins, which diffused towards the membrane so that concentration gradients could occur. At simulation start, the system was far from equilibrium. The initial growth phase was dominated by branching events followed by a delayed response of CP (Figure 4.20 d), which controlled the number of capping events and thus the final steady state concentration. The steady-state barbed end density decreased with an increasing CP concentration (Figure 4.20 a, b). In contrast the steady state concentration of available $Arp2/3^*$ increased with an increase of CP, since less barbed ends for the branching reaction were accessible, which in turn resulted in a lower branching rate (Figure 4.20 c). The growth rate of the network, which was proportional to the barbed end density also changed dependent on CP and decreased with an increasing concentration of CP. This is consistent with observations from pyrene assays. Two distinct growth regimes emerged dependent on CP: At low CP (40 nM), the barbed end density leveled off to a high steady-state concentration after passing a slightly higher peak intensity. The transient peak resulted from the balance between branching and capping events. At high CP concentrations (80 nM, 120 nM), the maximal barbed end density was lower compared to low CP. But likewise, the steady-state concentration was much lower and thus a more distinct peak could be observed before the barbed end density leveled off to the final steady-state concentration.

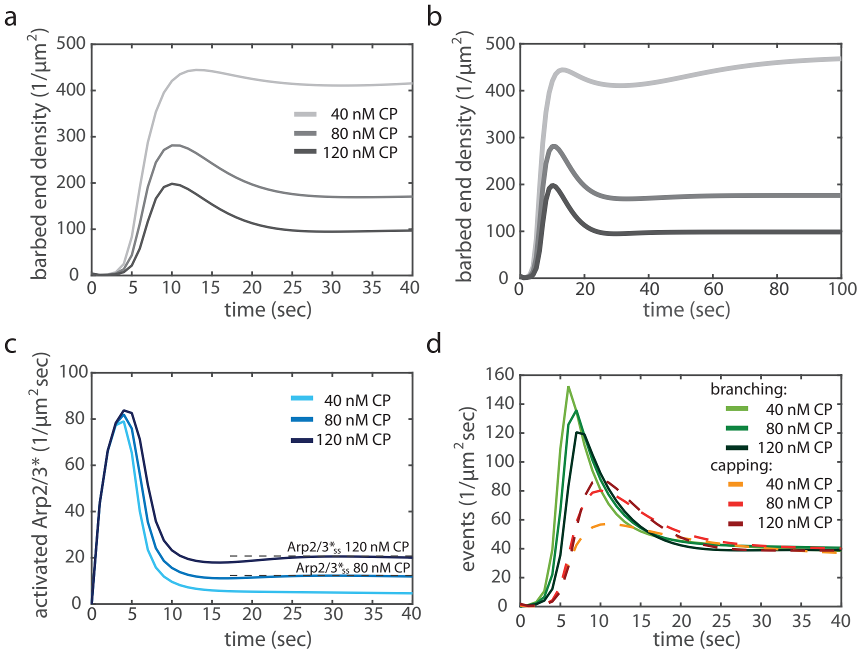

Figure 4.20: a,b) The temporal evolution of barbed end density was modeled on the top left side for 40 sec and on the right side for 100 sec. c) The temporal evolution of activated Arp2/3 complex (Arp2/3*) is shown. d) Branching and capping events at infinite protein pools were plotted over time. The final steady state of barbed end density and Arp2/3* was set by CP concentration. The balance between branching and capping events controlled the equilibration process of network growth towards the steady state.

The next step was to perform the simulation at finite protein pools to model the effects of local actin monomer depletion on the polymerization kinetics. The protein depletion was comparable to continuously changing starting conditions. At higher CP concentration more domains appeared at the membrane. As a consequence, the kinetic behavior also changed along the radial coordinate. The steady-state level decreased at all CP concentrations continuously with time.

At low CP concentration (40 nM), a rapid increase of barbed ends was observed, which decreased after passing a maximum intensity towards the steady state (Figure 4.21). As the starting conditions changed, the growth behavior along the radial coordinate also changed and the maximal reached filament intensity decreased with time. This resulted in a flat radial polymerization profile after 40 seconds (Figure 4.21). At 80 nM CP, a rapid increase of network density was observed leveling off to the steady state and in contrast to low CP a clear distinct peak appeared for all radial coordinates (Figure 4.21). Here monomer depletion seemed to affect the starting condition along the membrane much less as the barbed end density was much lower compared to 40 nM CP and the monomer pool was not depleted yet. This growth behavior resulted in a polymerization wave with its origin at the radial coordinate zero and then propagated along the membrane in both directions (Figure 4.21). In the domain center the density of pushing filaments was much lower compared to the rim of the polymerizing domain. At high CP concentration, the polymerization profile became flat again after 40 sec and was comparable to the one at 40 nM CP (Figure 4.21). This resulted from the smaller accessible protein pool per domain and demonstrated that also global conditions such as the number of nucleation sites control the overall growth conditions.

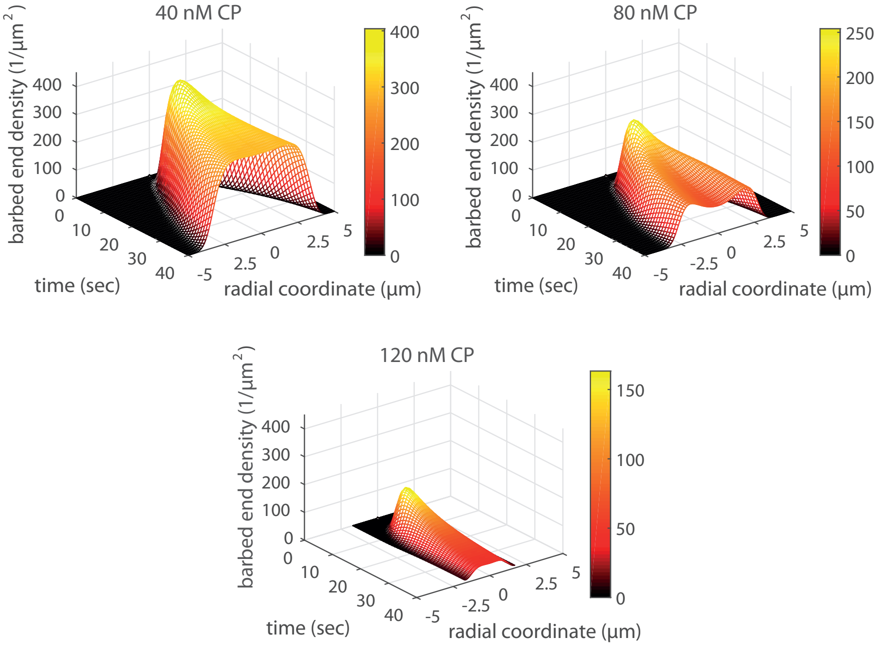

Figure 4.21: The spatio-temporal network growth was modeled along the membrane at finite protein pools. Two distinct barbed end patterns emerged. At 40 and 120 nM CP a flat barbed end distribution was observed and at 80 nM a double-peaked density distribution occurred.

The occurring polymerization patterns can be related to the observed shape deformations in our experiments, considering that the number of barbed ends, pushing against a tensed membrane, determine the local membrane protrusion velocity [98].

4.6 DISCUSSION

In this study it was shown that membrane localized actin polymerization is controlled by the presence of ABPs. Thereby, the focus was set on CP concentration. Network growth did not only depend on local CP variations, rather the interdependence between global growth conditions and local growth kinetics determined the final polymerization patterns pushing against the membrane. The polymerization pattern either induced a negative or positive bending of the membrane. At low CP concentration, a few domains nucleated rapidly at the membrane. These domains quickly grew together and the monomer pool was split up between them before new ones were nucleated due to fast lateral network growth. An increase of CP slowed down nucleation efficiency, but at the same time also network growth decreased and the monomer pool depleted slower. Many small confined actin domains emerged at the membrane over time. They could grow that dense that a closed cortex was formed out of many small domains. At the highest studied CP concentration, filament capping was too efficient and membrane localized polymerization less favored. A volume spanning network could be observed. TIRF measurement of the domain growth on a lipid monolayer confirmed that nucleation efficiency and lateral domain growth was controlled by CP. Confocal imaging of VCA distribution at the membrane revealed a local up-concentration, that is consistent with already published data [57, 83]. The kinetic model of membrane localized polymerization kinetics allowed to correlate the occurring shape deformations to the two distinct non-uniform polymerization patterns resulting in an inhomogeneous barbed end distribution. These density patterns could be directly correlated to an inhomogeneous membrane protrusion [98]. The number of barbed ends pushing against the membrane was low in our experiments ($<= 450/\mu m^2$) and thus the protrusion velocity directly correlated to barbed end density, when working against membrane tension. Moreover the number of filaments was too slow to be affected by local monomer depletion [2]. At low CP, the polymerization profile was flat and therefore the membrane protruded forward with a constant velocity to form a membrane spike. In contrast, at increased levels of CP filament density increased towards the domain rim and protrusion velocity was higher at the domain edge compared to the domain center. As a consequence, a concavely bent actin domain was formed. All simulations were performed in the absence of any external force and thus the protrusion velocity could not be modeled directly. Therefore it remains an open challenge to combine the kinetic simulations with the mechanical feedback of the membrane. The theoretical model, on which all performed simulations are based, is the Brownian Ratchet mechanism [95]. But over the past years an elastic continuum model was developed to account for internal stresses induced by continuous polymerization and related them to actin based motility [54]. But so far the model was not used to simulate lamellipodial growth or different actin induced shape deformations of the membrane. Thus it would be a major achievement to link such an elastic model to the here observed shape deformations. Stress gradients induced by the barbed end density gradients could either induce an inwards or outwards bending dependent on the gradient's orientation as soon as the growth stresses are released [54, 116].

The biological relevance of CP as key regulator was also investigated in the frame of this study. CP overexpression experiments were performed by Prof. Dr. Jan Faix. The overexpression resulted in an increased number of actin containing intracellular vesicles [39]. This corroborates the view that elevated CP concentrations promote the formation of concavely shaped deformations. Moreover the lamellipodium thickness clearly decreased and filopodia formation was completely suppressed, as the presence of CP promotes filament branching rather than elongation [6]. The experiments were consistent with CP depletion experiments in B16F1 mouse melanoma cells. In the absence of CP no lamellipodium formed at all, but an explosive increase of filopodia could be observed, as elongation is favored in the absence of CP [94]. The strong interdependence of the network structures might result from a homeostasis effect of the different actin cytoskeleton structures in cells, as first demonstrated to be an important mechanism in fission yeast [27, 144]. Similar to our experiments the limited actin monomer pool is split between the different actin structures, depending on the activation of the nucleation factors Arp2/3 complex and formin.

Our experiments also demonstrated that actin polymerization alone was not sufficient to induce membrane fission and to form endocytic-like vesicles. Only in the presence of molecular motors, fission events were observed. Again the contractile response correlated to the CP concentration. The requirement of myosins is in accordance with observations in vivo [29, 33, 88, 146]. Further studies are needed to shed light on the dynamics and physical mechanisms behind membrane fission events.

To sum up, the experiments showed that growth kinetics of the membrane bound actin network are decisive for the mechanical interplay with the membrane. Growth kinetics are controlled by CP in a concentration dependent manner. However, other ABPs like formin or VASP should have huge impact on network growth rate and its organization. But to fully understand how microscopic assembly kinetics, controlled by ABPs, are linked to the mesoscopic membrane deformation, a continuum elastic model is required to link density gradients to stress gradients. Also, the regulation of the ABPs remains an interesting field so study. In cells regulatory proteins like CARMIL, V-1 or Arpin exist to control the activity of CP and Arp2/3 [38, 40, 51, 72]. Their presence could be decisive for cells to switch between the diverging demands of function. In the here presented experiments it was the balance between branching and capping events that finally determined growth kinetics and the resulting shape deformations. Under confinement the conditions for branching and capping change continuously and thus the experiments demonstrate the urgent need to understand the full growth kinetics of the network even beyond the steady-state.

5

IN-VITRO RECONSTITUTION OF FILOPODIA FORMATION MEDIATED BY VASP

In this in-vitro study the focus was set on exploring the role of VASP during filopodia formation in a fully reconstituted vesicle system. To this end we couple His-Tagged VASP to the lipid membrane inside of vesicles in the absence and presence of additional ABPs. To ensure high activity of VASP, human VASP was used. But, the GAB domain was exchanged by dicty GAB (hVASP dGAB), as elongation efficiency is high even at low actin concentrations [25]. Only a sufficient localization to the membrane either by the presence of depletion forces or by the inhibition of spontaneous actin polymerization inside the vesicle due to the presence of CP and profilin resulted in the formation of actin filopodia pushing the membrane forward. Addition of fascin induced a star-like rearrangement of the membrane localized network, which was stiff enough to induce not only actin protrusion but also large-area deformations.

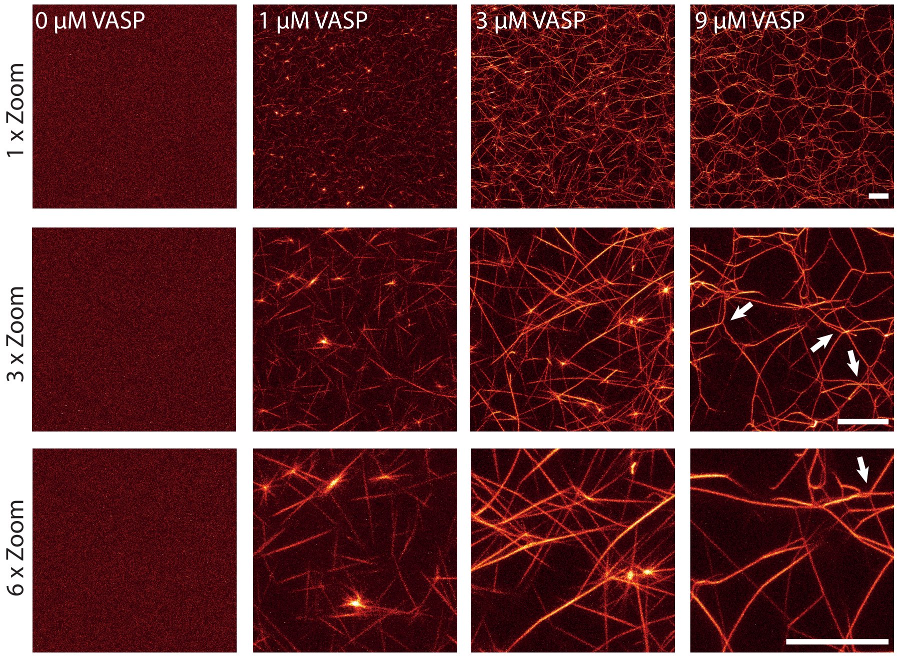

Figure 5.1: Confocal z-projections of alexa488-phalloidin labeled actin networks at different VASP concentrations are shown. In the presence of VASP actin bundles were observable. At a high VASP concentration (9 µM) the actin filaments began to crosslink and formed an interconnected network. All scale bars are 20 µm.

5.1 VASP PROMOTES THE FORMATION OF FILOPODIA LIKE ACTIN BUNDLES

First, we tested the molecular assembly properties of hVASP dGAB, which is called VASP from now on, in fluorescent network bulk assay. We polymerized actin networks (3 µM actin) at different VASP concentrations. In the absence of VASP only a diffusive actin signal could be observed and no network structures were present (Figure 5.1). The addition of 1 µM VASP induced the formation of short actin bundles, which were clearly discernible from the background. At 3 µM VASP, the actin bundles became longer and more distinct at highest used VASP concentration, a crosslinked network was formed from the bundles. The observed networks bundles resemble to the network architecture of filopodia in cells as filopodia are formed from stiff parallel aligned actin bundles. Therefore, VASP is an excellent candidate to study filopodia formation in a fully reconstituted system.

5.2 FILOPODIA-LIKE NETWORK FORMATION LOCALIZED TO THE MEMBRANE INSIDE OF GUVS

We used a modified version of cDICE to encapsulate VASP and actin monomers inside of GUVs of a radius of 10-25 µm. Thus to shift filament elongation towards the membrane, we recombinantly modified VASP and added an His-Tag to the N-Terminus. His-Tagged VASP is able to bind to lipid bilayers via NiNTA-lipids. 10 % NiNTA-lipids were incorporated in the vesicle's membrane. 2.5 % of PEG-PE lipids were also incorporated in the lipid bilayer in order to prevent any unspecific protein-membrane interactions.

The encapsulation of 1 µM His-tagged VASP and 3 µM actin induced actin polymerization inside the vesicle. Membrane localization was heterogeneous and varied among the vesicles. Three distinct phenotypes could be observed: (1) a network of actin bundles, which was fully localized to the membrane (Figure 5.2 phenotype1), (2) a fine volume spanning network connected to the membrane (Figure 5.2 phenotype2) and (3) a bundled network not connected to the membrane (Figure 5.2 phenotype3). The heterogeneous distribution of different phenotypes among the vesicles suggests that membrane localization of VASP was not sufficient to shift actin bundle formation towards the membrane in order to promote membrane protrusion. Actin seeds could form in the volume of the vesicle before VASP was fully adsorbed at the membrane and a volume spanning network grew.

Actin polymerization of bulk networks inside the vesicles could be completely suppressed either by using depletion forces or by controlling spontaneous actin polymerization inside the vesicle. The additional encapsulation of 2% methylcellulose to 3 µM actin and 1 µM VASP induced depletion forces within the vesicles, which pushed

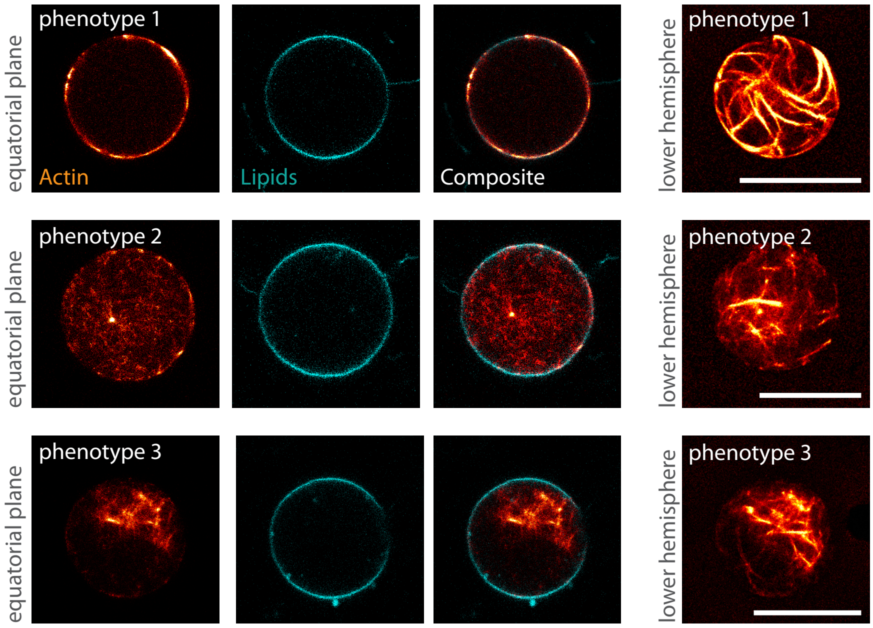

Figure 5.2: Confocal images of vesicles, which contained 1 µM VASP and 3 µM actin monomers (red hot; 10 % of the monomers were labeled with covalently bound atto 488), are shown. His-tagged VASP was specifically coupled to the membrane (cyan) via NiNTA lipids. Three different phenotypes of actin polymerization could be observed. All scale bars are 20 µm.

all actin towards the membrane and such promoted the formation of a membrane localized actin network (Figure 5.3). Also network bundling and crosslinking was enhanced as in all vesicles a bundled and crosslinked network could be observed. As a next step to study a more physiological way of restricting network formation to the membrane, polymerization kinetics of actin were controlled by adding additional ABPs to regulate network growth.The addition of 60 nM CP and 13.5 µM profilin instead of methylcellulose to the polymerization mix prior to encapsulation ensured that any spontaneous polymerization was fully suppressed inside the vesicle's volume. CP binds to barbed ends and such suppresses any elongation. Whereas profilin binds to actin monomers and such blocks actin growth at the pointed filament end. Compared to the presence of methylcellulose, the observed networks were composed of thinner bundles (Figure 5.3). Pyrene assays confirmed, that in the presence of CP and profilin filament growth slowed down as spontaneous nucleation and filament elongation was suppressed (Figure 5.4 a) and was comparable to actin polymerization without any ABPs.

For both experimental conditions the distribution of the occurring phenotypes was more homogeneous compared to the encapsulation of only actin and VASP and only one phenotype could be observed. This could be also confirmed by a quantification of membrane bind-

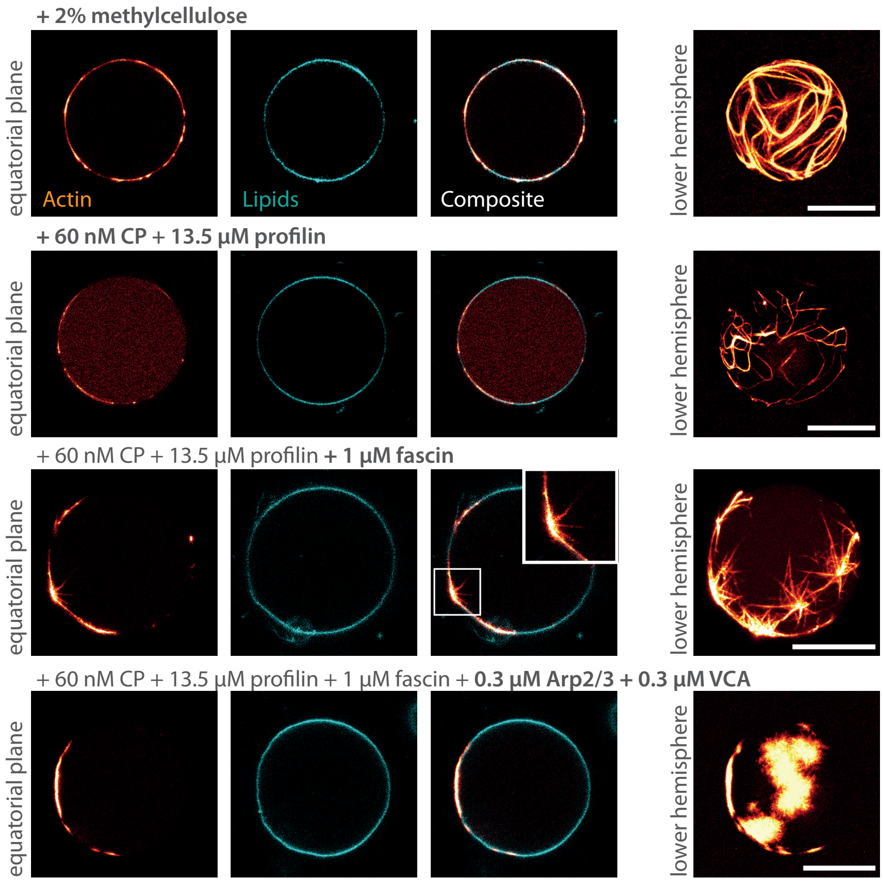
+ 2% methylcellulose
equatorial plane
Actin
Lipids
Composite
lower hemisphere
+ 60 nM CP + 13.5 µM profilin
equatorial plane
lower hemisphere
+ 60 nM CP + 13.5 µM profilin + 1 µM fascin
equatorial plane
lower hemisphere
+ 60 nM CP + 13.5 µM profilin + 1 µM fascin + 0.3 µM Arp2/3 + 0.3 µM VCA
equatorial plane
lower hemisphere

Figure 5.3: VASP mediated network formation was restricted to the membrane. For all tested experimental conditions confocal images of the equatorial plane and a z-projection of the lower hemishpere are shown. The actin channel is red hot and the membrane channel cyan. The addition of 2 % methylcellulose resulted in the formation of a membrane localized network composed of thick actin bundles. The addition of 60 nM CP and 13.5 µM profilin resulted in fine membrane localized networks. Star-like networks could be observed when 1 µM of fascin was encapsulated additional to CP and profilin and addition of 0.3 µM Arp2/3 and 0.3 µM VCA to actin, VASP and fascin induced the formation of dense actin patches at the membrane. All scale bars are 20 µm.

ing (Figure 5.4 b). Here the ratio of actin intensity measured in the equatorial plane at the membrane and in the vesicle's bulk was calculated. The dimensions of the resulting boxplots were tallest for the encapsulation of only actin and VASP, the size decreased in the presence of depletion forces and was smallest, when spontaneous polymerization was suppressed. The evaluation also revealed that membrane

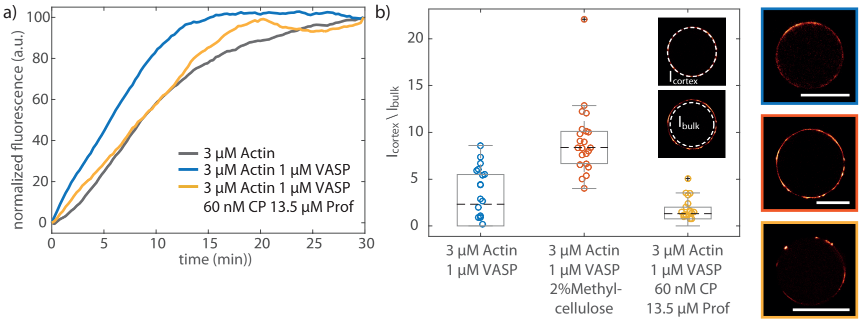

Figure 5.4: a) Pyrene measurement of filament elongation in the presence by VASP were measured with and without the suppression of spontaneous actin polymerization. b) Membrane binding was quantified for all experimental conditions (1 µM VASP, 3µM actin, 1 µM VASP, 3µM actin, 2%methylcellulose; 1 µM VASP, 3µM actin, 60 nM CP, 13.5 µM profilin) by calculating the ratio of actin fluorescence at the vesicle's membrane and inside. All scale bars are 20 µm.

localization was different. In the presence of depletion forces the ratio between the equatorial median actin intensity at the membrane and in the bulk was high, whereas it dropped when membrane polymerization was controlled by CP and profilin (Figure 5.4 b). As depletion forces were missing here, the vesicle's bulk was not fully depleted from G-actin and thus intensity values of bulk actin increased. In addition filament polymerization and bundling was less pronounced, which resulted in lower actin intensity values at the membrane.

Next we tested the effect of the crosslinker fascin on VASP mediated filopodia formation at the membrane. Fascin was added to the polymerization mix (3 µM actin, 1µM VASP, 60 nM CP and 13.5 µM profilin) prior to encapsulation. The resulting network structures looked fundamentally different compared to the absence of fascin. Star-like actin patches were built up in place of an entangled bundled actin network (Figure 5.3), which seemed to promote an inwards growth of straight actin bundles towards the vesicle's center. Also, the simultaneous formation of membrane localized dendritic and filopodia-like networks was studied as the nucleation convergent model predicts that filopodia emerge from the dendritic Arp2/3 networks, we. To this end, we added 0.3 µM Arp2/3 complex and 0.3 µM VCA to the polymerization mix (3 µM actin, 1 µM VASP, 60 nM CP and 13.5 µM profilin) prior to encapsulation. VCA is the actin binding site of the N-WASP complex and activates Arp2/3-complex. VCA also carried an

His-Tag and could therefore adsorb to the NiNTA-lipids containing membrane in order to induce network formation at the membrane. Shortly, after protein encapsulation was finished dense actin patches could be observed at the membrane (Figure 5.3). The patches grew very dense and no network structures were discernible within the domains.

5.3 MEMBRANE RESTRICTED ACTIN ELONGATION AND BUNDLING INDUCE MEMBRANE PROTRUSIONS

In this section the focus was set to study, if the experimental conditions from the section before were sufficient to induce local shape deformations of the membrane resembling to filopodia in cells. Thus the experiments were scanned again to look for any shape deformations. In the section before, the focus was only set on the network morphology at the membrane. But also, the appearance of membrane deformations induced by protruding actin bundles strongly depended on the composition of the encapsulated protein mixes. No shape deformations of the membrane were visible in any occurring phenotype, when only 3 µM actin and VASP were encapsulated. Only spontaneous membrane tubulation could be observed (Figure 5.5).

But as soon as network formation was fully restricted to the membrane either by depletion forces or controlling polymerization kinetics the formation of membrane protrusions was observable (Figure 5.5). Under both conditions short and long actin bundles grew normal to the actin cortex and formed membrane tubes already resembling to filopodia like structures. Large area deformations of the vesicle's membrane were only observed in the presence of a rigid actin cortex when depletion forces were present.

Star-like network rearrangement in the presence of VASP further enhanced shape deformations of the membrane, as no vesicles could be observed without any deformation. In about 50 % of the vesicles protrusion formation could be observed, whereas in the other half of the vesicle population large-area deformation could be observed (Figure 5.5).

The simultaneous formation of membrane localized Arp2/3 and VASP mediated networks did not promote the formation of protrusions at all. Only in 9 % of the vesicles the formation of actin protrusion pushing the membrane forward could be observed. Large-area deformations were still visible in about 40 % of the vesicles.

Not only the number of protrusions diminished in the presence of Arp2/3 and VCA, also protrusion length clearly decreased (Figure 5.6). In the presence of fascin it decreased only slightly and the average length was the highest in the presence of depletion forces or CP and profilin.

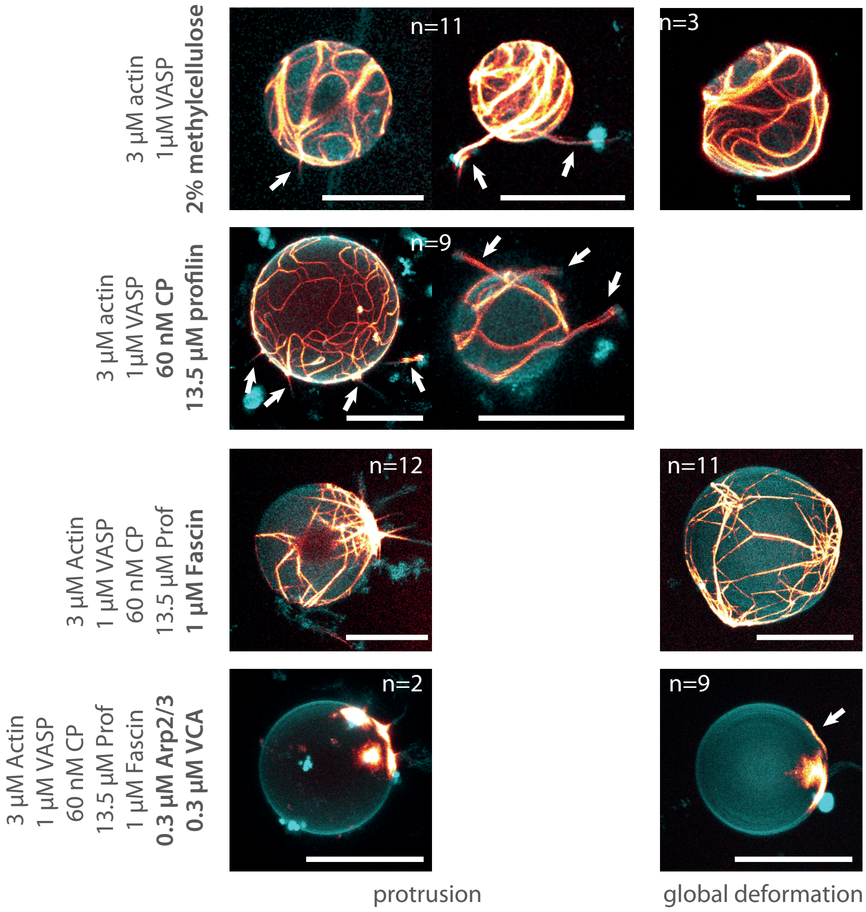
3 µM actin
1µM VASP
2% methylcellulose
n=11
n=3
3 µM actin
1µM VASP
60 nM CP
13.5 µM profilin
n=9
3 µM Actin
1 µM VASP
60 nM CP
13.5 µM Prof
1 µM Fascin
n=12
n=11
3 µM Actin
1 µM VASP
60 nM CP
13.5 µM Prof
1 µM Fascin
0.3 µM Arp2/3
0.3 µM VCA
n=2
n=9
protrusion
global deformation

Figure 5.5: Confocal overlays of the lower vesicle's hemispheres of the membrane (cyan) and actin channels (red hot) are shown. Shape deformations of the membrane could be only observed, when polymerization was sufficiently shifted towards the membrane. Protrusion formation was observed when either 2 % of methylcellulose (N=20) or 60 nM CP and 13.5 µM profilin in the absence (N=17) or presence of 1 µM fascin (N=23) were added to the protein mix prior to encapsulation. The number of vesicles with membrane protrusions decreased upon the addition of 0.3 µM Arp2/3 and 0.3 µM VCA (N=23). N denoted the total number of investigated vesicles, whereas n denotes the number of vesicles presenting the indicated deformation. All scale bars are 20 µm.

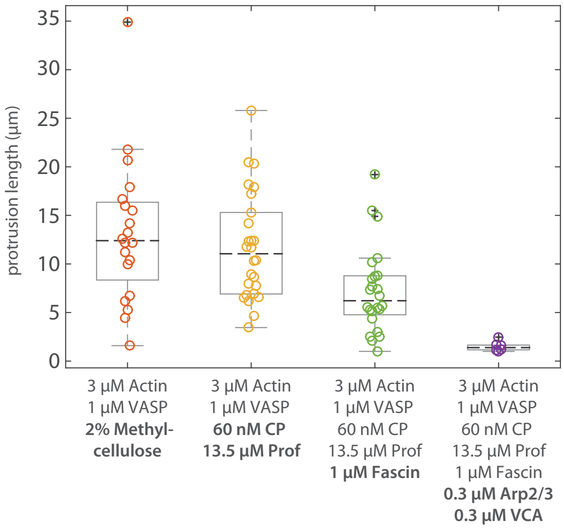

Figure 5.6: Combined dot density plots and boxplots show protrusion length distribution dependent on the different experimental conditions.

5.4 FLUORESCENTLY LABELED VASP LOCALIZES TO THE MEMBRANE LOCALIZED ACTIN NETWORK AND FILOPODIA

In a last set of experiments we focused on the localization of VASP within the polymerized network structures in the presence of CP and profilin. To this end, 20% of the unlabeled VASP were replaced by covalently labeled atto647N VASP. We found a direct co-localization between the membrane connected actin network and the VASP signal (Figure 5.7 on the top). The observed VASP intensity correlated with the actin filament thickness indicating that VASP accumulates within actin bundles and such promotes crosslinking.

The co-localization of long actin bundles forming a filopodium and VASP could be also observed. The intensity distribution of VASP along the actin bundle was rather inhomogeneous and correlated to flexibility of the actin filopodium (Figure 5.7 on the bottom). At the anchor point of the filopodium and the membrane localized network, VASP intensity was high resulting in an stiffer actin bundle and therefore showed less flexibility in the overlay of both fluorescent channels. In areas with lower VASP intensity the imaged actin bundles were not sharp indicating a higher bundle flexibility. High VASP intensities inside the vesicles indicate that not all of the VASP molecules were bound to the membrane. Still actin polymerization was only visible at the membrane.

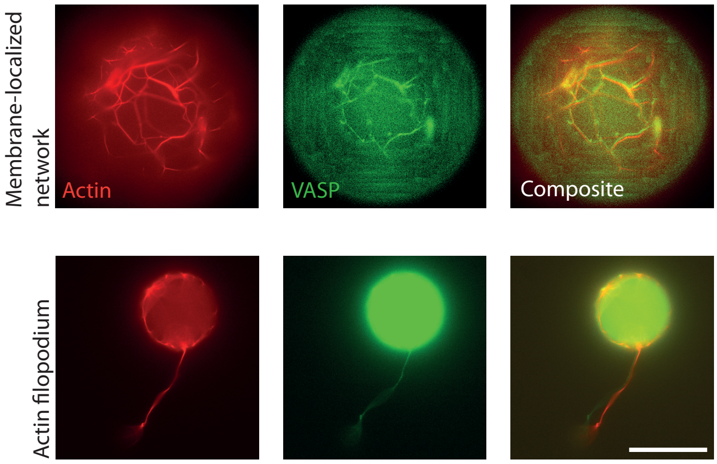

Figure 5.7: Epifluorescence images are shown of vesicles, in which 3 µM actin, 1 µM VASP, 60 nM CP and 13.5 µM profilin were encapsulated. 20 % of VASP were covalently labeled with atto 647N in order to visualize the VASP distribution. On the top, the VASP distribution in a membrane localized actin network (red) is shown. Here, VASP partly co-localizes with the actin. On the bottom, the equatorial vesicle plane with a filopodium growing away from the vesicles is shown. It can be seen that VASP is present inside the filopodium and the bulk of the vesicle. Scale bar is 20 µm.

5.5 DISCUSSION

In this in-vitro study it was shown that a minimal set of cytoskeletal proteins was sufficient to drive filopodia formation at membranes in the absence of any dendrite network structures. Branched network formation is not required to form filopodia and thus "the elongation tip" model could be a possible explanation for filopodia formation in cells [43, 143, 167]. It was the binding of VASP to the vesicle's membrane and suppression of any bulk actin polmyerization, which finally promoted the formation of actin bundles. The protrusions grew several μm long and therefore the number of actin filaments inside the bundles can be estimated to 20-30 filaments [96]. At this filament number protrusion against a membrane resistance of 10-50 pN is most efficient before protrusion is limited by monomer diffusion or filament buckling. Based on the Brownian Ratchet Model (Section 2.1.1.1) the force per filament is about 10 pN and thus a filopod of 20 filaments could create a force up to 200 pN, which is more than sufficient to push forward the membrane and such promote the formation of membrane tubes [113].

The encapsulation of only actin and VASP resulted in various phenotypes as nucleation and consecutive filament growth was not controlled and therefore actin polymerization was not restricted to the membrane. Depletion fores induced by the encapsulation of additional methylcellulose pushed all actin towards the membrane and such enabled membrane localized actin polymerization. Moreover the depletion forces also promoted the formation of thick actin bundles, which were not only stiff enough to induce large-area deformations of the membrane, but also actin filopods emerged from the rigid network and were able to create membrane protrusions. The effect of crosslinking by methylcellulose was consistent with already published data, where depletion forces formed stiff actin bundles inside of droplets, even in the absence of any crosslinking proteins [34].

But even in the absence of depletion forces when spontaneous polymerization was only controlled by the adjustment of the polymerization kinetics via CP and profilin, actin polymerization was fully localized towards the membrane despite the presence of fluorescently labeled actin monomers and VASP in the vesicle's bulk. This corroborates the view that VASP has no anti-capping function inside the vesicle but shields barbed ends from being capped by CP when bound to surfaces [9, 25, 26]. The localization of VASP via His-Tag was also sufficient to promote filament bundling in the absence of depletion forces. VASP molecules mulitmerizes and as they carry FAB domains, they also have the ability to bundle and crosslink actin filaments sensitive to the VASP concentration, which is consistent with other in-vitro measurements [24, 53, 129]. Also in cells the bundling and crosslinking properties of VASP can promote filopodia assembly as the formation of actin bundles facilitates the binding of VASP tetramers due to the presence of more FAB-attachment sides [60]. In addition, only reexpression of VASP with intact FAB domains could rescue filopodia formation in VASP deficient cells [129].

Addition of fascin stiffened the observed networks further as large area deformations of the membrane were visible. The network morphology changed completely. The presence of fascin induced a starlike rearrangement of the membrane localized network. These observations are consistent with in-vivo data, where star-like actin patterns have been observed in B16-F1 mouse melanoma cells, when filopodia formation was enhanced due to the knock-down of CP. The center of the observed stars was rather thick. Thus fascin might form membrane bound actin clusters at the first nucleation sites. Membrane localized VASP then ensures further elongation of the bundles and star-like patterns are formed. Surprisingly, the number of vesicles presenting actin induced membrane tubes did not increase, even though it was predicted in theory and found in-vivo that a sufficient network stiffening is required for efficient filopodia formation [95, 96, 160]. Along these lines it was found that fascin increases the Young's modulus of Arp2/3 mediated actin comet tails in the presence of VASP [145]. But the increased inwards growth of actin filopodia emerging from the star center could explain decreased membrane filopodia formation. Formation of a dense volume spanning network or encapsulation of a dense polymer network could stir filament elongation towards the membrane and such promote filopodia formation. The actin or polymer network would serve as a stable base against filaments can push.

The simultaneous polymerization of dendritic networks by Arp2/3 also did not enhance the formation of membrane tubes, as observed in cells and predicted by the "convergent elongation" model [60, 149]. Patch formation by Arp2/3 was much faster than VASP mediated polymerization as Arp2/3 mediated polymerization is autocatalytic. In contrast, actin polymerization by VASP is continuous and takes at least 15 minutes in the presence of CP and profilin. Therefore, most of the actin is already used up before VASP initiates filaments elongation and bundling to form actin filopodia.

To sum up, the fully reconstituted model system is capable to recapitulate the basic functions of VASP mediated actin polymerization and gives further insights in the mechanical interplay between actin-membrane interactions. Only sufficient membrane polymerization and network bundling promoted the formation of membrane protrusions. Still more experiments are required to fully understand the force balance during filopodia formation. Here, the encapsulation of actively treadmilling networks should be a step forward as only a dynamic system can remodel the predictions, made in the "convergent elongation" model, and transition of Arp2/3 nucleated networks towards stiff actin filopodia formed by Ena/VASP or formins could be reconstituted.

6

RECONSTITUTED ACTIVE ACTIN CORTICES IN GUVS RESHAPE MODEL MEMBRANES

A modified protocol of cDICE was evolved to encapsulate Xenopus laevis extract inside of GUVs to reconstitute active actin cortices on a free standing flexible membrane. Cortex formation could be only observed when the Arp2/3 activator VCA was bound to the membrane. As long as the actin cortices bound homogeneously to the membrane, no local shape deformation was observed. Addition of α-actinin increased network connectivity, whereas the addition of myosin motors induced a symmetry break of the actin cortex. Stable actin domains became visible, which were able to induce local membrane deformations. Either a negative bending of the membrane or membrane blebs were observed. Warming the sample to 35°C induced a global contraction of the acto-myosin gel even in the absence of additional crosslinkers and a full vesicle collapse was observed. Our protocol allows for the first time to encapsulate Xenopus laevis extract inside of GUVs and recovers basic membrane deformations resembling to cellular processes like migration via membrane blebbing or endocytosis.

6.1 EFFICIENT RECONSTITUTION OF ACTIVE CORTICES IN GUVS

Xenopus laevis extract was encapsulated inside of GUVs using a modified emulsion transfer technique (cDICE) [1]. Due to the high protein density of the extract and thus high viscosity the encapsulation protocol was modified to ensure an efficient and reproducible extract encapsulation. Most important the extract was clarified and diluted prior to encapsulation. A mixture of salts, labeled actin monomers, additional proteins and 3.6% extract was encapsulated. The actin concentration of undiluted extract was determined by electrophoresis and was estimated to be about 50 µM. Thus the total amount of encapsulated actin was about 5 µM including 1 µM of Atto488-actin to image the actin dynamics (Figure 6.1).

During encapsulation the extract droplets pass a lipid-oil layer. We had to ensure that lipid adsorption to the extract-oil interface was faster than protein adsorption. Therefore the lipid aggregate size was tuned by adjusting the oil composition (silicone oil:mineral oil:decane 0.8:0.14:0.06). The lipid membrane was composed of a mixture of DOPC, Ni-NTA, Peg-PE, PEG-Biotin lipids and Texas Red. The presence of NiNTA enables to bind His-Tagged proteins to the membrane and PEG-PE to suppress unspecific protein-membrane interactions.

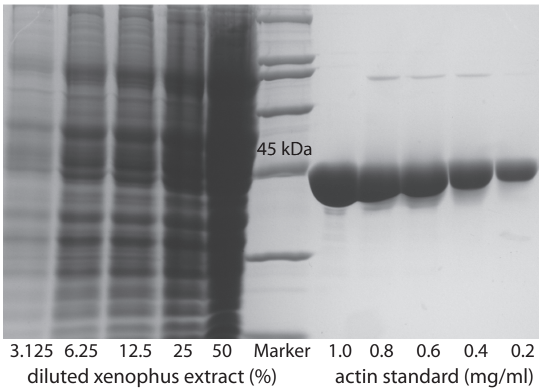
45 kDa
3.125 6.25 12.5 25 50 Marker 1.0 0.8 0.6 0.4 0.2
diluted xenophus extract (%)
actin standard (mg/ml)

Figure 6.1: Different dilutions of Xenopus extract were transferred on an electrophoresis gel to estimate the intrinsic actin concentration by comparison to an actin standard. Comparison of stain intensity and area of the actin bands of the extract and the standard gave an intrinsic actin concentration of about 50 µM.

PEG-Biotin lipids were used to immobilize the GUVs on a streptavidin coated cover slip and Texas Red DHPE to image the membrane. During encapsulation the extract solution phase separates in an extract-poor and extract-rich phase. Therefore only 50% of the fabricated vesicles (30-40 vesicles) could be used for our analysis. In the remaining 50% either no or only low amounts of extract were present. The average diameter of vesicles used for analysis was about 20 µm. After production, vesicles remained stable for at least half a day. Encapsulation of Xenopus laevis extract in the absence of any additional Actin binding proteins (ABPs) resulted in the formation of a volume spanning actin distribution inside the vesicle (Figure 6.2).

Addition of His-Tagged VCA prior to encapsulation resulted in the formation of a continuous actin cortex at the membrane. His-Tagged VCA bound to the membrane via Ni-NIA lipids and activated Arp2/3 complex, which was present in the extract. As a consequence formation of a continuous membrane localized branched actin network was initiated (Figure 6.2 c). Membrane localization of actin was dependent on the amount of added His-Tagged VCA and was most efficient at a concentration of 30 µM (Figure 6.2 b and Figure 6.3). At all VCA concentrations no shape remodeling of the membrane was observed. Fluorescence Recovery After Photobleaching (FRAP) experiments were performed at 20°C to verify that the actin cortices are active. Fast actin recovery was observed within the first 30 sec after a µm-sized area of the equatorial cortex was bleached (Figure 6.2 c). Thus actin incorporates continuously into the cortex.

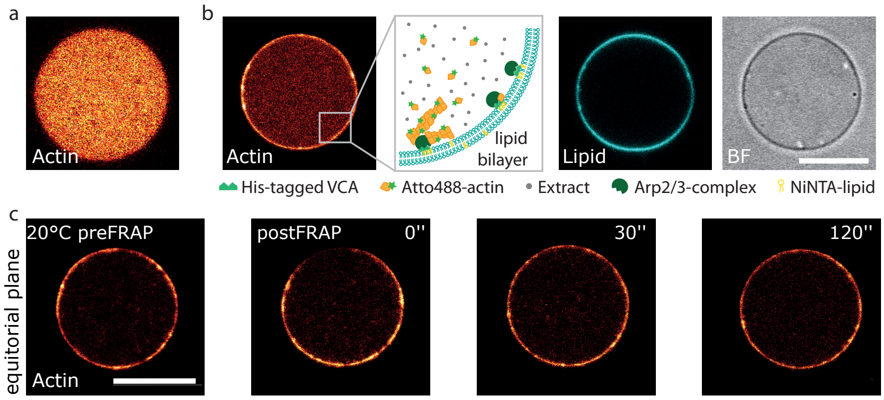
a
b
Actin
Actin
lipid
bilayer
Lipid
BF
His-tagged VCA
Atto488-actin
Extract
Arp2/3-complex
NiNTA-lipid
c
equitorial plane
20°C preFRAP
Actin
postFRAP
0''
30''
120''

Figure 6.2: a) The equatorial plane of a vesicle, in which a dilution of Xenopus extract and 1 µM Atto488-actin were encapsulated, is shown. b) The equatorial plane of a vesicle with an actin cortex attached to the membrane is shown. Cortex formation was induced by the addition of 30 µM His-Tagged VCA to the extract solution prior to encapsulation. The lipid channel is shown in cyan and the bright-field channel in gray. c) Fluorescent recovery experiments of the acto-myosin cortex are shown. Here 15 µM of of His-Tagged VCA were used. All scale bars are 10 µm.

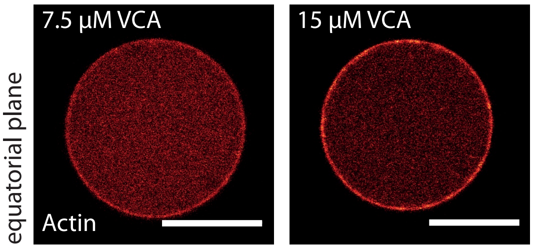
equatorial plane
7.5 µM VCA
Actin
15 µM VCA

Figure 6.3: Confocal images of the equatorial plane of vesicles, which contain Xenopus extract and different amounts of His-Tagged VCA, are shown. All scale bars are 10 µm.

6.2 EFFECT OF α-ACTININ ON CORTEX STRUCTURE

Addition of 0.5 µM α-actinin prior to encapsulation led to the formation of actin domains, which were $\sim$2 µm large (Figure 6.4 a top row). Despite domain formation still an actin cortex was present, which interconnected the actin domains. α-actinin locally stabilizes actin filaments and prevents them from disassembly. This is consistent with a FRAP measurement of an actin domain formed in the presence of 2 µM α-actinin. A recovery of the bleached domain could not be observed. Thus actin accumulation was promoted rather than disassembly. This is confirmed by the observation that the fluorescence signal of the actin domain was much higher than the signal of the actin cortex in the absence of any α-actinin. Domain intensity and size increased with an increasing amount of α-actinin (Figure 6.4 a row 2-4). At a concentration of 0.5 µM the volume of most domains was smaller than 1 µm^3, about 18% had a volume between 1 and 10 µm^3 (Figure 6.5). At 1 µM or 1.5 µM α-actinin the frequency of domains with a volume between 1 to 10 µm^3 increased to 22% and frequency increased to 16% for domains larger than 10 µm^3. A final increase to 2.4 µM α-actinin clearly increased the domain volume. Only 23% of the domains were smaller than 1 µm^3, 51% were between 1 and 10 µm^3 and 26% of the domains were larger than 10 µm^3 (Figure 6.5).

Domain formation was dependent on the amount of encapsulated His-Tagged VCA. In the absence of any His-Tagged VCA neither at 1 µM nor at 2.4 µM α-actinin domain formation was observed. At 7.5 µM His-Tagged VCA the actin cortices became inhomogeneous and areas of high density appeared within the cortex when α-actinin was present (Figure 6.6). Clearly separated domains could not be observed. Only when actin polymerization was effectively shifted towards the membrane, spatially separated domains could be observed. The size of the inhomogeneities within the cortex correlated to α-actinin concentration.

6.3 MEMBRANE BENDING AND BLEBBING INDUCED BY INHOMOGENEITIES IN THE ACTIN CORTEX

At all studied α-actinin concentrations actin domains were able to induce shape deformations of the membrane. Two deformation modes could be observed. Either the membrane bent inwards (negative curvature) or membrane blebs with a positive curvature were formed (Figure 6.7). The interaction between the actin domains and the membrane was different for both deformation types. In case of a negative bending the membrane was tightly coupled to the actin domain and adapted its curvature to domain shape. For membrane bleb formation the mechanical interplay was different. Only at the bleb bottom an actin domain was tightly coupled to the membrane. Both defor-

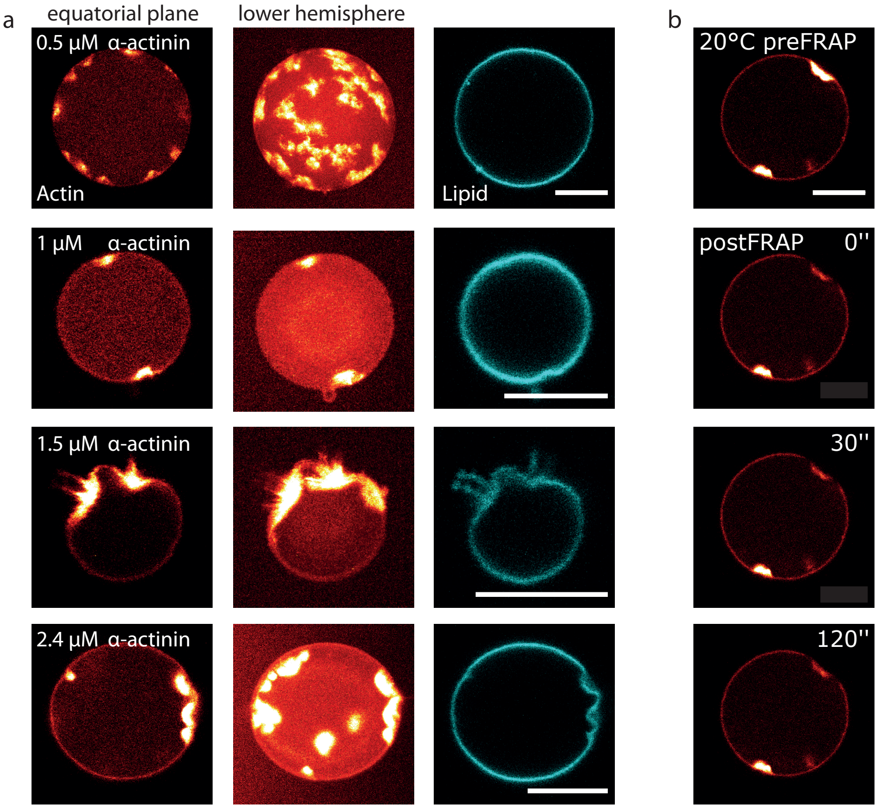
a
equatorial plane
lower hemisphere
0.5 µM α-actinin
Actin
Lipid
1 µM α-actinin
1.5 µM α-actinin
2.4 µM α-actinin
b
20°C preFRAP
postFRAP 0''
30''
120''

Figure 6.4: a) Confocal images of the equatorial plane of the actin (red hot) and lipid channel (cyan) and the lower hemisphere of the actin channel (red hot) are shown at different α-actinin concentrations. A mixture of 7.3% Xenopus extract, 1 µM labeled Atto488-actin, 30 µM His-Tagged VCA and the indicated concentration of α-actinin were encapsulated. b) FRAP measurements of an actin domain were taken to study the dynamics of actin domains. The concentration of α-actinin was 2 µM. All scale bars are 10 µm.

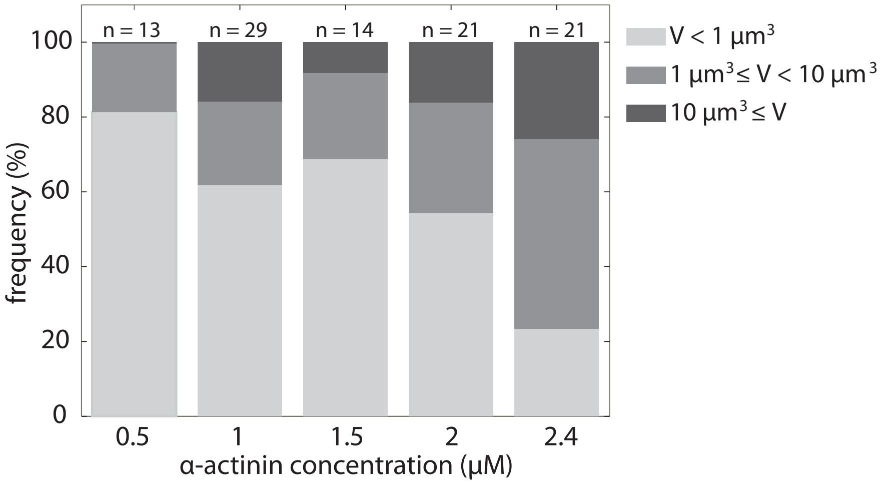

Figure 6.5: A histogram of the domain volume dependent on α-actinin concentration is shown. The domains were split in three subgroups dependent on their volume. Domains were either < 1 μm^3, between 1-10 μm^3 or > 10 μm^3. All experiments were performed at 20 °C.

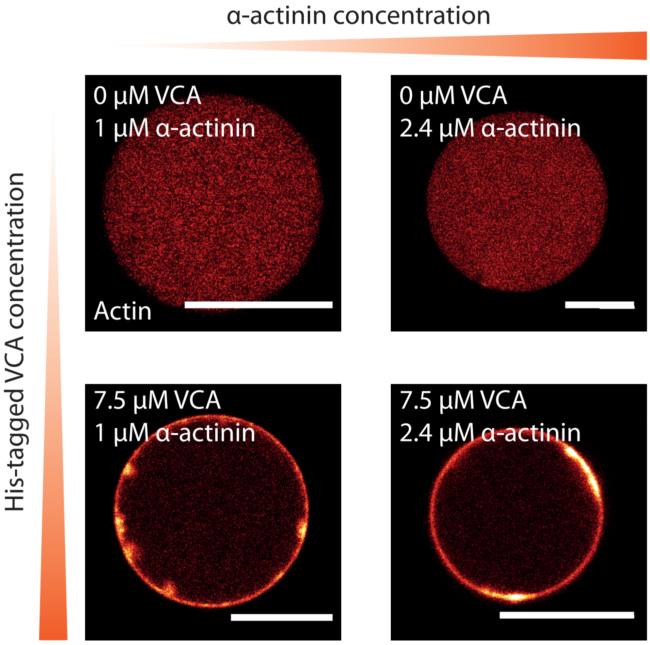
α-actinin concentration
His-tagged VCA concentration
0 μM VCA
1 μM α-actinin
Actin
0 μM VCA
2.4 μM α-actinin
7.5 μM VCA
1 μM α-actinin
7.5 μM VCA
2.4 μM α-actinin

Figure 6.6: Confocal images of the equatorial plane of vesicles filled with 7.3% extract, either 1 μM or 2.4 μM α-actinin, 1 μM labeled Atto488-actin and either 0 μM or 7.5 μM His-Tagged VCA are shown. All scale bars are 10 μm.

mation types could be observed simultaneously in the same vesicle. The shape remodeling depended on the concentration of α-actinin (Figure 6.7). Membrane blebs were not only observed at concentrations above 0.5 µM α-actinin but also increased their frequency with an increasing α-actinin concentration (Figure 6.8). Negatively shaped membranes occurred at all studied α-actinin concentrations.

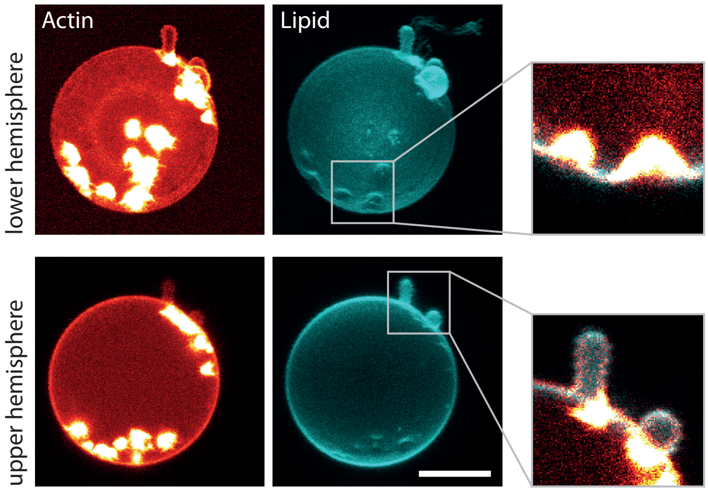

Figure 6.7: Confocal reconstruction of the lower and upper hemisphere of a vesicle presenting both deformation types are shown. 3.6% extract, 1 µM Atto488-actin, 30 µM His-Tagged VCA and 3 µM α-actinin were encapsulated inside GUVs. The actin channel is presented in red hot and the lipid channel in cyan. The two insets show overlays of the actin and lipid channel of both deformation types. The upper inset depicts a negative membrane bending, whereas the upper vesicle shows a membrane bleb. All scale bars are 10 µm.

6.4 ACTIN CORTEX COLLAPSE INDUCED BY GLOBAL MYOSIN CONTRACTION

Vesicles, where a cortex was formed in the absence of α-actinin, collapsed when they underwent a temperature change from 4°C to 35°C (Figure 6.9). As soon as the sample was placed on the microscope stage for imaging the actin cortex was already formed. It remained stable for the first 5 minutes and completely collapsed afterwards. The cortex did not detach from the membrane rather it remained tightly connected and such induced crumpling of the membrane when it collapsed. Contraction of the cortex and thus of the membrane lasted for 8 minutes after the collapse. The collapse did not correlate to vesicle's diameter and occurred rarely. It was only observed in about 10% of the vesicles. When the same experiment was repeated in the presence of α-actinin no vesicle collapse was observed in any of the imaged vesicles (Figure 6.9). Instead the actin domains were

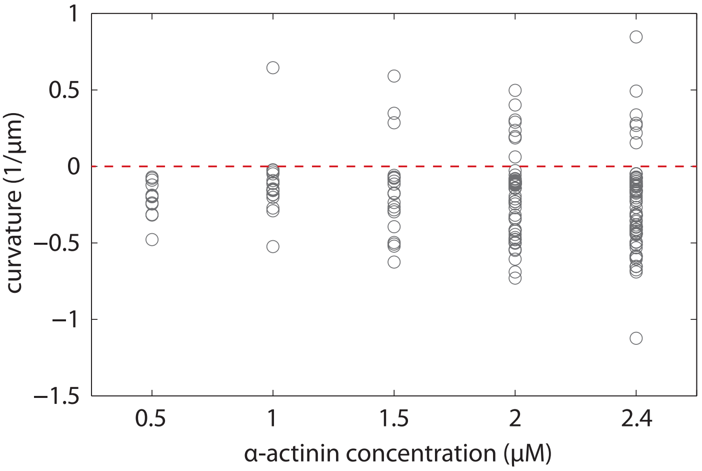

Figure 6.8: The curvature of the positive and negative bent membrane shapes were measured dependent on the α-actinin concentration. To measure the curvature a circle was fitted to the membrane shape and curvature was calculated from the inverse of the fitted circle radius.

present immediate at the membrane and remained stable during image acquisition.

6.5 DISCUSSION

Here we could show that Xenopus laevis extract can be encapsulated inside of GUVs by using a modified protocol of cDICE and we were able to reconstitute active actin cortices at flexible membranes. The experiments were inspired by the work of Enas Abu Shah and Kinneret Keren. They developed a protocol to encapsulate actin intact extract inside of droplets and reconstructed different cellular phenomena including cortical symmetry breaking [4]. Our approach could recover some of their observations and allowed additional insights into the mechanical interplay of active actin cortices and cellular membranes. We confirm that cortex formation requires the presence of Arp2/3 activators at the membrane. Moreover cortex formation was dynamic. However, a symmetry break of the cortex at 20°C could not be observed in our experiments rather cortex formation was homogeneous. A symmetry break was only achieved upon addition of the crosslinker α-actinin. But the encapsulated amount of extract in our study was about 5 times lower compared to the droplet experiments. Therefore we assume that network density and connectivity was not sufficient to observe a myosin induced symmetry break at low temperatures. Only the addition of α-actinin could provide sufficient network connectivity. Also at temperatures above 25°C or at high pH values, when network connectivity was low, addition of α-actinin recovered contractile behavior of the cortex and symmetry breaks were observable [4,

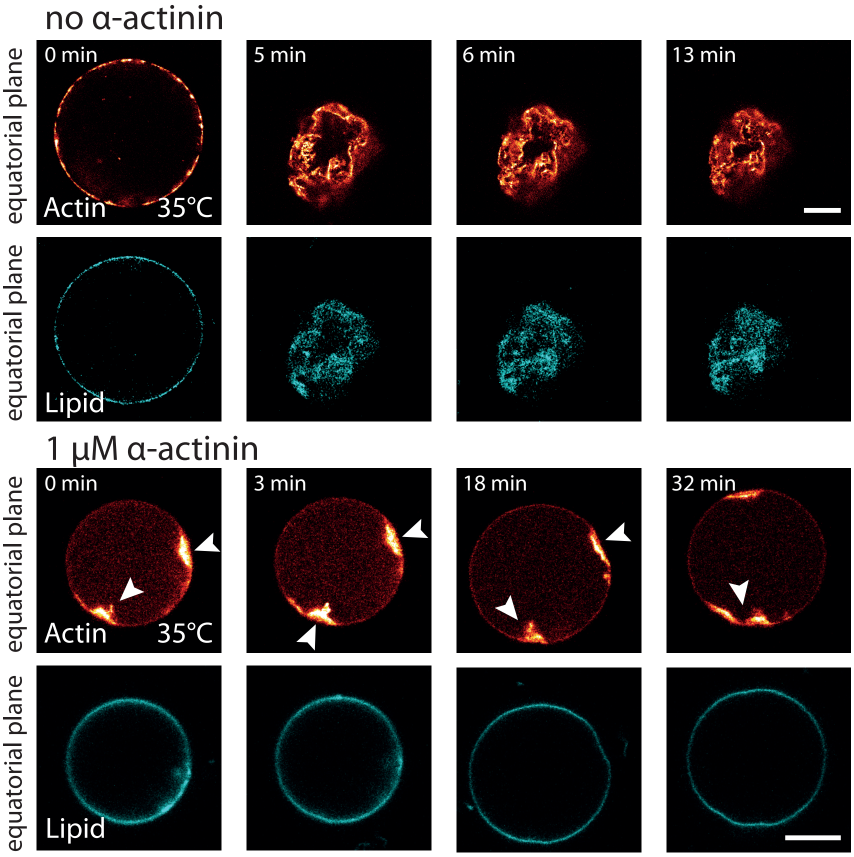
no α-actinin
0 min
5 min
6 min
13 min
Actin
35°C
Lipid
1 µM α-actinin
0 min
3 min
18 min
32 min
Actin
35°C
Lipid
equatorial plane
equatorial plane
equatorial plane
equatorial plane

Figure 6.9: Confocal images of the equatorial plane of a vesicle filled with 7.3% extract, 1µM Atto488-actin, 30 µM His-Tagged VCA and either no α-actinin or 1 µM α-actinin are shown. Vesicles were stored on ice before imaging and immediately heated up to 35°C, when they were placed on the microscope. Imaging was started immediately. White arrows mark the same actin domains. Vesicles rotated despite fixation on the cover-slip via biotin-streptavidin and thus domain position varied. All scale bars are 10 µm.

76].

In droplet experiments only a global deformation was observable. The reason is that surface tension is high in droplets and thus normal forces pulling against the interface were not sufficient to induce any shape deformations [23, 42]. Only tangential force components induced an internal cortex reorganization and a global deformation of the droplet's shape [4]. Instead in vesicles the surface is deformable and two types of membrane deformation became visible when network connectivity was sufficiently high. The mechanism is different for both deformation types. In case of a negative membrane bending shape remodeling relies on the actin polymerization kinetics controlled by various ABPs present in the extract [39]. The addition of α-actinin might stabilize the polymerized actin structures and prevents them from disassembly. This was confirmed by FRAP measurements of actin domains and is consistent with already published work [100, 127]. The presence of molecular motors in the actin domains further stabilizes and enhances negative membrane bending [39]. In case of membrane blebs acto-myosin contraction increases tension locally, which results in an internal overpressure at the membrane. The overpressure tends to push water outside, but osmotic pressure prevents a vesicle collapse [89]. As soon as the actin gel detaches from the membrane such an overpressure induces the formation of a membrane bleb [32, 89, 126]. Bleb formation was only observed at high α-actinin concentrations. Thus we assume that sufficient network connectivity is required for efficient acto-myosin contraction to increase membrane tension. The encapsulation of extract into vesicles allowed to recover both deformation types simultaneously as the whole actin polymerization machinery was present [15, 47].

Global contraction of the acto-myosin gel initiated a full vesicle collapse and was observed even in the absence of any α-actinin. A sudden increase of temperature from 4° to 35°C was sufficient to trigger contraction. The temperature raise increases ATPase activity of myosins and the motors become more active [11, 168]. The high motor activity counteracts low network connectivity and contraction is visible even in the absence of any additional crosslinkers. These results were consistent with bulk gelation assays, where large contractions of the gelated acto-myosin gel were visible when warming to room temperature [47]. The full vesicle collapse might not only result from the fast acto-myosin contract, rather a generic friction-driven mechanism might also come into play. When the actin myosin gel locally pulls small membrane tubes, tension increases continuously until the collapse. The remaining membrane bound network behaves as a diffusion barrier and lipids cannot diffused in the pulled tubes [138].

To conclude, we find that acto-myosin gels are able to induce various deformation types of the membrane. However, only when actin domains were stabilized by a crosslinker, shape deformations became visible. Our approach is an essential step to rebuild artificial cells as now the implementation of long term protein expression becomes possible [106]. Moreover studying the interaction of the actin cyotskeleton and the mitotic spindle inside of GUVs should recover the basic deformation steps of cell division [56, 61].

7

PHASESEPARATION

A protocol for the formation of phase separated vesicles by cDICE is developed as the use of phase separated membranes is of high interest for biophysicist. They can be used to remodel inhomogeneous membrane organization [134, 136, 137] and thus allow to study the interdependence of lateral membrane organization with the cytoskeleton in detail [65, 77, 86, 148].
So far the production of phase separated vesicles by cDICE is limited since only low fractions of cholesterol (<10%) incorporate into the membrane. But separation into a L_o and L_d requires the presence of cholesterol in the bilayer [155] and thus could be only observed upon external addition of cholesterol to already formed vesicles [21]. In this study also a low incorporation efficiency of cholesterol was measured, which could be directly correlated to the presence of mineral oil in the lipid-oil mixtures. Only in the absence of any mineral oil enough cholesterol segregated to the vesicle's membrane and phase separation into a liquid-liquid coexistence could be observed. The yield of phase separated vesicles could be improved significantly, when an additional lipid-oil layer was introduced before the glucose solution. This layer was free of mineral oil, but contained cholesterol. With this protocol almost 100% of the vesicles phase separated into a liquid-liquid coexistence below the miscibility temperature T_M. Membrane morphology depended on the ratio between the low melting temperature lipid (DOPC) and the high melting temperature lipid (DPPC). It turned out that the L_d phase can be functionalized by NiNTA lipids and specifically binds His-tagged proteins. Surprisingly, NiNTA did not functionalize the L_d phase homogeneously rather formation of NiNTA domains within the phase could be observed. In summary, we found a robust protocol to form phase separated vesicles with cDICE that will open up a complete new set of experiments to study the interaction of a confined cytoskeleton and the membrane.

7.1 PHASE SEPARATED VESICLES PRODUCED BY CDICE

7.1.1 *Liquid-liquid coexistence depends on mineral oil content*

The first experiments show that incorporation efficiency and thus phase separation into a liquid-liquid coexistence depends on the presence of mineral oil. For vesicle fabrication, a mixture of 30% DPPC, 30% DOPC and 40% cholesterol was dissolved in a mixture of 14% mineral oil, 6% decane and 80% silicone oil. To visualize phase separation, a small fraction of the fluorescent lipid TexasRed DHPE (0.03%), which is known to sort into the liquid disordered phase, was added to the lipid-oil mixture. Phase separation only occurred in about 20% of the observed vesicles (Figure 7.1). The boundaries between two phases were non circular and not very dynamic, which is characteristic for the separation into a gel-like phase (dark) and a L_d (bright) [10, 154]. The remaining 80% of the vesicles were not phase separated and the dye was homogeneously distributed within the lipid bilayer. A decrease of mineral oil to 7% did not improve the production of phase separated vesicles. Only about 10% showed phase separation at all and again that the observed phase boundaries were non-circular (Figure 7.1).

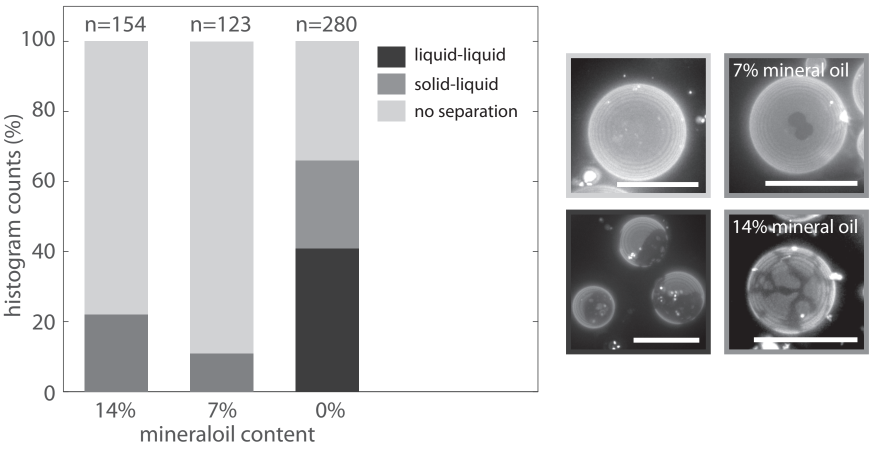

Figure 7.1: Vesicles were produced from lipid-oil mixtures containing DOPC/DPPC 1/1 and 40% cholesterol. The emergence of phase separation within the vesicle's bilayer depended on the concentration of mineral oil in the lipid-oil mixtures. The number of phase separated vesicles decreased, when mineral oil was present in the lipid-oil mixture. Liquid-liquid phase coexistence (dark frame) could be only observed in the absence of any mineral oil. On the right side the occurring vesicle's morphologies are shown. Vesicles are either not separated (light grey frame), or segregate into a gel-like and liquid phase (middle grey frames) or separate into a liquid-ordered and -disordered phase (dark grey frame). Scale bars are 20 µm.

Mineral oil was completely omitted in the lipid oil mixtures to determine its influence on phase separation. More than 60% of the vesicles showed phase separation, the rest was not phase separated. In about 40% of the phase-separated vesicles, the bilayer segregated into large bright and dark domains (Figure 7.1). The boundaries were circular and fusion of smaller domains into larger ones could be observed. These observations are typical for the coexistence of two liquid phases, a bright L_d and a dark L_o phase. They only appear, when enough cholesterol ($\leq 15\%$) is incorporated into the membrane.

Cholesterol together with the high-melting temperature lipid (DPPC) forms the liquid-ordered phase.

7.1.2 *Lipid aggregate size is controlled by cholesterol and mineral oil*

Due to the amphiphatic character, lipids are not soluble in oil and thus form aggregates. The aggregate size controls the emulsion's turbidity and depends on the hydrophobic and polar properties of the lipids and oil composition. Turbidity was quantified by measuring the optical density of the lipid oil mixtures by light scattering at a wavelength of $\lambda = 600nm$. The oil mixture was composed of 6% decane, 14% mineral oil and 80% silicone oil. A maximum concentration of 0.5 mM lipids (including cholesterol) were dissolved in the mixture. We expected a decrease of turbidity, when the percentage of cholesterol in the oil mixture increases. Cholesterol posses only a single polar hydroxyl headgroup, is therefore more hydrophobic than phospholipids and thus better soluble in the oil. Indeed the optical density decreased from 0.4 to 0.05 with an increasing portion of cholesterol (Figure 7.2).

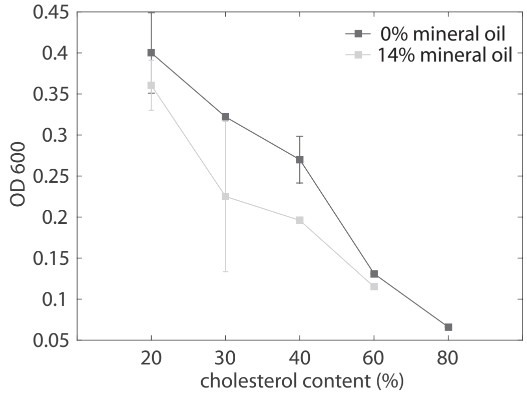

Figure 7.2: The opitical density at $\lambda = 600nm$ was measured to quantify the turbidity of the lipid oil mixtures in the presence (light grey) and absence of mineral oil (dark grey).

Apart from varying the cholesterol percentage, also the composition of the oil mixtures was changed. It was found that the turbidity increased in the absence of any mineral oil (Figure 7.2), which can be attributed to a decreased solubility of cholesterol in an oil mixture composed of 6% decane and 94% silicone oil.

7.1.3 *Cholesterol incorporation in the lipid membrane via double layer cDICE*

As the formation of vesicles with a liquid-liquid coexistence was enhanced in the absence of any mineral oil, we adapted the cDICE protocol and inserted an additional oil layer without mineral oil in the fabrication chamber. To this end we replaced the last 1/3 of the lipid-oil layer by a mixture composed of 6% decane and 94% silcone oil with maximum concentration of 0.5 mM lipids (Figure 7.3). The rest of the fabrication protocol remained unchanged. Thus protein droplets pass two different layers of lipid-oil mixtures instead of one, which is the reason that this modified version of cDICE is called double layer cDICE (dlcDICE). At first, a layer without cholesterol, but 14% mineral oil (LO1) and second a layer containing the desired amount of cholesterol, but no mineral oil (LO2).

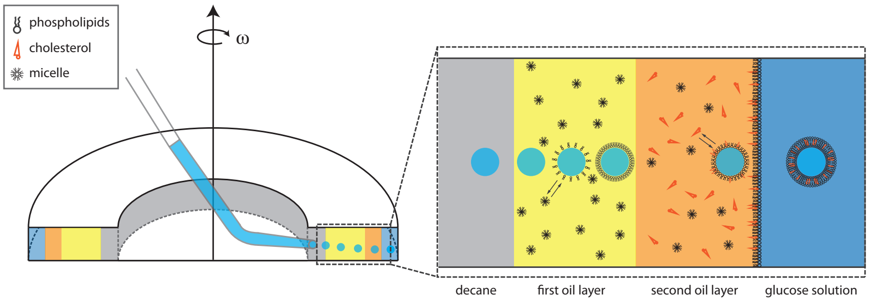

Figure 7.3: The formation of phase separated vesicles produced by double-layer (dl-cDICE) is shown. An additional lipid-oil mixture, in which mineral oil is not present and thus cholesterol is more soluble, is inserted into the cDICE chamber.

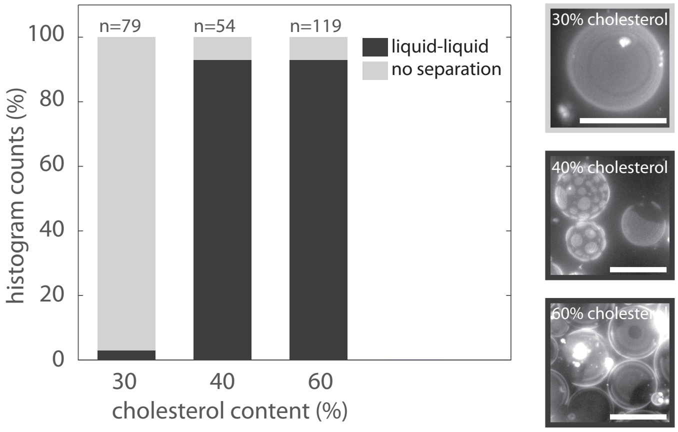

Figure 7.4: The appearance of liquid-liquid coexistence of the two lipid phases in vesicle depends on the cholesterol content in the lipid-oil mixture. The occurring morphologies are shown next to the histogram. The vesicle do not phase separate at low cholesterol contents (light grey frame) and phase separate into a L_o and L_d phase (dark grey frame). Scale bars are 20 μm.

Different percentages of cholesterol at a ratio of 1/1 for DOPC/DPPC were tested to find the minimum required cholesterol portion in the LO2 mixture. At a cholesterol percentage of 30% a liquid-liquid phase separation could not be observed for 99% of the vesicles (Figure 7.4).

An increase of the cholesterol portion to 40% led to a liquid-liquid coexistence in more than 90% of the vesicles but only after a light exposure for at least 30 sec. Here, shortly after initiation of phase separation two phases with frayed boundaries could be observed. They quickly merged together and formed circular domains (Figure 7.5). The photo-toxicity dependence of the phase separation indicates that the vesicles were near the miscibility transition. Therefore a further increase of cholesterol should shift the composite membranes away from the miscibility transition towards the unstable mixing regime. Indeed, when the cholesterol portion was increased to 60%, liquid-liquid coexistence became instantaneously visible below the transition temperature T_M.

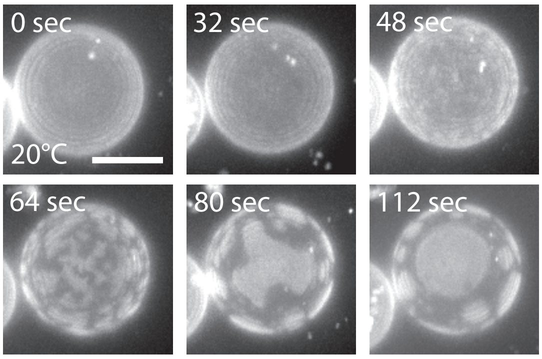

Figure 7.5: At 40% cholesterol phase separation was only induced by light. A temporal evolution of the separation process is shown. Scale bar is 10 µm.

7.2 PHYSICAL CHARACTERIZATION OF PHASE SEPARATION

The size of the two liquid phases depended on the lipid composition, which was used to prepare the lipid-oil emulsions. The amount of the L_o phase (dark) increased with an increasing concentration of DPPC, which could be observed at 60% and 80% cholesterol respectively. Likewise the amount of the L_d phase (bright) decreased (Figure 7.2). Variations of cholesterol did not significantly affect phase distribution and morphology. Rather the ratio between the low and high melting temperature lipid (DOPC and DPPC) determined the size of the two observed phases. Also T_Ms depended on the lipid compositions. T_Ms increased at higher DPPC and lower DOPC percentages, respectively. The transition temperatures increased from 25°C to nearly 38°C at a cholesterol portion of 60% and they increased from 25°C to 45°C at 80% cholesterol. T_Ms measured during the cooling were lower compared to T_Ms measured during the heating. Also variations of cholesterol slightly affected T_M. At a composition of DOPC/DPPC 2/1 T_Ms remained nearly constant during the heating and cooling process. Only at higher portions of DPPC, the T_M increased with an

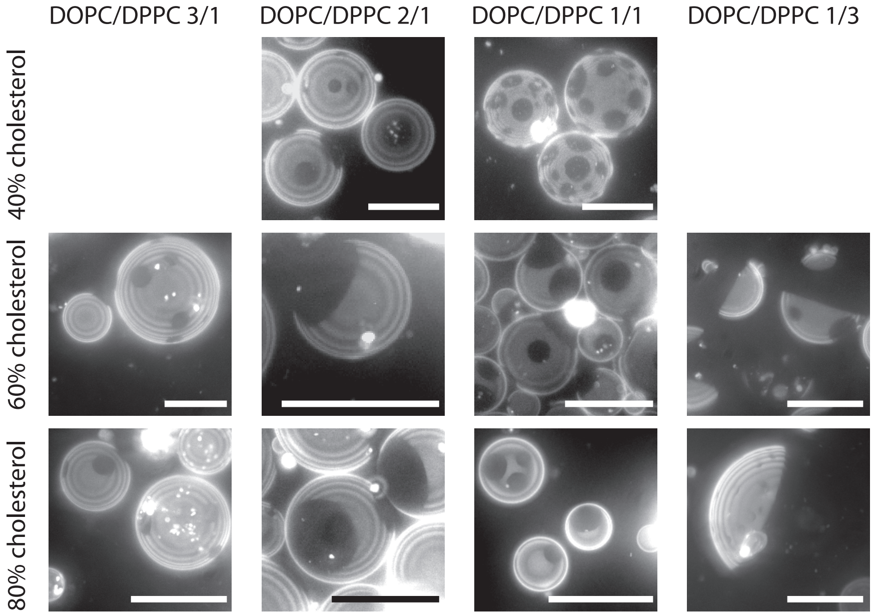

Figure 7.6: A phase diagram of the different vesicle morphologies is shown dependent on the lipid composition, used to prepare the lipid-oil mixtures. Scale bars are 20 µm.

increase of cholesterol (Figure 7.7). Again the T_Ms were lower for the cooling compared to the heating process. Therefore during the heating more energy must be provided and during cooling more energy must be taken from the system to induce phase separation.

Phase separation was fully reversible, when vesicles were heated up above T_M. The formation of the liquid-liquid coexistence was spontaneous for most vesicles when T_M was reached either during the heating or cooling process. In general, full separation was accomplished within 30 sec. Domain fusion of the different phases could be still observed several minutes later. The fused domains regained immediately a circular shape (Figure 7.8).

Spinodal decomposition was also observable but mainly at higher fractions of DPPC and cholesterol. Ribbon like domains appeared suddenly during vesicles cooling (Figure 7.9). The vesicles were either not phase separated before or already displayed circular domains. In both cases sample temperature was near to the T_M. The ribbons were dynamic and fused together within minutes. Full mixing of membranes with ribbon morphology could be also observed during heating-up (Figure 7.10). During heating the structure decomposed continuously and became more fragile when T_M was approached. Shortly, before the full mixing of both phases was accomplished, small liquid-disordered domains of a defined size and a hexagonal shape were homogeneously distributed over the whole vesicle's surface. Their size decreased constantly until they were completely dissolved and the membrane was no longer phase separated.

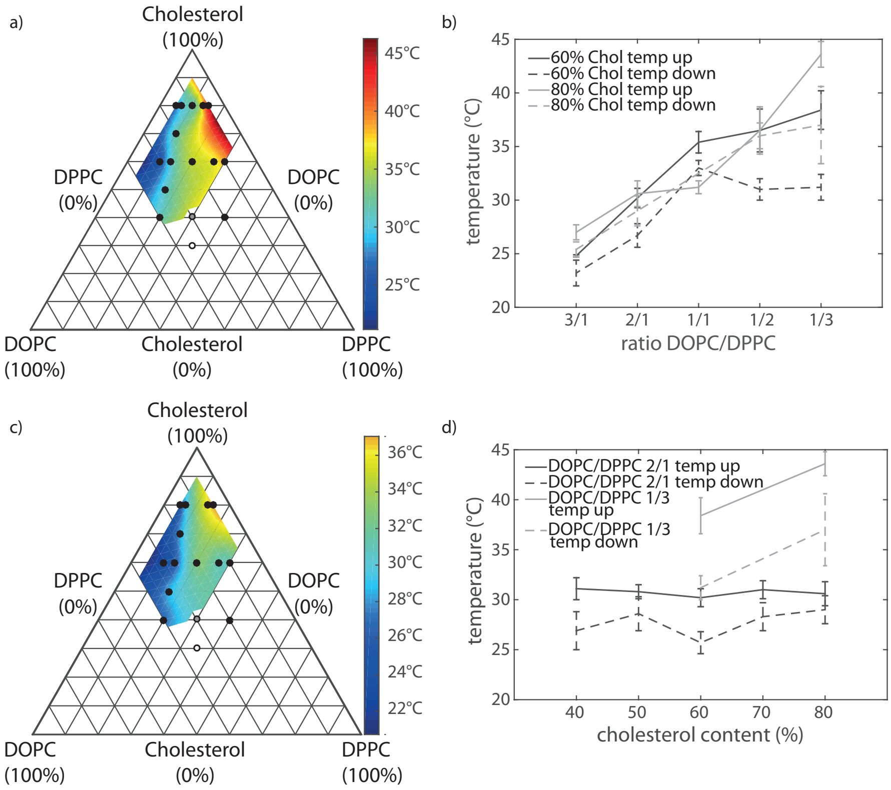

Figure 7.7: The T_Ms for different lipid compositions were measured and are presented in a ternary phase diagram. a) T_Ms were measured during the heating process and in b) they were measured during the cooling process. c,d) Line plots show how T_M varied with different DOPC/DPPC ratios and cholesterol percentages.

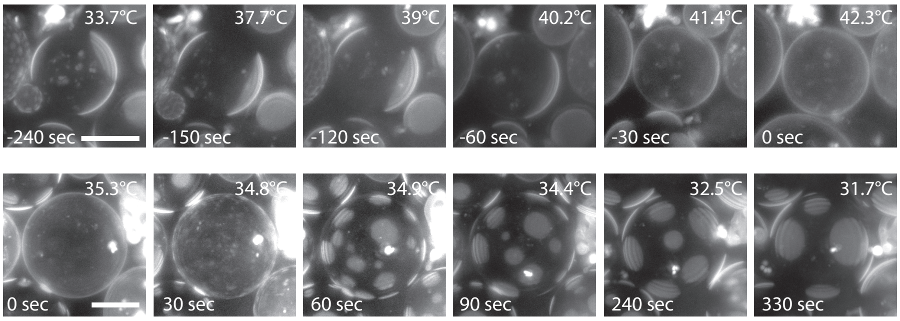
33.7°C
37.7°C
39°C
40.2°C
41.4°C
42.3°C
-240 sec
-150 sec
-120 sec
-60 sec
-30 sec
0 sec
35.3°C
34.8°C
34.9°C
34.4°C
32.5°C
31.7°C
0 sec
30 sec
60 sec
90 sec
240 sec
330 sec

Figure 7.8: Fluorescence z-projections of temporal domain formation are shown. On the top, vesicles were heated up and on the bottom, vesicles were cooled down. The lipid composition of the lipid-oil emulsion was DOPC/DPPC 1/3 and 80% cholesterol. Scale bars are 20 µm.

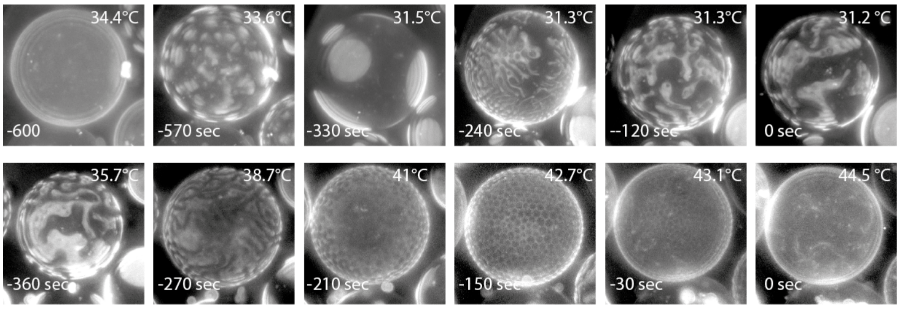
34.4°C
-600
33.6°C
-570 sec
31.5°C
-330 sec
31.3°C
-240 sec
31.3°C
--120 sec
31.2 °C
0 sec
35.7°C
-360 sec
38.7°C
-270 sec
41°C
-210 sec
42.7°C
-150 sec
43.1°C
-30 sec
44.5 °C
0 sec

Figure 7.9: Fluorescence z-projections of spinodal mixing and demixing are shown. Vesicles were produced from lipid-oil emulsion that contained in total 0.5 mM lipids. 80% were cholesterol and the remaining portion of lipids was split in DOPC/DPPC 1/3. Scale bars are 20 µm.

In some vesicles a bulging out of the bright liquid-disordered domains could be observed at different lipid compositions (Figure 7.10). This can be attributed to the fact, that line tension between the two phases minimizes and such forces the bright domains to bend. The bulging out was only observed for bright domains, which can be attributed to the higher fluidity of the liquid-disordered phase.

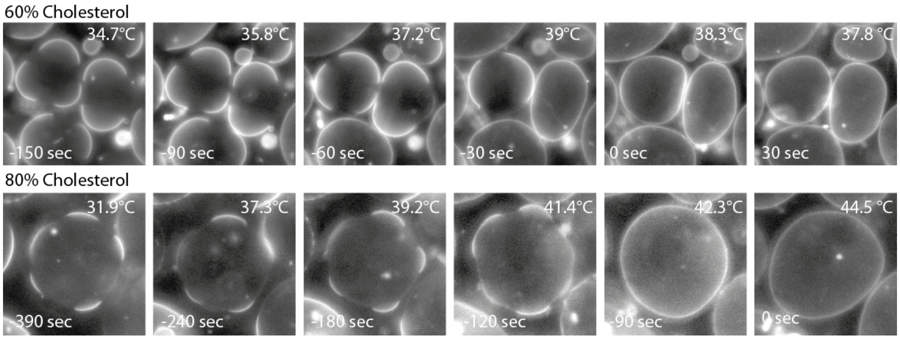
60% Cholesterol
34.7°C
-150 sec
35.8°C
-90 sec
37.2°C
-60 sec
39°C
-30 sec
38.3°C
0 sec
37.8 °C
30 sec
80% Cholesterol
31.9°C
-390 sec
37.3°C
-240 sec
39.2°C
-180 sec
41.4°C
-120 sec
42.3°C
-90 sec
44.5 °C
0 sec

Figure 7.10: Fluorescence z-projections of phase separated vesicles are shown. Membrane bulging of the bright lipid phase can be observed. All scale bars are 20 µm.

7.3 FUNCTIONALIZATION OF LIQUID-DISORDERED DOMAINS BY NINTA-LIPIDS

Last, we tested if one of the lipid phases can be functionalized with NiNTA-lipids to specifically bind proteins to one of the phases. To this end, we used a lipid composition of 27% DOPC, 13% DPPC and 60% cholesterol. 5% of DOPC were replaced by NiNTA. The functionalization was first tested with His-GFP. Thus, 300 nM of His-Tagged GFP was added to the vesicles. His-GFP only bound to the bright lipid phase, which demonstrated that NiNTA can be incorporated into the membrane of phase separated vesicles and segregates into the liquid disordered domain. However binding of His-GFP to the liquid-disordered domain was not homogeneous rather formation of GFP domains was observed (Figure 7.11). Either the NiNTA lipids are not homogeneously distributed, rather they formed small clusters within the liquid-disordered domain or GFP-dimerization induced domain formation.

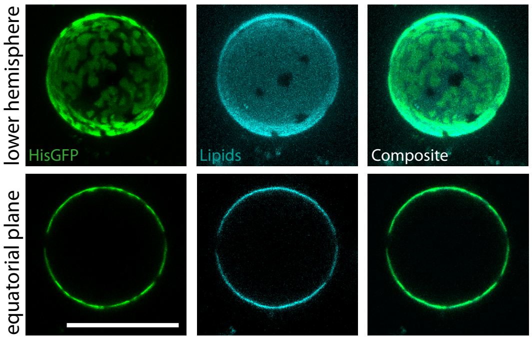

Figure 7.11: Confocal z-projection and the equatorial plane of vesicles containing NiNTA are shown. His-Tagged GFP was bound to the NiNTA-lipids to identify which phase was functionalized. The GFP channel is shown in green and the membrane in cyan. Scale bar is 20 µm.

Likewise the binding of actin to the functionalized domains was tested. The vesicles were transferred into a protein solution containing actin, VCA and Arp2/3. VCA was able to bind to the L_d lipid phase via NiNTA and could activate Arp2/3 complex, which finally induced the formation of a dense actin network only at the L_d phase of the membrane. Actin polymerization was homogeneous and domain formation was not observed (Figure 7.12). This can be attributed to the fact, that the growing network spreads laterally. Still defects in the network were visible supporting the assumption that NiNTA-lipids were not homogeneously distributed within the bright lipid phase. The reason for an inhomogeneous NiNTA distribution could be the presence of cholesterol. Actin polymerization around vesicles composed of Egg PC, PEG2000-PE and NiNTA were homogeneous and displayed no defects. EggPC is a natural lipid mix purified from egg yolk and contains mostly DOPC and DPPC but no cholesterol.

7.4 DISCUSSION

Here we present a modified cDICE protocol, which allows to produce phase separated vesicles at room temperature. The most critical step was to incorporate cholesterol into the vesicle's membrane. Only in the absence of any mineral oil enough cholesterol sorted into the vesicle's membrane and induced the formation of a L_o and L_d phase. Compared to phospholipids cholesterol is more hydrophobic, as it posses only one hydroxyl head group [7] and thus should be better soluble

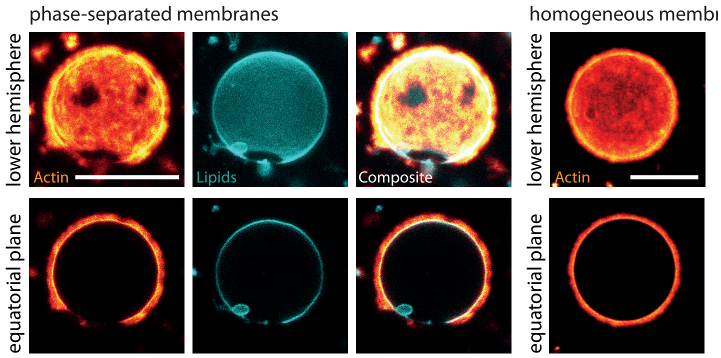

Figure 7.12: Confocal z-projection and the equatorial plane of vesicles containing NiNTA are shown. Vesicles were incubated with the His-Tagged Arp2/3 activator VCA. Afterwards vesicles were transferred into a protein solution including 3 µM actin and 30 nM Arp2/3 complex. The actin channel is shown in red hot and the membrane in cyan. Scale bars are 20 µm.

in hydrophobic solvents. The better solubility leads to the formation of smaller lipid aggregates within the oil mixture. Indeed, turbidity measurements indicated that the oil mixtures became less turbid at high cholesterol percentages. As a consequence, cholesterol partitions less likely to the water-oil interface of the passing protein droplets so that no phase separation is observable [21].

To overcome this issue, the oil properties were adapted to promote a sorting of cholesterol to the water-oil interface. To this end the lipids were dissolved in a mixture composed only of decane and silicone oil. Silicone oil has a higher dielectric constant ($\sim$ 2.7) [59] as mineral oil ($\sim$ 2.1-2.4) [170] and the permittivity of the oil mixture increases. In accordance, the lipid-oil mixtures became more turbid as the aggregate size increases due to the lower solubility of cholesterol in the absence of mineral oil. After production, phase separation with a liquid-liquid coexistence could be observed indicating that cholesterol segregated into the lipid bilayer.

To ensure efficient protein encapsulation, mineral oil is required in the lipid-oil emulsions [39, 89]. Therefore we decided not only to exchange the oil composition of the lipid-oil layer but also to introduce an additional cholesterol rich layer into the cDICE chamber to guarantee that a sufficient amount of cholesterol incorporates into the membrane. At first, the cholesterol-free lipid-oil layer containing 14% mineral oil is passed by the protein droplets, to ensure fast lipid adsorption to the water-oil interface that proteins remain intact during monolayer formation and are not adsorbed at the water oil interface before the arrival of lipids. Second, the droplets pass on to the cholesterol-rich layer without mineral oil. Here cholesterol is incorporated into the lipid bilayer. It is not clear, if cholesterol already gets incorporated during the passage time within the second layer or if it incorporates only during the zipping process of the droplet monolayer and the monolyer assembled at the interface between the cholesterol-rich layer and the glucose solution. We speculate that a preformed monolayer around the droplet promotes cholesterol incorporation as 93% of the vesicles were phase separated when produced by dl-cDICE and only 66% phase separated vesicles occurred when they were produced with the conventional cDICE method but in the absence of any mineral oil.

The morphology and dynamic behavior of phase separation was comparable to phase separated vesicles produced either from biological membranes or by electroswelling [10, 12, 13, 155]. Phase separation was either driven by spontaneous or continuous (spinodal) nucleation. Bulging of the membrane was observed for the more fluid liquid disordered phase. A large difference between the GUVs produced by dl-cDICE or electroswelling was found for the transition temperatures dependent on the lipid composition. For the production of phase separated vesicles by dl-cDICE at least 40% of cholesterol had to be present in the lipid-oil mixture. Whereas phase separation already occurred at cholesterol percentages starting from 10% for GUVs produced by electroswelling. Thus we assume that cholesterol incorporation is less efficient for GUVs produced by dl-cDICE as the liquid-liquid coexistence was shifted to higher cholesterol percentages in the phase diagram. The incorporation efficiency of cholesterol into GUVs can be roughly estimated to be about 25%-30% for dl-cDICE compared to electroswelling [155].

Protein binding to the phase separated membrane affirmed that NiNTA-lipids segregate into the L_d phase and is in accordance with already published data [86]. But it was unknown so far that it does not distribute homogeneously within the L_d phase but rather forms small domains and such induces the formation of His-GFP domains. It remains to be tested if the same observations are made for phase-separated GUVs produced by electroswelling to exclude that NiNTA clustering is not specific to dl-cDICE.

To conclude we found a robust method to incorporate cholesterol into GUVs produced by cDICE to form phase separated vesicles at room temperature. This allows to encapsulate protein solutions with a high encapsulation efficiency and precision [1, 39, 89] and enables a complete new set of experiments to study the interdependence of protein-membrane dynamics.

Part V

CONCLUSION AND OUTLOOK

8

CONCLUSION AND OUTLOOK

It has been a along term goal over the past decades to build up cellular systems from scratch in order to understand the biochemical and physical mechanisms, controlling cellular dynamics. Many cellular processes like cell motility [45, 130, 131, 153, 165], membrane adhesion [103, 104] and organization [12, 85], actomyosin driven contraction [76, 102, 133] or molecular transport [108] have been already successfully reconstituted. But so far most processes were only studied separately. However, to fully understand cellular behavior they need to be combined to study their interdependence.

To this end, it was the aim of this work to investigate the mechanical interplay between the actin cytoskeleton and a flexible membrane, to better understand the underlying physical principles. Reconstitution of lamellipodial and filopodial architecture gave deep insights in the mechanical interplay between different network architectures and flexible membranes. It is the control of the polymerization kinetics, adjusted by the presence of different sets of ABPs, which finally determined the shape remodeling of the membrane. However, combination of different protein systems was difficult due to the different time scales of polymerization. Dendritic network formation is autocatalytic and thus much faster than linear filament elongation. Most of the monomer pool inside the vesicles was already used up before filopodia formation became pronounced.

Encapsulation of proteins from the ADF/cofilin family could solve this issue as they promote filament disassembly and such ensure continuous polymerization [20, 121, 142]. Preliminary experiments were already performed. ADF/cofilin was added to the lamellipodium forming protein set before encapsulation (Figure 8.1). Instead of domain formation a homogeneous cortex formed at the membrane. This was consistent with the encapsulation experiments of actively treadmilling Xenopus laevis extract, where also the formation of a homogeneous cortex could be observed. Thus, implementation of actively polymerizing networks inside of GUVs seems not too far and the full control over the system would allow to study the basic principles behind active network formation and resulting cell migration. First in-vitro experiments already indicated, that ADF/cofilin activity depends on network architecture [58].

Fabrication of actively treadmilling phase-separated vesicles by using the here developed protocol would allow to study the mechanisms behind cell polarization and thus the effects of symmetry breaking on active network formation.

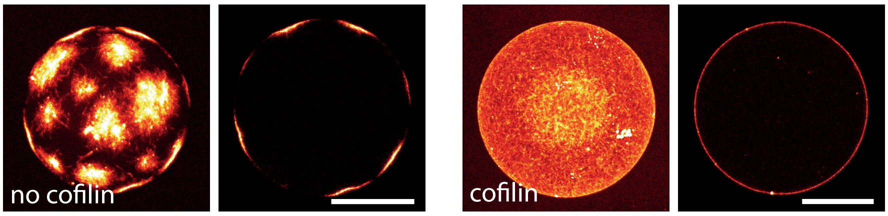

Figure 8.1: On the left side, 3 µM actin, 300 nM VCA, 300 nM Arp2/3, 40 nM CP and 13.5 µM profilin have been encapsulated to form lamellipodia like actin patches at the membrane. On the right side, 300 nM cofilin was added additionally, which induced the formation of a homogeneous cortex. The scale bars are 20 µm.

Implementation of the adhesion machinery could help to better understand the physics behind directed cell movement. Cells must adhere to the extra cellular matrix to translate continuous force transduction into a directed movement [66, 68]. Encapsulation of integrins inside of GUVs, which bind via co-factors like talin or α-actinin to the cytoskeleton, could enable adhesion to the external substrate and such steer force transduction [28]. So far, only membrane adhesion of empty liposomes was reconstituted. Also addition of microtuble dynamics might be an interesting target for future reconstitution experiments. During various cellular processes such as migration, wound healing, neuronal growth and cell division strong interactions between the actin and microtubule cytoskeleton have been observed [123, 163]. Just recently, it was shown that growing microtubule ends steer formin mediated actin assembly [62].
A complete new set of experiments is enabled by the successful encapsulation of Xenopus laevis extract inside of GUVs [107]. Apart from the whole actin machinery, also all components for in-vitro protein transcription and translation should be present [46]. Thus controlled over-expression of various ABPs, either separately but also simultaneously, reveals an elegant way to study actin dynamics and paves the road to fully rebuild cellular processes. In-vitro expression of EGFP in e.coli extract was already successfully implemented inside of GUVs [106] and lasted for days. Promising seems to be the expression of trans-membrane proteins like integrins inside the extract, as their purification in general is challenging. Normally, they are purified in the presence of detergent, which makes them not usable for vesicle studies as any remaining traces of detergent destabilize vesicles. Even though, it is still a long route to fully rebuild artificial cells, this work showed that already many processes have been well understood and can be fully reconstituted to study the interdependence between different cellular systems. Especially the new developed protocols of Xenopus extract encapsulation inside of GUVs and fabrication of phase separated vesicles by cDICE are promising tools for future studies.

BIBLIOGRAPHY

[1] Manouk Abkarian, Etienne Loiseau, and Gladys Massiera. “Continuous droplet interface crossing encapsulation (cDICE) for high throughput monodisperse vesicle design.” In: *Soft Matter* 7.10 (2011), p. 4610.

[2] Vivek C. Abraham et al. “The Actin-Based Nanomachine at the Leading Edge of Migrating Cells.” In: *Biophysical Journal* 77.3 (1999), pp. 1721–1732.

[3] Enas Abu Shah and Kinneret Keren. “Mechanical forces and feedbacks in cell motility.” In: *Current Opinion in Cell Biology* 25.5 (2013), pp. 550–557.

[4] Enas Abu Shah and Kinneret Keren. “Symmetry breaking in reconstituted actin cortices.” In: *eLife* 3.0 (2014), e01433.

[5] Vérane Achard et al. “A "primer"-based mechanism underlies branched actin filament network formation and motility.” In: *Current biology : CB* 20.5 (2010), pp. 423–428.

[6] Orkun Akin and R. Dyche Mullins. “Capping Protein Increases the Rate of Actin-Based Motility by Promoting Filament Nucleation by the Arp2/3 Complex.” In: *Cell* 133.5 (2008), pp. 841–851.

[7] Bruce Alberts. *Molecular biology of the cell*. 6. ed. New York, NY: Garland Science, 2015.

[8] O. Albrecht, H. Gruler, and E. Sackmann. “Polymorphism of phospholipid monolayers.” In: *Journal de Physique* 39.3 (1978), pp. 301–313.

[9] Derek A. Applewhite et al. “Ena/VASP proteins have an anticapping independent function in filopodia formation.” In: *Molecular Biology of the Cell* 18.7 (2007), pp. 2579–2591.

[10] Luis A. Bagatolli and Enrico Gratton. “A Correlation between Lipid Domain Shape and Binary Phospholipid Mixture Composition in Free Standing Bilayers: A Two-Photon Fluorescence Microscopy Study.” In: *Biophysical Journal* 79.1 (2000), pp. 434–447.

[11] M. Barany. “ATPase Activity of Myosin Correlated with Speed of Muscle Shortening.” In: *The Journal of General Physiology* 50.6 (1967), pp. 197–218.

[12] Tobias Baumgart, Samuel T. Hess, and Watt W. Webb. “Imaging coexisting fluid domains in biomembrane models coupling curvature and line tension.” In: *Nature* 425.6960 (2003), pp. 821–824.

[13] Tobias Baumgart et al. “Large-scale fluid/fluid phase separation of proteins and lipids in giant plasma membrane vesicles.” In: *Proceedings of the National Academy of Sciences of the United States of America* 104.9 (2007), pp. 3165–3170.

[14] James E. Bear et al. “Antagonism between Ena/VASP Proteins and Actin Filament Capping Regulates Fibroblast Motility.” In: *Cell* 109.4 (2002), pp. 509–521.

[15] Jessica G. Bermudez et al. “Probing the biology of cell boundary conditions through confinement of Xenopus cell-free cytoplasmic extracts.” In: *Genesis (New York, N.Y. : 2000)* 55.1-2 (2017).

[16] Julien Berro and Thomas D. Pollard. “Synergies between Aip1p and capping protein subunits (Acp1p and Acp2p) in clathrin-mediated endocytosis and cell polarization in fission yeast.” In: *Molecular Biology of the Cell* 25.22 (2014), pp. 3515–3527.

[17] Peter Bieling et al. “Force Feedback Controls Motor Activity and Mechanical Properties of Self-Assembling Branched Actin Networks.” In: *Cell* 164.1-2 (2016), pp. 115–127.

[18] Sara Bisi et al. “Membrane and actin dynamics interplay at lamellipodia leading edge.” In: *Current Opinion in Cell Biology* 25.5 (2013), pp. 565–573.

[19] L. Blanchoin et al. “Direct observation of dendritic actin filament networks nucleated by Arp2/3 complex and WASP/Scar proteins.” In: *Nature* 404.6781 (2000), pp. 1007–1011.

[20] Laurent Blanchoin et al. “Actin dynamics, architecture, and mechanics in cell motility.” In: *Physiological Reviews* 94.1 (2014), pp. 235–263.

[21] Matthew C. Blosser, Benjamin G. Horst, and Sarah L. Keller. “cDICE method produces giant lipid vesicles under physiological conditions of charged lipids and ionic solutions.” In: *Soft Matter* 12.35 (2016), pp. 7364–7371.

[22] Rajaa Boujemaa-Paterski et al. “Network heterogeneity regulates steering in actin-based motility.” In: *Nature communications* 8.1 (2017), p. 655.

[23] Steeve Boulant et al. “Actin dynamics counteract membrane tension during clathrin-mediated endocytosis.” In: *Nature Cell Biology* 13.9 (2011), pp. 1124–1131.

[24] Dennis Breitsprecher et al. “Clustering of VASP actively drives processive, WH2 domain-mediated actin filament elongation.” In: *The EMBO journal* 27.22 (2008), pp. 2943–2954.

[25] Dennis Breitsprecher et al. “Molecular mechanism of Ena/VASP-mediated actin-filament elongation.” In: *The EMBO Journal* 30.3 (2011), pp. 456–467.

[26] Stefan Brühmann et al. "Distinct VASP tetramers synergize in the processive elongation of individual actin filaments from clustered arrays." In: *Proceedings of the National Academy of Sciences of the United States of America* 114.29 (2017), E5815–E5824.

[27] Thomas A. Burke et al. "Homeostatic actin cytoskeleton networks are regulated by assembly factor competition for monomers." In: *Current biology : CB* 24.5 (2014), pp. 579–585.

[28] David A. Calderwood, Iain D. Campbell, and David R. Critchley. "Talins and kindlins: partners in integrin-mediated adhesion." In: *Nature reviews. Molecular cell biology* 14.8 (2013), pp. 503–517.

[29] Anders E. Carlsson and Philip V. Bayly. "Force generation by endocytic actin patches in budding yeast." In: *Biophysical Journal* 106.8 (2014), pp. 1596–1606.

[30] K. Carvalho et al. "Actin polymerization or myosin contraction: two ways to build up cortical tension for symmetry breaking." In: *Philosophical Transactions of the Royal Society B: Biological Sciences* 368.1629 (2013), p. 20130005.

[31] Gregor Cevc and Derek Marsh. *Phospholipid bilayers: Physical principles and models*. New York: John Wiley, 1987.

[32] Guillaume Charras and Ewa Paluch. "Blebs lead the way: how to migrate without lamellipodia." In: *Nature reviews. Molecular cell biology* 9.9 (2008), pp. 730–736.

[33] Jackie Cheng, Alexandre Grassart, and David G. Drubin. "Myosin 1E coordinates actin assembly and cargo trafficking during clathrin-mediated endocytosis." In: *Molecular Biology of the Cell* 23.15 (2012), pp. 2891–2904.

[34] Claessens, Mireille M A E et al. "Actin-binding proteins sensitively mediate F-actin bundle stiffness." In: *Nature materials* 5.9 (2006), pp. 748–753.

[35] Cyrille Claudet, Martin In, and Gladys Massiera. "Method to disperse lipids as aggregates in oil for bilayers production." In: *The European physical journal. E, Soft matter* 39.1 (2016), p. 9.

[36] J. A. Cooper, S. B. Walker, and T. D. Pollard. "Pyrene actin: documentation of the validity of a sensitive assay for actin polymerization." In: *Journal of muscle research and cell motility* 4.2 (1983), pp. 253–262.

[37] David S. Courson and Ronald S. Rock. "Actin cross-link assembly and disassembly mechanics for alpha-Actinin and fascin." In: *The Journal of Biological Chemistry* 285.34 (2010), pp. 26350–26357.

[38] Irene Dang et al. "Inhibitory signalling to the Arp2/3 complex steers cell migration." In: *Nature* 503.7475 (2013), pp. 281–284.

[39] Katharina Dürre et al. "Capping protein-controlled actin polymerization shapes lipid membranes." In: *Nature Communications* 9.1 (2018), p. 454.

[40] Marc Edwards et al. "Capping protein regulators fine-tune actin assembly dynamics." In: *Nature reviews. Molecular cell biology* 15.10 (2014), pp. 677–689.

[41] Coumaran Egile et al. "Activation of the Cdc42 Effector N-Wasp by the Shigella flexneri Icsa Protein Promotes Actin Nucleation by Arp2/3 Complex and Bacterial Actin-Based Motility." In: *The Journal of Cell Biology* 146.6 (1999), pp. 1319–1332.

[42] El Alaoui Faris, M D et al. "Membrane tension lowering induced by protein activity." In: *Physical review letters* 102.3 (2009), p. 038102.

[43] Jan Faix and Klemens Rottner. "The making of filopodia." In: *Current Opinion in Cell Biology* 18.1 (2006), pp. 18–25.

[44] Sandra Falck et al. "Biological role and structural mechanism of twinfilin-capping protein interaction." In: *The EMBO journal* 23.15 (2004), pp. 3010–3019.

[45] Tobias T. Falzone et al. "Actin assembly factors regulate the gelation kinetics and architecture of F-actin networks." In: *Biophysical Journal* 104.8 (2013), pp. 1709–1719.

[46] Marina Feric et al. "Coexisting Liquid Phases Underlie Nucleolar Subcompartments." In: *Cell* 165.7 (2016), pp. 1686–1697.

[47] Christine M. Field et al. "Actin behavior in bulk cytoplasm is cell cycle regulated in early vertebrate embryos." In: *Journal of cell science* 124.Pt 12 (2011), pp. 2086–2095.

[48] Christine M. Field et al. "Xenopus egg cytoplasm with intact actin." In: *Methods in Enzymology* 540 (2014), pp. 399–415.

[49] Kate S. Foley and Paul W. Young. "The non-muscle functions of actinins: an update." In: *The Biochemical journal* 459.1 (2014), pp. 1–13.

[50] Giacomo Franzot et al. "The crystal structure of the actin binding domain from alpha-actinin in its closed conformation: structural insight into phospholipid regulation of alpha-actinin." In: *Journal of Molecular Biology* 348.1 (2005), pp. 151–165.

[51] I. Fujiwara et al. "Capping protein regulatory cycle driven by CARMIL and V-1 may promote actin network assembly at protruding edges." In: *Proceedings of the National Academy of Sciences* 111.19 (2014), E1970–E1979.

[52] Rémi Galland et al. "Fabrication of three-dimensional electrical connections by means of directed actin self-organization." In: *Nature Materials* 12.5 (2013), pp. 416–421.

[53] Brian S. Gentry et al. "Multiple actin binding domains of Ena/-VASP proteins determine actin network stiffening." In: *European biophysics journal : EBJ* 41.11 (2012), pp. 979–990.

[54] Fabien Gerbal et al. "An Elastic Analysis of Listeria monocytogenes Propulsion." In: *Biophysical Journal* 79.5 (2000), pp. 2259–2275.

[55] Erin D. Goley and Matthew D. Welch. "The ARP2/3 complex: an actin nucleator comes of age." In: *Nature Reviews Molecular Cell Biology* 7.10 (2006), pp. 713–726.

[56] M. C. Good et al. "Cytoplasmic Volume Modulates Spindle Size During Embryogenesis." In: *Science* 342.6160 (2013), pp. 856–860.

[57] Nir S. Gov and Ajay Gopinathan. "Dynamics of membranes driven by actin polymerization." In: *Biophysical Journal* 90.2 (2006), pp. 454–469.

[58] Laurène Gressin et al. "Architecture dependence of actin filament network disassembly." In: *Current biology : CB* 25.11 (2015), pp. 1437–1447.

[59] Raymond Hakim, Ronald Olivier, and Hugues St-Onge. "The Dielectric Properties of Silicone Fluids." In: *IEEE Transactions on Electrical Insulation* EI-12.5 (1977), pp. 360–370.

[60] S. D. Hansen and R. D. Mullins. "VASP is a processive actin polymerase that requires monomeric actin for barbed end association." In: *The Journal of Cell Biology* 191.3 (2010), pp. 571–584.

[61] James Hazel et al. "Changes in cytoplasmic volume are sufficient to drive spindle scaling." In: *Science (New York, N.Y.)* 342.6160 (2013), pp. 853–856.

[62] Jessica L. Henty-Ridilla et al. "Accelerated actin filament polymerization from microtubule plus ends." In: *Science (New York, N.Y.)* 352.6288 (2016), pp. 1004–1009.

[63] H. N. Higgs and T. D. Pollard. "Regulation of actin filament network formation through ARP2/3 complex: activation by a diverse array of proteins." In: *Annual review of biochemistry* 70 (2001), pp. 649–676.

[64] Terrell L. Hill. *Linear Aggregation Theory in Cell Biology*. Springer Series in Molecular Biology. New York, NY: Springer New York, 1987.

[65] Alf Honigmann et al. "A lipid bound actin meshwork organizes liquid phase separation in model membranes." In: *eLife* (2014).

[66] John D. Hood and David A. Cheresh. "Role of integrins in cell invasion and migration." In: *Nature reviews. Cancer* 2.2 (2002), pp. 91–100.

[67] Christopher Hug et al. "Capping protein levels influence actin assembly and cell motility in dictyostelium." In: *Cell* 81.4 (1995), pp. 591–600.

[68] Richard O. Hynes. "Integrins: Versatility, modulation, and signaling in cell adhesion." In: *Cell* 69.1 (1992), pp. 11–25.

[69] Jacob N. Israelachvili. *Intermolecular and surface forces*. Amsterdam, Boston, and Paris: Elsevier, 2011.

[70] Ludger Johannes et al. "Building endocytic pits without clathrin." In: *Nature reviews. Molecular cell biology* 16.5 (2015), pp. 311–321.

[71] Richard A. L. Jones. *Soft condensed matter*. Reprinted. Oxford Master Series in Condensed Matter Physics. Oxford: Oxford University Press, 2014.

[72] Goeh Jung et al. "V-1 regulates capping protein activity in vivo." In: *Proceedings of the National Academy of Sciences of the United States of America* 113.43 (2016), E6610–E6619.

[73] Felix C. Keber. "Dynamics and self-organisation of active cytoskeletal gels." Dissertation. München: Technische Universität München, 2017.

[74] Felix C. Keber et al. "Topology and dynamics of active nematic vesicles." In: *Science (New York, N.Y.)* 345.6201 (2014), pp. 1135–1139.

[75] D. R. Kellogg, T. J. Mitchison, and B. M. Alberts. "Behaviour of microtubules and actin filaments in living Drosophila embryos." In: *Development (Cambridge, England)* 103.4 (1988), pp. 675–686.

[76] Simone Köhler et al. "Regulating contractility of the actomyosin cytoskeleton by pH." In: *Cell reports* 2.3 (2012), pp. 433–439.

[77] Darius Vasco Köster et al. "Actomyosin dynamics drive local membrane component organization in an in vitro active composite layer." In: *Proceedings of the National Academy of Sciences of the United States of America* 113.12 (2016), E1645–54.

[78] Matthias Krause and Alexis Gautreau. "Steering cell migration: lamellipodium dynamics and the regulation of directional persistence." In: *Nature reviews. Molecular cell biology* 15.9 (2014), pp. 577–590.

[79] Matthias Krause et al. "Ena/VASP proteins: regulators of the actin cytoskeleton and cell migration." In: *Annual review of cell and developmental biology* 19 (2003), pp. 541–564.

[80] Wanda Kukulski et al. "Plasma membrane reshaping during endocytosis is revealed by time-resolved electron tomography." In: *Cell* 150.3 (2012), pp. 508–520.

[81] F. Lanni and B. R. Ware. "Detection and characterization of actin monomers, oligomers, and filaments in solution by measurement of fluorescence photobleaching recovery." In: *Biophysical Journal* 46.1 (1984), pp. 97–110.

[82] Le Ma et al. "Corequirement of Specific Phosphoinositides and Small GTP-binding Protein Cdc42 in Inducing Actin Assembly in Xenopus Egg Extracts." In: *The Journal of Cell Biology* 140.5 (1998), pp. 1125–1136.

[83] Kwonmoo Lee et al. "Self-assembly of filopodia-like structures on supported lipid bilayers." In: *Science (New York, N.Y.)* 329.5997 (2010), pp. 1341–1345.

[84] O. Lieleg et al. "Mechanics of bundled semiflexible polymer networks." In: *Physical review letters* 99.8 (2007), p. 088102.

[85] Daniel Lingwood and Kai Simons. "Lipid rafts as a membrane-organizing principle." In: *Science (New York, N.Y.)* 327.5961 (2010), pp. 46–50.

[86] Allen P. Liu and Daniel A. Fletcher. "Actin Polymerization Serves as a Membrane Domain Switch in Model Lipid Bilayers." In: *Biophysical Journal* 91.11 (2006), pp. 4064–4070.

[87] Allen P. Liu et al. "Membrane-induced bundling of actin filaments." In: *Nature Physics* 4.10 (2008), pp. 789–793.

[88] Jian Liu et al. "Mechanochemical crosstalk during endocytic vesicle formation." In: *Current Opinion in Cell Biology* 22.1 (2010), pp. 36–43.

[89] Etienne Loiseau et al. "Shape remodeling and blebbing of active cytoskeletal vesicles." In: *Science advances* 2.4 (2016), e1500465.

[90] Laura M. Machesky and Kathleen L. Gould. "The Arp2/3 complex: A multifunctional actin organizer." In: *Current Opinion in Cell Biology* 11.1 (1999), pp. 117–121.

[91] J. B. Marchand et al. "Interaction of WASP/Scar proteins with actin and vertebrate Arp2/3 complex." In: *Nature Cell Biology* 3.1 (2001), pp. 76–82.

[92] Derek Marsh. *Handbook of Lipid Bilayers*. Second edition. Boca Raton, FL: CRC Press, 2013.

[93] Pieta K. Mattila and Pekka Lappalainen. "Filopodia: molecular architecture and cellular functions." In: *Nature Reviews Molecular Cell Biology* 9.6 (2008), pp. 446–454.

[94] Marisan R. Mejillano et al. "Lamellipodial Versus Filopodial Mode of the Actin Nanomachinery." In: *Cell* 118.3 (2004), pp. 363–373.

[95] A. Mogilner and G. Oster. "Cell motility driven by actin polymerization." In: *Biophysical Journal* 71.6 (1996), pp. 3030–3045.

[96] A. Mogilner and B. Rubinstein. "The physics of filopodial protrusion." In: *Biophysical Journal* 89.2 (2005), pp. 782–795.

[97] Alex Mogilner. "On the edge: modeling protrusion." In: *Current Opinion in Cell Biology* 18.1 (2006), pp. 32–39.

[98] Alex Mogilner and Leah Edelstein-Keshet. "Regulation of Actin Dynamics in Rapidly Moving Cells: A Quantitative Analysis." In: *Biophysical Journal* 83.3 (2002), pp. 1237–1258.

[99] Alex Mogilner and George Oster. "Force Generation by Actin Polymerization II: The Elastic Ratchet and Tethered Filaments." In: *Biophysical Journal* 84.3 (2003), pp. 1591–1605.

[100] Svetlana Mukhina, Yu-Li Wang, and Maki Murata-Hori. "Alpha-actinin is required for tightly regulated remodeling of the actin cortical network during cytokinesis." In: *Developmental cell* 13.4 (2007), pp. 554–565.

[101] R. D. Mullins, J. A. Heuser, and T. D. Pollard. "The interaction of Arp2/3 complex with actin: Nucleation, high affinity pointed end capping, and formation of branching networks of filaments." In: *Proceedings of the National Academy of Sciences* 95.11 (1998), pp. 6181–6186.

[102] Michael P. Murrell and Margaret L. Gardel. "F-actin buckling coordinates contractility and severing in a biomimetic actomyosin cortex." In: *Proceedings of the National Academy of Sciences of the United States of America* 109.51 (2012), pp. 20820–20825.

[103] Michael P. Murrell et al. "Liposome adhesion generates traction stress." In: *Nature Physics* 10.2 (2014), pp. 163–169.

[104] Michael Murrell et al. "Spreading Dynamics of Biomimetic Actin Cortices." In: *Biophysical Journal* 100.6 (2011), pp. 1400–1409.

[105] R. Niederman. "Human platelet myosin. II. In vitro assembly and structure of myosin filaments." In: *The Journal of Cell Biology* 67.1 (1975), pp. 72–92.

[106] Vincent Noireaux and Albert Libchaber. "A vesicle bioreactor as a step toward an artificial cell assembly." In: *Proceedings of the National Academy of Sciences of the United States of America* 101.51 (2004), pp. 17669–17674.

[107] Vincent Noireaux, Yusuke T. Maeda, and Albert Libchaber. "Development of an artificial cell, from self-organization to computation and self-reproduction." In: *Proceedings of the National Academy of Sciences of the United States of America* 108.9 (2011), pp. 3473–3480.

[108] Angela Oberhofer et al. "Myosin Va's adaptor protein melanophilin enforces track selection on the microtubule and actin networks in vitro." In: *Proceedings of the National Academy of Sciences of the United States of America* 114.24 (2017), E4714–E4723.

[109] Ewa Paluch, van der Gucht, Jasper, and Cécile Sykes. "Cracking up: symmetry breaking in cellular systems." In: *The Journal of Cell Biology* 175.5 (2006), pp. 687–692.

[110] Ewa Paluch et al. "Cortical actomyosin breakage triggers shape oscillations in cells and cell fragments." In: *Biophysical Journal* 89.1 (2005), pp. 724–733.

[111] D. Pantaloni et al. "The Arp2/3 complex branches filament barbed ends: functional antagonism with capping proteins." In: *Nature Cell Biology* 2.7 (2000), pp. 385–391.

[112] Sapun H. Parekh et al. "Loading history determines the velocity of actin-network growth." In: *Nature Cell Biology* 7.12 (2005), pp. 1219–1223.

[113] C. S. Peskin, G. M. Odell, and G. F. Oster. "Cellular motions and thermal fluctuations: The Brownian ratchet." In: *Biophysical Journal* 65.1 (1993), pp. 316–324.

[114] Ryan J. Petrie, Andrew D. Doyle, and Kenneth M. Yamada. "Random versus directionally persistent cell migration." In: *Nature reviews. Molecular cell biology* 10.8 (2009), pp. 538–549.

[115] Mathieu Pinot et al. "Confinement induces actin flow in a meiotic cytoplasm." In: *Proceedings of the National Academy of Sciences of the United States of America* 109.29 (2012), pp. 11705–11710.

[116] Julie Plastino and Cécile Sykes. "The actin slingshot." In: *Current Opinion in Cell Biology* 17.1 (2005), pp. 62–66.

[117] T. D. Pollard, L. Blanchoin, and R. D. Mullins. "Molecular mechanisms controlling actin filament dynamics in nonmuscle cells." In: *Annual review of biophysics and biomolecular structure* 29 (2000), pp. 545–576.

[118] Thomas D. Pollard. "[31] Purification of nonmuscle myosins." In: *Structural and Contractile Proteins Part B: The Contractile Apparatus and the Cytoskeleton*. Vol. 85. Methods in Enzymology. Elsevier, 1982, pp. 331–356.

[119] Thomas D. Pollard and Gary G. Borisy. "Cellular Motility Driven by Assembly and Disassembly of Actin Filaments." In: *Cell* 112.4 (2003), pp. 453–465.

[120] Léa-Laetitia Pontani et al. "Reconstitution of an Actin Cortex Inside a Liposome." In: *Biophysical Journal* 96.1 (2009), pp. 192–198.

[121] Dikla Raz-Ben Aroush et al. “Actin Turnover in Lamellipodial Fragments.” In: *Current biology : CB* 27.19 (2017), 2963–2973.e14.

[122] Anne J. Ridley et al. “Cell migration: integrating signals from front to back.” In: *Science (New York, N.Y.)* 302.5651 (2003), pp. 1704–1709.

[123] Olga C. Rodriguez et al. “Conserved microtubule-actin interactions in cell movement and morphogenesis.” In: *Nature Cell Biology* 5.7 (2003), pp. 599–609.

[124] Winfried Römer et al. “Actin dynamics drive membrane reorganization and scission in clathrin-independent endocytosis.” In: *Cell* 140.4 (2010), pp. 540–553.

[125] K. Rottner et al. “VASP dynamics during lamellipodia protrusion.” In: *Nature Cell Biology* 1.5 (1999), pp. 321–322.

[126] Guillaume Salbreux, Guillaume Charras, and Ewa Paluch. “Actin cortex mechanics and cellular morphogenesis.” In: *Trends in Cell Biology* 22.10 (2012), pp. 536–545.

[127] M. Sato, W. H. Schwarz, and T. D. Pollard. “Dependence of the mechanical properties of actin/alpha-actinin gels on deformation rate.” In: *Nature* 325.6107 (1987), pp. 828–830.

[128] D. A. Schafer. “Dynamics of capping protein and actin assembly in vitro: Uncapping barbed ends by polyphosphoinositides.” In: *The Journal of Cell Biology* 135.1 (1996), pp. 169–179.

[129] Antje Schirenbeck et al. “The bundling activity of vasodilator-stimulated phosphoprotein is required for filopodium formation.” In: *Proceedings of the National Academy of Sciences of the United States of America* 103.20 (2006), pp. 7694–7699.

[130] K. M. Schmoller, O. Lieleg, and A. R. Bausch. “Structural and Viscoelastic Properties of Actin/Filamin Networks: Cross-Linked versus Bundled Networks.” In: *Biophysical Journal* 97.1 (2009), pp. 83–89.

[131] Kurt M. Schmoller, Christine Semmrich, and Andreas R. Bausch. “Slow down of actin depolymerization by cross-linking molecules.” In: *Journal of Structural Biology* 173.2 (2011), pp. 350–357.

[132] Daniel V. Schroeder. *An introduction to thermal physics*. [Nachdr.] San Francisco, Calif.: Addison Wesley Longman, 2005.

[133] Matthias Schuppler et al. “Boundaries steer the contraction of active gels.” In: *Nature communications* 7 (2016), p. 13120.

[134] Erdinc Sezgin et al. “The mystery of membrane organization: composition, regulation and roles of lipid rafts.” In: *Nature reviews. Molecular cell biology* 18.6 (2017), pp. 361–374.

[135] John R. Silvius. "Role of cholesterol in lipid raft formation: Lessons from lipid model systems." In: *Biochimica et Biophysica Acta (BBA) - Biomembranes* 1610.2 (2003), pp. 174–183.

[136] K. Simons and D. Toomre. "Lipid rafts and signal transduction." In: *Nature reviews. Molecular cell biology* 1.1 (2000), pp. 31–39.

[137] Kai Simons and Mathias J. Gerl. "Revitalizing membrane rafts: new tools and insights." In: *Nature reviews. Molecular cell biology* 11.10 (2010), pp. 688–699.

[138] Mijo Simunovic et al. "Friction Mediates Scission of Tubular Membranes Scaffolded by BAR Proteins." In: *Cell* 170.1 (2017), 172–184.e11.

[139] B. Sjöblom, A. Salmazo, and K. Djinović-Carugo. "Alpha-actinin structure and regulation." In: *Cellular and molecular life sciences : CMLS* 65.17 (2008), pp. 2688–2701.

[140] J. V. Small. "Actin filament organization in the fish keratocyte lamellipodium." In: *The Journal of Cell Biology* 129.5 (1995), pp. 1275–1286.

[141] J. A. Spudich and S. Watt. "The regulation of rabbit skeletal muscle contraction. I. Biochemical studies of the interaction of the tropomyosin-troponin complex with actin and the proteolytic fragments of myosin." In: *The Journal of Biological Chemistry* 246.15 (1971), pp. 4866–4871.

[142] Christopher J. Staiger and Laurent Blanchoin. "Actin dynamics: old friends with new stories." In: *Current opinion in plant biology* 9.6 (2006), pp. 554–562.

[143] Anika Steffen et al. "Filopodia formation in the absence of functional WAVE- and Arp2/3-complexes." In: *Molecular Biology of the Cell* 17.6 (2006), pp. 2581–2591.

[144] Cristian Suarez et al. "Profilin regulates F-actin network homeostasis by favoring formin over Arp2/3 complex." In: *Developmental cell* 32.1 (2015), pp. 43–53.

[145] Sandy Suei, Julie Plastino, and Laurent Kreplak. "Fascin and VASP synergistically increase the Young's modulus of actin comet tails." In: *Journal of Structural Biology* 177.1 (2012), pp. 40–45.

[146] Yidi Sun, Adam C. Martin, and David G. Drubin. "Endocytic internalization in budding yeast requires coordinated actin nucleation and myosin motor activity." In: *Developmental cell* 11.1 (2006), pp. 33–46.

[147] A. Suzuki et al. "Some properties of purified skeletal muscle alpha-actinin." In: *The Journal of Biological Chemistry* 251.21 (1976), pp. 6860–6870.

[148] Sven Kenjiro Vogel, Ferdinand Greiss, Alena Khmelinskaia, Petra Schwille. "Control of lipid domain organization by a biomimetic contractile actomyosin cortex." In: *eLife* (2017).

[149] Tatyana M. Svitkina et al. "Mechanism of filopodia initiation by reorganization of a dendritic network." In: *The Journal of Cell Biology* 160.3 (2003), pp. 409–421.

[150] Nessy Tania, John Condeelis, and Leah Edelstein-Keshet. "Modeling the synergy of cofilin and Arp2/3 in lamellipodial protrusive activity." In: *Biophysical Journal* 105.9 (2013), pp. 1946–1955.

[151] Tatyana M. Svitkina, Gary G. Borisy. "Arp2/3 Complex and Actin Depolymerizing Factor/Cofilin in Dendritic Organization and Treadmilling of Actin Filament Array in Lamellipodia." In: *Journal of Cell Biology* (1999).

[152] Julie A. Theriot et al. "Involvement of profilin in the actin-based motility of L. monocytogenes in cells and in cell-free extracts." In: *Cell* 76.3 (1994), pp. 505–517.

[153] Thomas P. Loisel, Rajaa Boujemaa, Dominique Pantaloni & Marie-France Carlier et al. "Reconstitution of actin-based motility of Listeria and Shigella using pure proteins." In: *Nature* 401.6753 (1999), pp. 613–616.

[154] Sarah L. Veatch and Sarah L. Keller. "Organization in Lipid Membranes Containing Cholesterol." In: *Physical Review Letters* 89.26 (2002).

[155] Sarah L. Veatch and Sarah L. Keller. "Separation of Liquid Phases in Giant Vesicles of Ternary Mixtures of Phospholipids and Cholesterol." In: *Biophysical Journal* 85.5 (2003), pp. 3074–3083.

[156] Sarah L. Veatch and Sarah L. Keller. "Miscibility phase diagrams of giant vesicles containing sphingomyelin." In: *Physical review letters* 94.14 (2005), p. 148101.

[157] Alexander B. Verkhovsky. "The mechanisms of spatial and temporal patterning of cell-edge dynamics." In: *Current Opinion in Cell Biology* 36 (2015), pp. 113–121.

[158] Miguel Vicente-Manzanares et al. "Non-muscle myosin II takes centre stage in cell adhesion and migration." In: *Nature reviews. Molecular cell biology* 10.11 (2009), pp. 778–790.

[159] Danijela Vignjevic et al. "Formation of filopodia-like bundles in vitro from a dendritic network." In: *The Journal of Cell Biology* 160.6 (2003), pp. 951–962.

[160] Danijela Vignjevic et al. "Role of fascin in filopodial protrusion." In: *The Journal of Cell Biology* 174.6 (2006), pp. 863–875.

[161] Sven Kenjiro Vogel et al. “Control of lipid domain organization by a biomimetic contractile actomyosin cortex.” In: *eLife* 6 (2017), e00116.

[162] John M. Walker and X. Johné Liu. *Xenopus Protocols*. Vol. 322. Totowa, NJ: Humana Press, 2006.

[163] Clare M. Waterman-Storer and E. D. Salmon. “Positive feedback interactions between microtubule and actin dynamics during cell motility.” In: *Current Opinion in Cell Biology* 11.1 (1999), pp. 61–67.

[164] Julian Weichsel and Ulrich S. Schwarz. “Two competing orientation patterns explain experimentally observed anomalies in growing actin networks.” In: *Proceedings of the National Academy of Sciences of the United States of America* 107.14 (2010), pp. 6304–6309.

[165] S. Wiesner. “A biomimetic motility assay provides insight into the mechanism of actin-based motility.” In: *The Journal of Cell Biology* 160.3 (2003), pp. 387–398.

[166] Jonathan D. Winkelman et al. “Ena/VASP Enabled is a highly processive actin polymerase tailored to self-assemble parallel-bundled F-actin networks with Fascin.” In: *Proceedings of the National Academy of Sciences of the United States of America* 111.11 (2014), pp. 4121–4126.

[167] Changsong Yang and Tatyana Svitkina. “Filopodia initiation: focus on the Arp2/3 complex and formins.” In: *Cell adhesion & migration* 5.5 (2011), pp. 402–408.

[168] Christopher M. Yengo, Yasuharu Takagi, and James R. Sellers. “Temperature dependent measurements reveal similarities between muscle and non-muscle myosin motility.” In: *Journal of muscle research and cell motility* 33.6 (2012), pp. 385–394.

[169] Lorna E. Young, Ernest G. Heimsath, and Henry N. Higgs. “Cell type-dependent mechanisms for formin-mediated assembly of filopodia.” In: *Molecular Biology of the Cell* 26.25 (2015), pp. 4646–4659.

[170] Yuan Zhou et al. “Study of the dielectric response in mineral oil using frequency-domain measurement.” In: *Journal of Applied Physics* 115.12 (2014), p. 124105.

[171] Juliane Zimmermann et al. “Actin Filament Elasticity and Retrograde Flow Shape the Force-Velocity Relation of Motile Cells.” In: *Biophysical Journal* 102.2 (2012), pp. 287–295.

[172] Gerrit van Meer, Dennis R. Voelker, and Gerald W. Feigenson. “Membrane lipids: where they are and how they behave.” In: *Nature reviews. Molecular cell biology* 9.2 (2008), pp. 112–124.

[173] van der Gucht, Jasper et al. “Stress release drives symmetry breaking for actin-based movement.” In: *Proceedings of the National Academy of Sciences of the United States of America* 102.22 (2005), pp. 7847–7852.